**University of West Bohemia**

**Faculty of Applied Sciences**

# Doctoral thesis

**2023**

**Ing. Sven Künkel**

**University of West Bohemia**
**Faculty of Applied Sciences**

# DESIGN AND IMPLEMENTATION OF A METHOD OF MONITORING THE INTERACTION BETWEEN THE TURBINE-GENERATOR AND THE ELECTRICAL NETWORK

**Ing. Sven Künkel**

doctoral thesis
submitted in partial fulfillment of the requirements
for the degree of Doctor of Philosophy
in Cybernetics

**Supervisor: Doc. Ing. Eduard Janeček, CSc.**

**Specialist consultant: Ing. Jindřich Liška, Ph.D.**

**Department: Cybernetics**

**Pilsen 2023**

**Západočeská univerzita v Plzni**
**Fakulta aplikovaných věd**

# NÁVRH A IMPLEMENTACE METODY MONITORINGU INTERAKCE MEZI TURBOGENERÁTOREM A ELEKTRIZAČNÍ SÍTÍ

**Ing. Sven Künkel**

Disertační práce
k získání akademického titulu doktor
v oboru Kybernetika

**Školitel: Doc. Ing. Eduard Janeček, CSc.**

**Konzultant specialista: Ing. Jindřich Liška, Ph.D.**

**Katedra: Kybernetiky**

**Plzeň 2023**

# Declaration

I declare that this thesis is my original work of authorship that I have created myself. All resources, sources and literature, which I used in my thesis, are cited indicating the full link to the appropriate source.

In Pilsen: 6.8.2023 .....

Sven Künkel

# Abstract

The work was focused on the research and development of methods, software and the necessary components of the measuring chain for the purpose of analysis and subsequent monitoring of the torsional interaction of the turbine-generator with the events in the electricity network. As described, the torsional interaction is enabled by means of the air-gap torque of the generator, as this is a quantity dependent both on the motion state of the rotor as well as on the current electrical state of the generator. The complexity of the problem is due to the fact that the information on torsional vibration cannot be measured directly, as for example the absolute vibration of bearings, but a special measurement and a relatively complex post-processing must be used. As part of the work, an algorithm was developed and successfully validated for the evaluation of the instantaneous angular velocity, from which the amplitude and frequency of the rotor torsional oscillation can subsequently be evaluated. In addition, some limitations of the proposed method are discussed, as well as limitations resulting from the nature of measuring torsional oscillations with an incremental encoder. The presented case studies prove the existence of significant oscillatory components with a variable frequency originating in the power grid relevant for torsional viration excitation. Furthermore, examples were shown where a sudden change in the state of the electricity network caused a transient excitation of the torsional oscillations of the turbine-generator rotor. A TVMS Torsional Vibration Monitoring System was assembled and programmed in the Labview programming language which has already been deployed on 14 turbine-generators with a total capacity of 3 GW.

# Abstrakt

Práce byla zaměřena na výzkum a vývoj metod, softwaru a potřebných komponent měřicího řetězce za účelem analýzy a následného monitorování torzní interakce turbogenerátoru s ději v elektrizační síti. Tato torzní interakce je zprostředkována momentem ve vzduchové mezeře generátoru, neboť ten je veličinou závislou jak na pohybovém stavu rotoru tak na aktuálním elektrickém stavu generátoru. Složitost úlohy je dána tím, že informace o torzním kmitání není měřitelná přímo jako na příklad absolutní vibrace ložisek, nýbrž musí být použito speciální měření a následně relativně složitý post-processing. V rámci práce byl vyvinut a na praktických datech úspešně otestován algoritmus pro vyhodnocení okamžité úhlové rychlosti, z níž lze následně vyhodnotit amplitudy a frekvence torzního kmitání rotoru. Navíc jsou diskutovány některá omezení navržené metody i omezení plynoucí z podstaty měření torzních kmitů inkrementálním enkodérem. V rámci případových studií se podařila prokázat existence z hlediska buzení torzních kmitů významných oscilačních složek s proměnnou frekvencí s původem v elektrizační síti. Dále byla ukázána řada příkladů, kdy skoková změna podmínek v elektrizační síti způsobila přechodné vybuzení torzních kmitů rotoru turbogenerátoru. Konečně, byl sestaven a v programovacím jazyce Labview naprogramován systém pro měření torzních vibrací TVMS, který byl dosud nasazen na 14 turbogenerátorech o celkovém výkonu 3 GW.

# Acknowledgement

I especially would like to thank my supervisor Eduard Janeček for leading me in the right direction during my studies. I would also like to acknowledge to Jindřich Liška for an extraordinary willingness to discuss all problems which occurred during the work and to create conditions for bringing it to a successful final. My family also supported me a lot during the study years.

# Contents

Contents ... 9
Introduction and objectives of the work ... 11
1 Electromechanical model of rotor torsional vibration ... 13
1.1 Mechanical model – rotor torsional vibration ... 13
1.1.1 Kinematic model of torsional vibration ... 13
1.1.2 Rotor static torsion ... 14
1.1.3 Torsional vibration of a discrete oscillator ... 17
1.1.4 Continuous body torsional vibration ... 18
1.1.5 Specifics of large turbine-generators ... 22
1.2 Electrical model – synchronous generator ... 25
1.2.1 Synchronous generator model and phasor diagram ... 25
1.2.2 Electrical power and power factor ... 29
1.2.3 Generator air-gap torque model ... 29
2 Interaction of a turbine-generator with the electrical grid ... 31
2.1 Transient events in the electrical grid ... 31
2.2 Unbalanced power grid ... 32
2.3 Subsynchronous resonance ... 34
3 Torsional vibration analysis based on incremental encoder data ... 37
3.1 System structure and input data ... 37
3.2 Encoder geometry and a method of its estimation ... 39
3.2.1 Algorithm for calculating the gap width from measured time increments ... 39
3.2.2 Mathematical model for encoder geometry estimation ... 41
3.2.3 Identification of the parameters of the model of the quantity gap width ... 44
3.2.4 Determination of measurement noise $\eta$ characteristics ($\sigma t$ and $\sigma y$) ... 45
3.2.5 Determination of state noise $\xi$ characteristics ($\sigma\xi$). ... 49
3.2.6 Gap width random variable – running summary ... 51
3.2.7 Kalman filter design for system state estimation ... 51
3.3 Instantaneous angular speed evaluation based on incremental encoder measurement ... 52
3.3.1 Velocity computation by definition ... 53
3.3.2 Velocity computation without encoder geometry compensation ... 53
3.3.3 Velocity computation algorithm incorporating the encoder geometry estimation ... 54
3.4 Error of the encoder geometry and angular speed calculation ... 55
3.4.1 Random measurement noise ... 55
3.4.2 Systematic error of the instantaneous angular speed calculation algorithm ... 56
3.4.3 The problem of oscillation at the rotational frequency and its multiples ... 65

3.5 Programmatic implementation of the algorithm ... 67
4 Practical case studies for the analysis of torsional vibration interaction with the power grid ... 69
4.1 Subsynchronous torsional vibration resonance events ... 69
4.1.1 Subsynchronous resonance and forced vibration ... 70
4.1.2 Subsynchronous resonance and beat phenomenon ... 72
4.1.3 Forced vibration components in all-day spectrograms ... 73
4.2 Torsional vibration response to air-gap torque disturbances ... 75
4.2.1 Three-phase generator terminal short-circuit torsional response diagnostics on RD ... 75
4.2.2 Evaluation of rotor torsional vibration and static torsion ... 78
4.2.3 Evaluation of instantaneous angular speed and generator terminal voltage signals of a 250 MW turbine-generator ... 80
4.2.4 Torsional response of a 250 MW nuclear power plant unit to the outage of a nearby unit with LP turbine blade vibration excitation ... 86
5 Conclusions ... 89
6 Appendices ... 91
6.1 Appendix 1: Incremental encoders ... 91
6.1.1 Optical incremental encoders ... 91
6.1.2 Electromagnetic incremental sensors ... 92
6.2 Appendix 2: Disturbances affecting encoder gap width ... 94
6.2.1 Non-parallelism of the edges of the encoder stripes ... 94
6.2.2 Zebra tape resolution error ... 95
6.3 Appendix 3: Detection times generator ... 95
6.4 Appendix 4: Detection time uncertainty approximation by means of normal distribution ... 97
7 Bibliography ... 99
8 Publications ... 101

# Introduction and objectives of the work

The subject of this dissertation thesis is the design and implementation of a system for monitoring of torsional vibration of a turbine-generator rotor. This task includes both the creation of a suitable measurement chain that will respect a wide range of restrictions resulting from the use of the system in the machine room environment of a power plant, and - in particular - the design and implementation of a suitable signal processing algorithm. From a cybernetic point of view, it will be a system that will have a defined set of input quantities and a set of output quantities, the most important of which will be output information on the amplitude and frequency of torsional oscillations. In addition, the system will be affected by a certain set of disturbance variables, the effect of which will have to be compensated in a suitable way.

The implementation of the torsional vibration monitoring system has one main goal. This is to ensure that the amplitude of torsional vibrations does not exceed some specified safe limits. Exceeding these limits can damage the rotor or some other key components such as turbine blades. Excessive oscillation can take two basic forms. One is long-term oscillation above a certain limit, which leads to so-called high-cycle fatigue. The second possibility are impact events with large instantaneous values of the achieved mechanical stress in the material, which can, at a given moment, cause cracks to appear on the surface of the rotor or at the root of the turbine blades. There have been many cases of severe to catastrophic turbine-generator accidents due to excessive torsional oscillation.

A very specific feature of torsional oscillations is their close connection to events in the power grid. This coupling evolves from the existence of the air-gap torque in the generator, which is dictated by both the instantaneous electrical state of the generator and the instantaneous state of motion of the rotor. Thanks to the existence of this coupling, a wide range of ways in which torsional oscillations can be excited opens up, which of course have no analogues in other types of vibrations. For example, subsynchronous resonance or excitation due to asymmetry in the power grid.

The need for a torsional vibration monitoring system has recently been growing strongly as the structure of the power grid changes. The share of renewable energy sources is increasing, conventional sources are operated in the regime of more frequent starts and shut downs, electrical energy is transmitted over long distances from the place of production (e.g. off-shore wind farms) to the place of consumption. These changes often cause a more frequent change in the operating state of the network and the associated excitation of transient events, which in turn have an effect on the excitation of torsional vibrations of turbine-generators.

Current power plants are not equipped with torsional vibration monitoring systems as standard. Typically, only the lateral and axial vibrations of the rotor are monitored. However, neither of these two quantities is in principle capable of capturing torsional oscillations. Thus, the rotor can vibrate torsionally even with large amplitudes completely unobserved, while the lateral and axial vibrations remain normal. Standardly measured rotor vibrations also have limits clearly defined by the standards, which determine what level of vibration is still safe and at what level it is already necessary to take counteractions. Such limits defined by a standard are unfortunately missing in the case of torsional vibrations. If a system for measuring rotor torsional vibrations is currently installed at a power plant, it is usually an ad-hoc solution, the installation of which was initiated by problems during machine operation in the past. New machines can be equipped with vibration measurement in certain cases, but this is an additional system, the outputs of which are not sufficiently interpretable for the plant operator (What is too much, what is too little? What to do when the vibration is increased?).

The reason why torsional vibration monitoring is not a standard at power plants till this day is probably primarily due to its complex implementation. The fact that torsional vibrations can be reasonably measured only with wireless strain gauges attached to the surface of the rotor or with incremental encoders practically precluded the construction or the economic profitability of such systems in the "analog" era in the 20th century. Only with the rapid development of computer technology and the steep drop in the prices of measuring hardware in recent time, the idea of including torsional vibration monitoring among standard turbogenerator protection systems becomes relevant.

This thesis presents a system for long-term monitoring of torsional vibrations of a turbine-generator rotor. It is a system of own design, the core of which is in advanced signal processing methods. These

methods must be robust enough to provide sufficiently accurate results and still be calculable in real time. In addition, the system was designed from the start with practical use in mind. This condition is absolutely fundamental and has far-reaching consequences on the final form of the proposed system. Starting with the measuring chain, whose set-up has been innovated several times during the development of the system, mainly to ensure its reliability for long-term operation. Ending with the form of the implemented signal processing methods, which must be built in such a way that they are able to overcome practical problems and be robust against applied disturbances.
As this is a doctoral thesis, it must have a clear defined set of problems to solve. The fulfillment of the objectives of the work is an indicator of the quality of the work done by the author/student and a condition for the successful defense of the dissertation. In the following list the objectives of the thesis will be given:

1. monitoring of the interaction between the turbine-generator unit and the electrical grid
2. measurement and evaluation of the torsional vibration signals
3. practical evaluation on data measured in power plants

At the end of this introductory text, we will briefly describe the chapters into which the thesis is divided. The first numbered chapter is the Electromechanical model of rotor torsional vibration. It introduces all the necessary terms and quantities that will be used for the rest of the work. At the same time, basic physical principles are described, the understanding of which is necessary when investigating torsional vibrations.
The second chapter is devoted to the interaction of a turbine-generator with the electrical grid. In this chapter, three phenomena are analysed, which have their origin in the electricity network, but during which the torsional oscillations of the turbine-generator rotor are excited. As will be shown, these phenomena are related either to operations in the power grid or to the state of the power grid as such.
The third chapter is the core of the entire thesis and presents methods for evaluating torsional vibrations from measured signals. As it turns out, the problem of evaluating torsional vibrations from measured data is not trivial and requires multi-stage algorithmic processing. In addition to the derivation of the necessary methods, the chapter also analyses their properties, and in a separate subchapter, the error of the results that the proposed methods give is also analysed in detail.
The fourth chapter validates the results of the proposed methods directly on data from practical operation. The chapter could only be created thanks to the exclusive access to these practical data, which was made possible by the fact that the proposed system was deployed at several power plants in the Czech Republic and around the world during its existence. Due to the variety of locations of the individual installations, the variety of manifestations of torsional vibration, which was already discussed a few paragraphs above, is clearly visible in the results.
The most important outputs of the work are summarized in the Conclusions. In addition, directions for further research are suggested, which have the potential to expand the possibilities of applying the results of the existing system, for example by combining it with the blade vibration monitoring system, or to improve the quality of the system in its current form.
The series of appendices at the end of the work certainly deserve special attention, as they often contain other important findings that were omitted from the main text in order to increase its readability.

# 1 Electromechanical model of rotor torsional vibration

In this chapter the most important physical laws regarding rotor torsional vibration will be explained. Next, some more mathematical expressions will be derived which will further be addressed in later chapters.

## 1.1 Mechanical model – rotor torsional vibration

### 1.1.1 Kinematic model of torsional vibration

Rotor torsional vibration manifests itself as a harmonic oscillation of the rotor angular speed. This is regardless of the axial position on the rotor. An exception from this is the case when torsional vibration is being measured exactly in the node of the oscillation.
If the rotor is subject to torsional vibration of more than one frequency, the resultant motion is the superposition of the harmonic oscillations of the individual frequencies.
Besides the torsional vibration, however, the rotor is rotating with a constant or slowly changing rotational speed $\omega_{rot}$, which is equal to $314\ rad/s$ ($3000\ RPM$) for two-pole machines.
Generally, the rotor instantaneous angular speed $\omega(t)$ can be written as a sum of a constant angular speed $\omega_{rot}$ and the contributions of the individual torsional vibration harmonic components, each having a distinct frequency $f_i$, a phase delay $\phi_i$ and an amplitude $A_i$ in terms of

$$\omega(t) = \omega_{rot} + \sum_{i=1}^{N} A_i \sin(2\pi f_i t + \phi_i)\,. \tag{1.1}$$

By the integration of the instantaneous angular speed signal from Eq. 1.1, the rotor angular position $\varphi(t)$ measured from the beginning of the measurement can be found as

$$\varphi(t) = \int_0^t \omega(\tau)\mathrm{d}\tau\,. \tag{1.2}$$

After the substitution from the Eq 1.1 into the Eq. 1.2,

$$\varphi(t) = \int_0^t \left[\omega_{ot} + \sum_{i=1}^{N} A_i \sin(2\pi f_i \tau + \phi_i)\right] d\tau\,, \tag{1.3}$$

$$\varphi(t) = \omega_{rot} t + \sum_{i=1}^{N} \int_0^t A_i \sin(2\pi f_i \tau + \phi_i)\, d\tau\,, \tag{1.4}$$

$$\varphi(t) = \omega_{rot} t + \sum_{i=1}^{N} \left(\left[-\frac{A_i}{2\pi f_i}\cos(2\pi f_i \tau + \phi_i)\right]_0^t\right) + C, \tag{1.5}$$

$$\varphi(t) = \omega_{rot} t + \sum_{i=1}^{N} \left(-\frac{A_i}{2\pi f_i}\cos(2\pi f_i t + \phi_i) + \frac{A_i}{2\pi f_i}\cos(\phi_i)\right) + C. \tag{1.6}$$

The constant of integration $C$ can be obtained from the initial condition $\varphi(0) = 0$. After the substitution $t = 0$, the first term on the right-hand side is zero, the other terms inside the sum operator diminish and for $\varphi(0) = 0$ to hold the constant of integration must be zero, i.e. $C = 0$. The final expression for absolute rotor angular position having $N$ torsional components is as follows

$$\varphi(t) = \omega_{rot} t + \sum_{i=1}^{N} \left( -\frac{A_i}{2\pi f_i} \cos(2\pi f_i t + \phi_i) + \frac{A_i}{2\pi f_i} \cos(\phi_i) \right). \tag{1.7}$$

### 1.1.2 Rotor static torsion

The term static torsion will be used for the rotor twisting around its longitudinal axis under a torque applied on both of the ends of the rotor. In the state of a static equilibrium, the sum of all torques must be zero. If the rotor is subject to an external torque, the rotor twists, the atomic structure gets deformed and thus a reaction torque appears. In a steady state, the value of this reaction torque is the same as the magnitude of the external torque. Also, the torque is the same along the rotor length.
In addition, for a homogeneous cylindrical rotor the deformation is also constant along its length. As a consequence, the angular deviation of the cross sections of the cylinder changes linearly, as illustrated in Fig. 1.1.

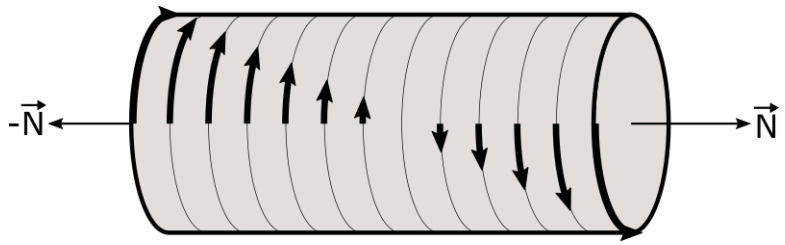


*Fig. 1.1 Rotor torsion as a consequence of two opposite torques* $\mathbf{N}$.

In the following text, the mathematical expressions describing rotor static torsion will be derived. The torsion loading of a cylindrical rotor can be interpreted as deploying a shear stress to individual cylindrical shells, see Fig. 1.2. Thus, shear strain of a cube, also known as Hooke's law for shear stress, can be taken as a starting point,

$$\frac{F}{S} = \mu\theta \tag{1.8}$$

where $F$ is a tangential force acting to the upper surface of the area $S$, $\mu$ is the shear modulus which is a material constant and $\theta$ is the twist angle caused by the force $F$.

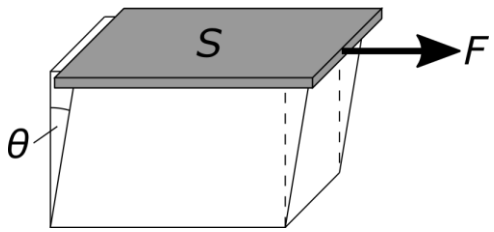


*Fig. 1.2 Twisting of a cube which is subject to shear stress.*

The relation between the twist angle and the external force in Eq. 1.8 provides a starting point for the computation of the twist angle of a homogeneous cylindrical rotor which is subject to an external torque $M$, i.e. in case of a static torsion loading of the rotor. The situation is illustrated in Fig. 1.3.

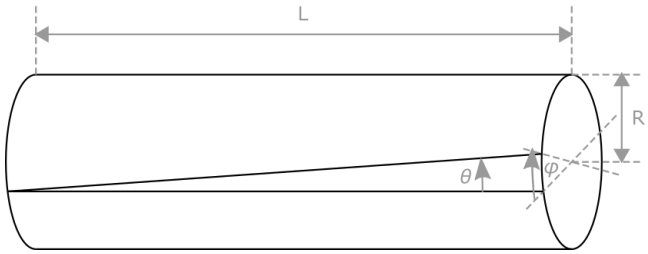


*Fig. 1.3 Twisting of a cylindrical rotor.*

It can be seen that by twisting one end by angle $\varphi$ with respect to the other, the cylindrical surface is subject to a shear deformation of the angle $\theta$. If the twist is small enough, an approximate relation holds

$$\theta L = \varphi R \tag{1.9}$$

The cylindrical rotor can be thought of as a composition of many thin cylindrical shells with their radius changing from zero to the radius $R$ of the rotor. The same effect as depicted in Fig. 1.3 applies for every of the internal cylindrical shells. A detail of one internal cylindrical shell of a radius $0 < r \leq R$ is shown in Fig. 1.4. The twist angle $\theta$ is linearly decreasing from its maximum value for the outermost shell to zero at the rotation axis of the rotor.

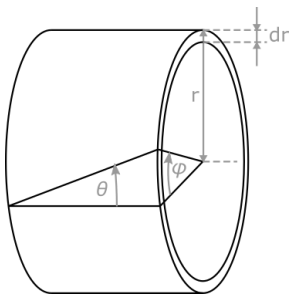


*Fig. 1.4 Twisting of a cylindrical shell.*

For the twist angle $\varphi$ of the cylindrical shell and the angle of torsion displacement $\theta$, the following relation holds

$$\theta L = \varphi r. \tag{1.10}$$

The cylindrical shell transmits a portion $\mathrm{d}M(r)$ of the total torque $M$ so an integral can be written

$$\int_0^R \mathrm{d}M(r) = M. \tag{1.11}$$

The value $\mathrm{d}M(r)$ is related to the tangential force $\mathrm{d}F(r)$ acting on that cylindrical shell to the distance from the axis of rotation by

$$\mathrm{d}M(r) = \mathrm{d}F(r) \cdot r. \tag{1.12}$$

The magnitude of the force $\mathrm{d}F(r)$ can be evaluated by the Eq. 1.8. As $S$ the surface of the cylindrical shell cross section $2\pi r\mathrm{d}r$ is substituted. The twist angle $\theta$ is obtained from Eq. 1.10. The final equation is of the form

$$\mathrm{d}F(r) = \mu \frac{\varphi r}{L} 2\pi r dr. \tag{1.13}$$

The total torque $M$ transmitted by the rotor is obtained by combining Eq. 1.11, Eq. 1.12 and Eq. 1.13 as

$$M = 2\pi\mu \frac{\varphi}{L} \int_0^R r^3 \mathrm{d}r \tag{1.14}$$

and after integration

$$M = \frac{\pi\mu R^4}{2L}\varphi. \tag{1.15}$$

The torque $M$ is thus proportional to the twist angle $\varphi$. The corresponding constant of proportionality is the torsional stiffness

$$k_t = \frac{\pi\mu R^4}{2L} \tag{1.16}$$

that describes the capability of the rotor to oppose an external torque. It can be seen from Eq. 1.16 that torsional stiffness decreases with the length $L$ of the rotor and increases with the fourth power of the diameter $R$. This means also a small change in diameter has a significant effect on the torsional stiffness. Because the torsion angle $\theta$ is proportional to the distance from the rotor axis, also the mechanical stress does so. As a consequence, the maximum mechanical stress is reached on the surface of the rotor. For that reason the cracks caused by excessive torsional stress initiate mainly on the surface of the rotor. The distribution of the mechanical stress on a rotor cross section illustrates Fig. 1.5.

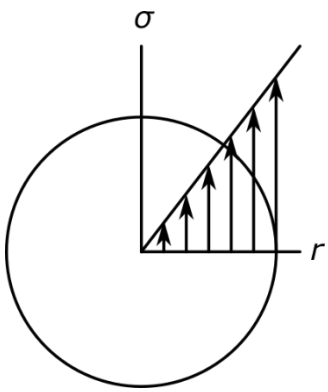


***Fig. 1.5 The distribution of the mechanical stress on a rotor cross section.***

Mechanical stress on the surface of a cylindrical rotor subject to an external torque $M$ can be obtained from Eq. 1.15. Let $\mathrm{d}M$ be a portion of the net torque that is transmitted by the outer cylindrical shell of the thickness $\mathrm{d}r$, thus

$$dM = \frac{\pi\mu R^4\varphi}{2L} - \frac{\pi\mu(R-\mathrm{d}r)^4\varphi}{2L}. \tag{1.17}$$

Under algebraic rules, the fourth power of $(R-\mathrm{d}r)$ can be written as an addition of $R^4 - 4R^3\mathrm{d}r + 6R^2\mathrm{d}r^2 - 4R\mathrm{d}r^3 + \mathrm{d}r^4$. In this expression, the terms with higher power of $\mathrm{d}r$ can be neglected, yielding an approximative form $R^4 - 4R^3\mathrm{d}r$. This is further substituted into Eq. 1.15. The final equation has the form

$$dM = 4\frac{\pi\mu R^4\varphi}{2L}\frac{\mathrm{d}r}{R}. \tag{1.18}$$

Note, that Eq. 1.18 contains a term representing the net torque $M$ from Eq. 1.15. By the substitution into Eq. 1.18, the final form is obtained

$$dM = 4M\frac{\mathrm{d}r}{R}. \tag{1.19}$$

The mechanical stress acting on the outer shell is

$$\sigma = \frac{dF}{dS} = \frac{dM/R}{dS}. \tag{1.20}$$

The substitution for $\mathrm{d}M$ from Eq. 1.19 and for $dS = 2\pi R\mathrm{d}r$ yields

$$\sigma = \frac{2M}{\pi R^3}. \tag{1.21}$$

Equation 1.21 describes the relation between the net torque transmitted by a homogeneous cylindrical rotor and the maximum value of the mechanical stress that appears on the surface of the rotor.

The above discussion may be applied to the evaluation of mechanical stress on a turbine-generator rotor. Here, however, the existence of stress concentrators is an additional issue that must also be considered. These include locations where the rotor cross section has a shape that differs from a circular one such as the whole length of the generator rotor that has drilled longitudinal slots for rotor winding. Other example are locations on turbine tailored to the attachment of bladed discs. As stress concentrators act also locations of rotor diameter change.

### 1.1.3 Torsional vibration of a discrete oscillator

In the last chapter the response of the rotor subject to an external static torque has been addressed. The focus of this chapter will be the dynamic torsional response of the rotor. The free torsional oscillations, torsional natural frequencies and natural shapes are the highlights. For reference, a detailed guide regarding torsional vibration of mechanical systems can be found in [32].
Free torsional oscillations is a state of a repetitive transformation of kinetic and potential energy between distinct parts of a rotor. Kinetic energy is linked to a motion of the rotor. Potential energy is linked to the deformation of the material of the rotor caused by its twisting. This energy is nonzero every time there are portions of the rotor which are twisted to each other related to the steady state.
The simplest example of free torsional oscillations is a system of two mass discs connected by a massless torsional spring, see Fig. 1.6. Considering a small initial deviation the spring develops a torque that acts in an opposite direction thus trying to take the rotor back to the equilibrium. The velocity of the discs gradually increases and thereby also the kinetic energy increases. The spring acts with a non-zero torque until the deformation is zero and the rotor reaches equilibrium. In that position, potential energy is zero and it is fully transformed into the kinetic energy that reaches its maximum. However, the process does not end by reaching equilibrium but, due to inertia, the rotor starts to deviate in an opposite direction. Hereby, the spring is again being deformed and acting on the rotor in a way to slow down the rotor and bring it back to equilibrium. The kinetic energy is again transforming to the potential energy. In case of zero friction, the motion will never end and the system will oscillate at its torsional natural frequency forever.

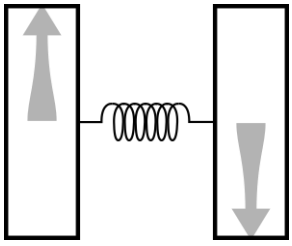

***Fig. 1.6 The simplest example of free torsional oscillations.***

For the system in Fig. 1.6 the torsional natural frequency as a function of blade inertia $I$ and torsional spring stiffness $k_t$ can easily be obtained. Thanks to the symmetry of the mechanical system the deviation of each of the two discs will be equal but opposite at each time. The point in the middle of the spring will be still and is called a node. The computation can thus be made for a simplified system consisting of one bladed disc and a torsional spring of half the length (i.e. double stiffness $k_t{}' = 2k_t$) fixed on one end.
The Newton's second law for rotational motion can be used as a starting point

$$M(t) = I\epsilon(t), \tag{1.22}$$

where $M(t)$ is the torque acting on the disc, $I$ is the moment of inertia of the disc and $\epsilon(t)$ is its angular acceleration. The torque $M$ is caused exclusively by the torsional spring, it has the opposite sign than

the deviation and its amplitude depends on the torsional stiffness $k_t' = 2k_t$ and on the deviation $\varphi$ of the disc according to Hooke's law

$$M(t) = -k_t'\varphi(t) = -2k_t\varphi(t). \tag{1.23}$$

Combining Eq. 1.22 and Eq. 1.23 and considering that the angular acceleration $\epsilon(t)$ is the second time derivative of angular deviation $\varphi(t)$, the equation of motion of the free oscillations of the mechanical system is

$$\ddot{\varphi}(t) + \frac{2k_t}{I}\varphi(t) = 0. \tag{1.24}$$

Eq. 1.24 is a differential equation where a substitution $\omega^2 \equiv \frac{2k_t}{I}$ can be applied. The two solutions of the characteristic equation

$$\lambda^2 + \omega^2 = 0 \tag{1.25}$$

are $\lambda_{1,2} = \pm i\omega$. A general solution of the Eq. 1.25 has the form

$$\varphi(t) = C_1 e^{\lambda_1 t} + C_2 e^{\lambda_2 t}. \tag{1.26}$$

$C_1$ and $C_2$ are constants which can be determined by the initial conditions. These are the nonzero deviation from equilibrium $\varphi(0) = \varphi_0$ and a nonzero initial velocity $\dot{\varphi}(0) = 0$.

$$\varphi(0) = C_1 e^{\lambda_1 \cdot 0} + C_2 e^{\lambda_2 \cdot 0} = C_1 + C_2 = \varphi_0$$

$$\dot{\varphi}(0) = \lambda_1 C_1 e^{\lambda_1 \cdot 0} + \lambda_2 C_2 e^{\lambda_2 \cdot 0} = \omega(C_1 - C_2) = 0$$

This is a couple of linear equations for two unknowns $C_1$ and $C_2$. The solution is $C_1 = C_2 = \varphi_0/2$. By the substitution into Eq 1.26 we have

$$\varphi(t) = \frac{\varphi_0}{2} e^{i\omega t} + \frac{\varphi_0}{2} e^{-i\omega t}, \tag{1.27}$$

which can be simplified using Euler's identity to

$$\varphi(t) = \varphi_0 \cos \omega t\,. \tag{1.28}$$

With respect to Eq 1.28 the quantity $\omega$ can be interpreted as angular frequency of the free torsional oscillations, i.e. the torsional natural frequency

$$\omega = \sqrt{k_t'/I}. \tag{1.29}$$

The oscillatory motion discussed above is the only one for that mechanical system that can exist without any external torques. For more complicated mechanical systems with more discs and springs there will also be a larger number of torsional natural shapes and frequencies. It's a fact, that for a general torsional system with $N$ discs connected by $N-1$ springs there are always $N-1$ torsional natural frequencies of the natural oscillations. Actually, there is always one more natural frequency with the value of 0 corresponding to a trivial case of uniform rotation of the whole system. Considering also this frequency, there is a total of $N$ torsional natural frequencies.

### 1.1.4 Continuous body torsional vibration

In the next section the torsional natural frequency of a homogeneous cylindrical rotor will be derived. Let $R$ be the radius of the rotor and $L$ its length. Next, let $\varphi_1 = \varphi_1(t)$, $\varphi_2 = \varphi_2(t)$ and $\varphi = \varphi(x,t)$ denote the angular deviation at the two rotor ends and in an arbitrary position $x$.

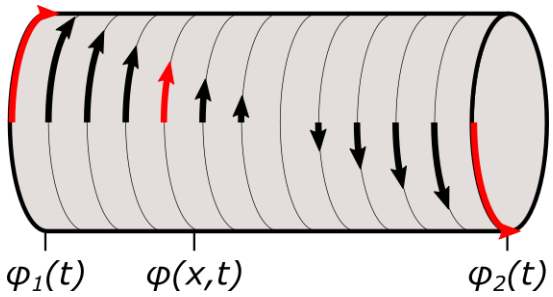


*Fig. 1.7 To the rotor torsional vibration.*

Thanks to symmetry, the angular displacement is linearly distributed along the rotor length, thus

$$\varphi(x,t) = c_0(t) + c_1(t)x, \tag{1.30}$$

and this can be written as

$$\varphi(x,t) = \boldsymbol{\phi}^T(x) \cdot \boldsymbol{c}(t), \tag{1.31}$$

where $\boldsymbol{\phi}(x) = [1, x]^T$ a $\boldsymbol{c}(t) = [c_0(t),\ c_1(t)]^T$. Defining a vector of boundary displacements $\boldsymbol{q}(t) = [\varphi_1(t), \varphi_2(t)]^T$ the angular displacement in an arbitrary position can be computed as

$$\boldsymbol{q}(t) = \begin{bmatrix} \varphi_1(t) \\ \varphi_2(t) \end{bmatrix} = \begin{bmatrix} 1 & 0 \\ 1 & L \end{bmatrix} \begin{bmatrix} c_0(t) \\ c_1(t) \end{bmatrix} = \boldsymbol{S} \cdot \boldsymbol{c}(t). \tag{1.32}$$

Next, both sides of Eq. 1.32 can be multiplied by the inversion of a regular matrix $\boldsymbol{S}$ which gives $\boldsymbol{c}(t)$ as

$$\boldsymbol{c}(t) = \boldsymbol{S}^{-1}\boldsymbol{q}(t), \tag{1.33}$$

where

$$\boldsymbol{S}^{-1} = \begin{bmatrix} 1 & 0 \\ -\frac{1}{L} & \frac{1}{L} \end{bmatrix}. \tag{1.34}$$

By the substitution for $\boldsymbol{c}(t)$ from Eq.1.33 into Eq. 1.31, we get

$$\varphi(x,t) = \boldsymbol{\phi}^T(x)\boldsymbol{S}^{-1}\boldsymbol{q}(t). \tag{1.35}$$

In the following the kinetic and potential energy of the rotor will be computed. Kinetic energy of an infinite small rotor element is given by its instantaneous angular speed $\dot{\varphi}(x,t)$,

$$\dot{\varphi}(x,t) = \boldsymbol{\phi}^T(x)\boldsymbol{S}^{-1}\dot{\boldsymbol{q}}(t), \tag{1.36}$$

and its moment of inertia which is given by

$$dI = \rho J_p dx, \tag{1.37}$$

where $\rho$ is the density of the rotor material and $J_p$ is the polar moment of inertia. The kinetic energy of the element is then expressed as

$$dE_k = \frac{1}{2}\dot{\varphi}^2(x,t)\ \mathrm{d}I. \tag{1.38}$$

The kinetic energy of the whole rotor is obtained by the integration over its full length

$$E_k = \int_{(I)} \frac{1}{2}\dot{\varphi}^2(x,t)\, dI = \int_0^L \frac{1}{2}\dot{\boldsymbol{q}}^T(t)\boldsymbol{S}^{-T}\boldsymbol{\phi}^T(x)\boldsymbol{\phi}(x)\boldsymbol{S}^{-1}\dot{\boldsymbol{q}}(t)\, \rho J_p dx$$
$$= \frac{1}{2}\dot{\boldsymbol{q}}^T(t)\left[\boldsymbol{S}^{-T}\left(\rho J_p \int_0^l \boldsymbol{\phi}^T(x)\boldsymbol{\phi}(x)dx\right)\boldsymbol{S}^{-1}\right]\dot{\boldsymbol{q}}(t)$$
$$= \frac{1}{2}\dot{\boldsymbol{q}}^T(t)\boldsymbol{M}\dot{\boldsymbol{q}}(t). \qquad (1.39)$$

The integral within the braces can be computed as follows

$$\int_0^L \boldsymbol{\phi}^T(x)\boldsymbol{\phi}(x)dx = \int_0^L \begin{bmatrix}1\\x\end{bmatrix}[1,x]dx = \int_0^L \begin{bmatrix}1 & x\\ x & x^2\end{bmatrix}dx = L\begin{bmatrix}1 & \frac{L}{2}\\ \frac{L}{2} & \frac{L^2}{3}\end{bmatrix}. \qquad (1.40)$$

The matrix $\boldsymbol{M}$ is then given by

$$\boldsymbol{M} = \rho J_p l \begin{bmatrix}1 & -\frac{1}{L}\\ 0 & \frac{1}{L}\end{bmatrix}\begin{bmatrix}1 & \frac{L}{2}\\ \frac{L}{2} & \frac{L^2}{3}\end{bmatrix}\begin{bmatrix}1 & 0\\ -\frac{1}{L} & \frac{1}{L}\end{bmatrix} = I\begin{bmatrix}\frac{1}{3} & \frac{1}{6}\\ \frac{1}{6} & \frac{1}{3}\end{bmatrix} \qquad (1.41)$$

where $I$ is the moment of inertia of the whole rotor. The kinetic energy of the rotor is

$$E_k = \frac{1}{2}I\dot{\boldsymbol{q}}^T(t)\dot{\boldsymbol{q}}(t). \qquad (1.42)$$

The potential energy of the rotor is given by the integral of the deformation energy density $\lambda$ over the volume of the whole rotor

$$E_p = \int_{(V)} \lambda dV\,, \qquad (1.43)$$

where $\lambda$ is given by

$$\lambda = \frac{1}{2}\mu\theta^2. \qquad (1.44)$$

Considering the relation between the shear deformation angle and the deviation of the rotor cross section (see Eq. 1.9), we get

$$\theta = \frac{\partial\varphi}{\partial x}R, \qquad (1.45)$$

and after substitution from Eq. 1.36

$$\theta = \frac{\partial\boldsymbol{\phi}^T(x)}{\partial x}\boldsymbol{S}^{-1}\boldsymbol{q}(t)R, \qquad (1.46)$$

the Eq. 1.43 can be written as

$$E_p = \frac{1}{2}\int_0^L \int_{(A)} \mu \boldsymbol{q}^T(t)\boldsymbol{S}^{-T}\frac{\partial \boldsymbol{\phi}^T(x)}{\partial x}\frac{\partial \boldsymbol{\phi}(x)}{\partial x}\boldsymbol{S}^{-1}\boldsymbol{q}(t) r^2 dA\, dx$$

$$= \frac{1}{2}\int_0^L \mu \boldsymbol{q}^T(t)\boldsymbol{S}^{-T}\frac{\partial \boldsymbol{\phi}^T(x)}{\partial x}\frac{\partial \boldsymbol{\phi}(x)}{\partial x}\boldsymbol{S}^{-1}\boldsymbol{q}(t) \int_{(A)} r^2 dA\, dx$$

$$= \frac{1}{2}\boldsymbol{q}^T(t)\left[\boldsymbol{S}^{-T}\left(\int_0^L \mu J_p \frac{\partial \boldsymbol{\phi}^T(x)}{\partial x}\frac{\partial \boldsymbol{\phi}(x)}{\partial x} dx\right)\boldsymbol{S}^{-1}\right]\boldsymbol{q}(t)$$

$$= \frac{1}{2}\boldsymbol{q}^T(t)\boldsymbol{K}\boldsymbol{q}(t). \tag{1.47}$$

For the integral within the braces we have

$$\int_0^L \frac{\partial \boldsymbol{\phi}^T(x)}{\partial x}\frac{\partial \boldsymbol{\phi}(x)}{\partial x} dx = \int_0^L \begin{bmatrix}0\\1\end{bmatrix}[0,1]dx = \int_0^L \begin{bmatrix}0 & 0\\0 & 1\end{bmatrix} dx = L\begin{bmatrix}0 & 0\\0 & 1\end{bmatrix}. \tag{1.48}$$

The matrix $\boldsymbol{K}$ is then given by

$$\boldsymbol{K} = \mu J_p L \begin{bmatrix}1 & -\frac{1}{L}\\ 0 & \frac{1}{L}\end{bmatrix}\begin{bmatrix}0 & 0\\0 & 1\end{bmatrix}\begin{bmatrix}1 & 0\\ -\frac{1}{L} & \frac{1}{L}\end{bmatrix} = k_t\begin{bmatrix}1 & -1\\ -1 & 1\end{bmatrix}, \tag{1.49}$$

where $k_t$ is the rotor torsional stiffness defined by Eq. 1.16. The potential energy is given by

$$E_p = \frac{1}{2}k_t \boldsymbol{q}^T(t)\boldsymbol{q}(t) \tag{1.50}$$

The problem of free torsional oscillations of a homogeneous cylindrical rotor is symmetrical, thus in every time the ends of the rotor are deviated by the same angle. Here, two distinct cases are possible:

- The opposite ends move in the same direction

$$\boldsymbol{q}(t) = \begin{bmatrix}\varphi(t)\\ \varphi(t)\end{bmatrix} \tag{1.51}$$

- The opposite ends move in opposite direction

$$\boldsymbol{q}(t) = \begin{bmatrix}\varphi(t)\\ -\varphi(t)\end{bmatrix} \tag{1.52}$$

Substituting Eq. 1.51 into the equation for the kinetic energy Eq 1.42 and potential energy Eq. 1.50 we get

$$E_k = I\dot{\varphi}^2(t) \tag{1.53}$$

$$E_p = k_t\varphi^2(t) \tag{1.54}$$

The mechanical system has one generalized coordinate and so the Lagrange equation has the form

$$\frac{d}{dt}\left(\frac{\partial E_k}{\partial \dot{\varphi}}\right) - \frac{\partial E_k}{\partial \varphi} + \frac{\partial E_p}{\partial \varphi} = 0 \tag{1.55}$$

where

$$\frac{d}{dt}\left(\frac{\partial E_k}{\partial \dot{\varphi}}\right) = 2I\ddot{\varphi}(t), \tag{1.56}$$

$$\frac{\partial E_k}{\partial \varphi} = 0 \text{ a} \tag{1.57}$$

$$\frac{\partial E_p}{\partial \varphi} = 2k_t\varphi(t) \tag{1.58}$$

Substituting into the Lagrange equation we have the equation of motion describing the free torsional oscillations

$$I\ddot{\varphi}(t) + k_t\varphi(t) = 0, \tag{1.59}$$

the solution of which is

$$\varphi(t) = \varphi_0 \cos\left(\sqrt{k_t/I} \cdot t\right). \tag{1.60}$$

Thus, the natural frequency $\omega$ of the torsional oscillations is

$$\omega = \sqrt{k_t/I} \tag{1.61}$$

Eq. 1.61 defines the frequency of the first natural shape of the torsional oscillations of a homogeneous cylindrical rotor. The computation of higher frequencies would be a more complicated problem which is usually solved by numerical solvers, such as the software Ansys.

### 1.1.5 Specifics of large turbine-generators

For the sake of an *exact* analysis of natural shapes and frequencies of more complicated rotors, the best and often the only way to do this is the use of specialized programs. In this chapter a method for *approximate* natural shapes evaluation is presented. The method was published by Giesecke in [8] and it can be used especially there, where no exact geometrical model of the rotor is available. The analysis can be useful for example to decide where to place the torsion measurement sensors.
The starting point is the fact that large turbine-generators typically consist of several bodies. These are the turbine segments, the generator rotor and the exciter. These are massive objects of relatively large torsional stiffness. Between these bodies there is the rotor shaft of a relatively small diameter and thus small torsional stiffness (see the fourth power of the diameter in Eq. 1.16).
A rotor built of $N$ rotor bodies has $N - 1$ natural torsional shapes which correspond to such a kind of torsional oscillation where the main torsional strain manifests on the low-diameter connecting shafts and the individual rotor bodies behave as rigid bodies. Thus, at these low frequencies the rotor can be thought of as a spring-mass system similar to that analysed in 1.1.3

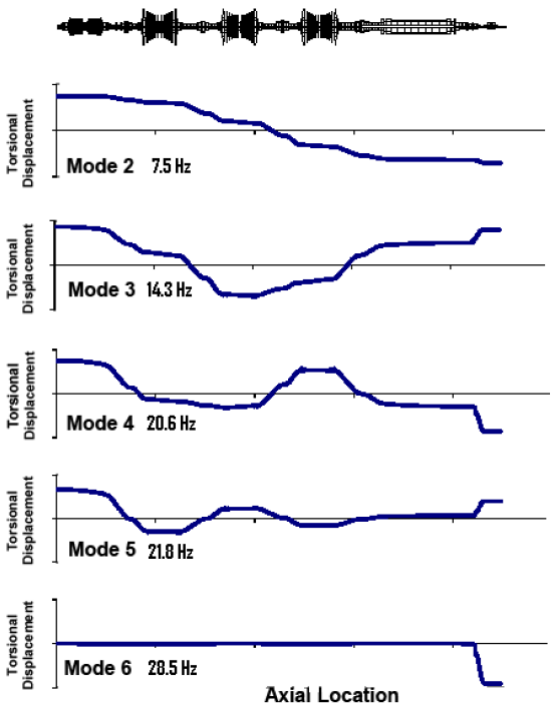


*Fig. 1.8 Subsynchronous natural shapes of a 1800 RPM rotor, adapted from [8].*

The Fig. 1.8 shows subsynchronous natural shapes of a large turbine-generator rotor for a nuclear power plant. The nominal rotational speed of the rotor is 1800 RPM. The individual modes are numbered starting at 2 as the first torsional mode corresponds to the trivial case of constant speed rotation with no

torsional deformation of the rotor. The mode no. 2 is the natural shape of the rotor for the lowest natural frequency where the rotor ends oscillate in the opposite direction to each other and the trend of the torsional dislocation between them is a monotonous function. Every subsequent mode adds one node to the natural shape and one local antinode. Eventually, every rotor body oscillates in an opposite direction to the surrounding bodies in case of the last - 6th – mode (although not very apparent in the figure).
It can be seen that for every mode the trend of the torsional displacement is approximately constant and changes only along the connecting shafts. This corresponds to the fact that for subsynchronous torsional modes the major part of the torsional displacement occurs at the connecting shafts whereas the rotor bodies act as rigid bodies, thus the rotor acting as a spring-mass system.

In case of higher modes the torsional deformation starts to be significant also at the rotor bodies. One group of these natural modes is presented by the coupled blade-shaft oscillation where the blades of the largest low-pressure turbine couple with the rotor. For the turbine-generator being studied there are 9 such shapes in total.

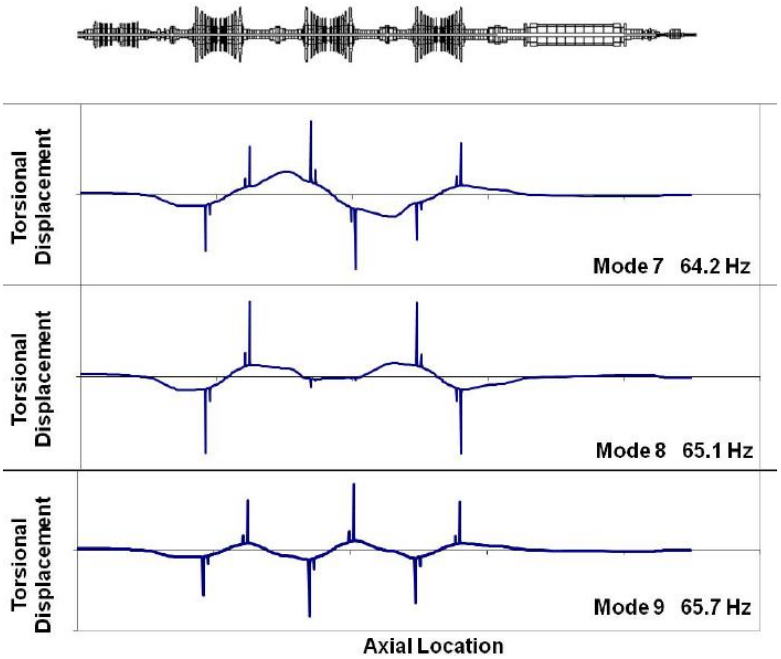


*Fig. 1.9 Example of the first LP twisting modes of the turbine-generator coupled with the L-0 umbrella modes where the blades vibrate in the same direction as the rotor. Both L-0 and L-1 blade rows participate. Adopted from [8].*

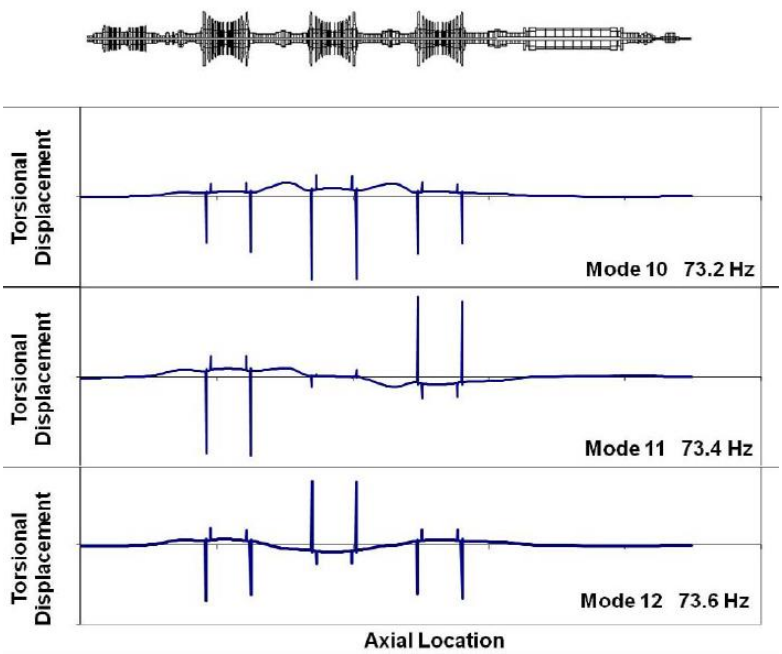


*Fig. 1.10 Example of the first L-0 umbrella modes of the turbine-generator. Adopted from [8].*

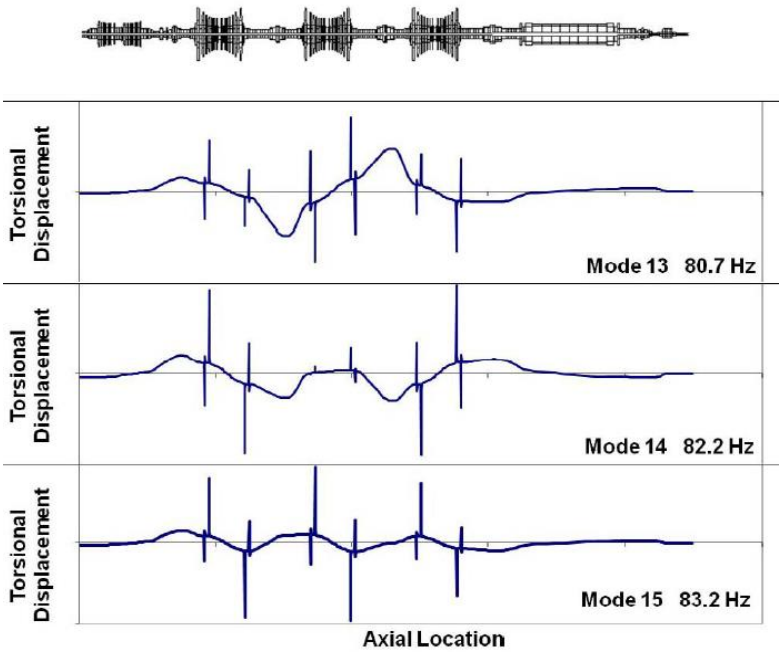


*Fig. 1.11 Example of the first LP twisting modes of the turbine-generator coupled with the L-0 umbrella modes where the blades vibrate in the opposite direction to the rotor. Adopted from [8].*

Besides the above listed twisting modes there is, theoretically, an infinite number of other torsional natural modes at higher natural frequencies. Their practical importance, however, gradually decreases as for high natural frequencies, significantly more energy is needed for the displacements to be a hazard. A special attention, however, should be paid for torsional modes near twice the grid frequency as this frequency can be considerably excited by the generator rotor at some typical circumstances (see Chapter 2.2).

## 1.2 Electrical model – synchronous generator

The most characteristic property of torsional vibration is its relation to events occurring in the electrical grid. Changes in the generator air-gap torque are the main source of torsional vibration excitation. This is something very unique compared to other types of turbine-generator vibration that is, for example, excited by rotor unbalance or by aerodynamic forces.
The fact that torsional vibration is mainly caused by the power grid events has one benefit. The information of the state of the power grid, if known, can be used to determine the excitation of the torsional vibration, both qualitatively and quantitatively. This makes torsional vibration different from other kinds of vibration where the excitation forces can usually not be determined.
In the beginning of this chapter we present a standard synchronous machine electrical model and the derivation of the phasor diagram. Afterwards, we present the fundamental equations for active power and for the power factor. Finally, we present the equations that determine the air-gap torque of the generator.

### 1.2.1 Synchronous generator model and phasor diagram

In this chapter the principle of a synchronous generator will be explained. This will be necessary to grasp the mutual relation between torsional vibration and electrical grid where the generator acts as the linking element. In addition, mathematical equations will be derived in order to formulate the equation of the air-gap torque. Equations and notation is adopted from [15].
A synchronous generator consists of a rotor and a stator part. The rotor supports the rotor winding that acts as a simple coil whereas the stator consists of three stator windings forming three coils displaced by 120° from each other. Although this generator design is not the only one being used it is probably the most common and the rest of this text will refer to this design pattern. This kind of a generator is called two-pole. The situation is depicted in Fig. 1.12.

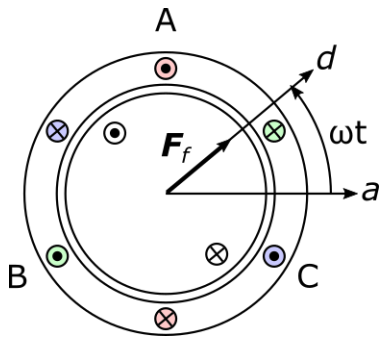


*Fig. 1.12 Schema of a two-pole three-phase synchronous rotor.*

The rotor winding is supplied by an exciter that is a separate element with a constant direct current called field current, $i_f$. The field current creates a constant magnetomotive force $F_f$

$$F_f = N_f i_f, \tag{1.62}$$

where $N_f$ is the number of turns of the rotor winding. The field mmf $F_f$ creates a magnetic flux $\phi_f$ that, according to Ohm's law for a magnetic circuit, is equal to

$$\phi_f = \frac{F_f}{\Re}, \tag{1.63}$$

where $\Re$ is the reluctance of the magnetic current, i.e. the ability to conduct magnetic field. The reluctance is mainly dependent on the thickness of the air-gap between rotor and stator. This air-gap is constant all over the rotor circumference, thus the reluctance $\Re$ does not depend on the actual angular position of the rotor. As a consequence, neither the magnetic flux $\phi_f$ depends on the angular position.
The magnetic flux $\phi_f$ intersects the stator windings of the three phases. As a consequence the mutual magnetic fluxes $\psi_{fA}$, $\psi_{fB}$ and $\psi_{fC}$ are built. During the rotor rotation, the mutual magnetic flux at a

certain phase is changing harmonically with a frequency that is equal to the rotational frequency $\omega$ of the rotor and with an amplitude $\psi_f$. For phase A it reaches its maximum each time the $d$-axis is aligned with the $a$-axis. This is mathematically expressed by a cosine function as

$$\psi_{fA}(t) = \psi_f \cos \omega t\,. \tag{1.64}$$

For the other phases B and C an analogous relation can be determined. Considering that their phase delay relative to the reference $a$-axis are $2\pi/3$ and $4\pi/3$ respectively, we have

$$\psi_{fB}(t) = \psi_f \cos(\omega t - 2\pi/3)\,, \tag{1.65}$$

$$\psi_{fC}(t) = \psi_f \cos(\omega t - 4\pi/3)\,. \tag{1.66}$$

The amplitude $\psi_f$ is given by the product of magnetic flux $\phi_f$ and the number of armature winding turns $N_\phi$. This can be written as a product of the mutual inductance of the rotor winding with one of the stator windings $M_f$ and the field current $i_f$ as

$$\psi_f = N_\phi \phi_f = \frac{N_\phi N_f}{\mathfrak{R}} i_f = M_f i_f. \tag{1.67}$$

The mutual flux through the armature windings of individual phases changes in time. As a result the electromotive force (emf) is induced in armature windings. For the phase A, the induced emf $e_{fA}$ is given by

$$e_{fA}(t) = -\frac{\mathrm{d}\psi_{fA}(t)}{\mathrm{d}t} = \omega M_f i_f \sin \omega t\,. \tag{1.68}$$

This emf would appear on the generator terminal if the generator was disconnected from the grid. Because the voltage has a harmonic trend with an amplitude equal to $\omega M_f i_f$ its effective (rms) value $E$ is given by

$$E = \frac{1}{\sqrt{2}} \omega M_f i_f. \tag{1.69}$$

However, if the generator is connected to the grid, there is a nonzero alternating current in the armature winding which can be written for individual phases as

$$i_A = I_m \cos(\omega t - \lambda)\,. \tag{1.70}$$

$$i_B = I_m \cos(\omega t - 2\pi/3 - \lambda)\,. \tag{1.71}$$

$$i_C = I_m \cos(\omega t - 4\pi/3 - \lambda)\,. \tag{1.72}$$

where $I_m$ is the armature alternating current amplitude and $\lambda$ is a phase delay between rotor actual angular position and the armature winding phasor. Typically, $\lambda \in (\pi/2,\ \pi)$.
The time change of the armature current in each phase gives rise to mmf which act in the direction of the axis of each phase and whose instantaneous amplitude is given by

$$F_A(t) = N_a I_m \cos(\omega t - \lambda)\,, \tag{1.73}$$

$$F_B(t) = N_a I_m \cos(\omega t - 2\pi/3 - \lambda)\,, \tag{1.74}$$

$$F_C(t) = N_a I_m \cos(\omega t - 4\pi/3 - \lambda)\,, \tag{1.75}$$

The constant term $N_a = 2N_\phi/\pi$ is interpreted as the effective number of armature winding turns. It counts for various effects related to the geometry of the stator such as the varying surface of the turns wound on the cylindrical rotor. Adding the mmf vectors of all the armature windings the resultant mmf is obtained

$$\boldsymbol{F}_a(t) = \boldsymbol{F}_A(t) + \boldsymbol{F}_B(t) + \boldsymbol{F}_C(t), \tag{1.76}$$

which can after some algebraic operations rewritten as

$$\boldsymbol{F}_a(t) = 1{,}5 N_a I_m e^{j(\omega t - \lambda)}, \tag{1.77}$$

In Eq. 1.77 the vector is written as a complex number. By doing that, the real axis has been identified with the $a$-axis and the imaginary axis is perpendicular to the $a$-axis. Note, that the resultant armature mmf $\boldsymbol{F}_a(t)$ has a constant amplitude which is 1,5 times greater than the amplitude of the mmf of individual phases. Next, it rotates at the same speed as the rotor and it has a phase delay $\lambda$.
Figure 4.13 shows the time trends of the instantaneous amplitudes of the vectors $\boldsymbol{F}_A(t)$, $\boldsymbol{F}_B(t)$ and $\boldsymbol{F}_C(t)$. Figure 4.14 shows how the mmf vectors are spatially composed to the resultant mmf $\boldsymbol{F}_a(t)$ according to Eq. 1.76.

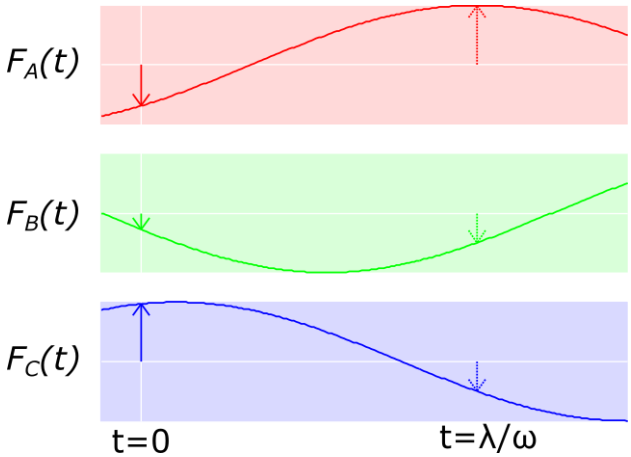


*Fig. 1.13 Time trend of the absolute values of vectors $\boldsymbol{F}_A(t)$, $\boldsymbol{F}_B(t)$ a $\boldsymbol{F}_C(t)$.*

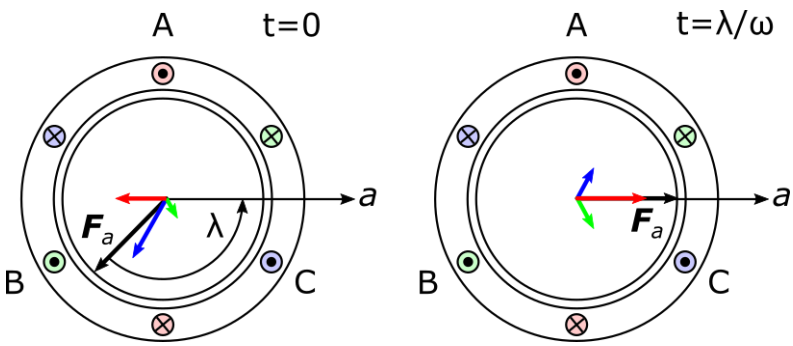


*Fig. 1.14 Resultant armature mmf $\boldsymbol{F}_a(t)$.*

Hence, there are two different rotating mmf inside a synchronous generator. The first one is induced by the direct current going through the field winding and is therefore rotating together with the rotor. The second one is induced by the alternating current going through armature winding and is rotating thanks to the interplay of the time delay and winding position effects. Because the rotational velocity of both of these mmfs is the same, their angular difference is constant in time and the vector of the resultant mmf can be constructed as

$$\boldsymbol{F}_r(t) = \boldsymbol{F}_f(t) + \boldsymbol{F}_a(t). \tag{1.78}$$

All three vectors in Eq. 1.78 form a fixed shape that is rotating with a constant velocity. This shape is depicted in Fig. 1.15.

*Fig. 1.15 Construction of the resultant magnetic field $\mathbf{F}_r$ as a superposition of the armature mmf $\boldsymbol{F}_a$ and field mmf $\mathbf{F}_f$.*

The rotating magnetic field caused by the mmf $\boldsymbol{F}_a(t)$ induces time varying flux linkages in armature winding. This, in turn, induces electromotive force in the armature winding.
Because of the effect of rotation the instantaneous amplitude of the projection of the vector $\boldsymbol{F}_a(t)$ in the $a$-axis is given by

$$F_{aA}(t) = F_a \cos(\omega t - \lambda) = 1{,}5 N_a I_m \cos(\omega t - \lambda)\,. \tag{1.79}$$

The respective flux linkage is given by

$$\psi_{aA}(t) = \frac{N_\phi F_{aA}(t)}{\mathfrak{R}} = \frac{1{,}5 N_\phi N_a}{\mathfrak{R}} I_m \cos(\omega t - \lambda) = L_a I_m \cos(\omega t - \lambda)\,, \tag{1.80}$$

where $L_a$ is the armature reaction inductance. This time changing flux induces the armature reaction emf $e_{aA}$, which is equal to

$$e_{aA}(t) = -\frac{\mathrm{d}\psi_{aA}(t)}{\mathrm{d}t} = \omega L_a I_m \sin(\omega t - \lambda)\,. \tag{1.81}$$

The term $\omega L_a$ can be interpreted as armature reaction reactance $X_a$. From Eq. 1.81 it is also apparent that the induced emf $e_{aA}$ is delayed by $\pi/2$ behind the armature current.
The resultant voltage at phase A is given by the superposition of $e_{fA}(t)$ from Eq. 1.68 and $e_{aA}(t)$ from Eq. 1.81.

$$e_{rA}(t) = e_{fA}(t) + e_{aA}(t). \tag{1.82}$$

The term $e_{rA}(t)$ is the instantaneous terminal voltage at phase A of a generator connected to the grid. Because both terms on the right hand side of Eq. 1.82 are harmonic functions of the same frequency, the emf $e_{rA}(t)$ is also a harmonic function that can be written as a phasor $\underline{V_g}$

$$\underline{V_g} = \underline{E} - jX_a\underline{I}. \tag{1.83}$$

Figure 1.16 shows the relation between the phasors $\underline{V_g}$, $\underline{E}$ and $jX_a\underline{I}$. It is called the phasor diagram of a synchronous machine. In addition, the vectors of the mmfs are also depicted in the phasor diagram.

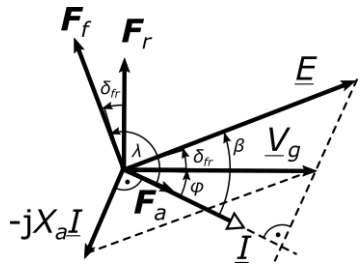


*Fig. 1.16 Phasor diagram of a synchronous machine.*

The vectors $\boldsymbol{F}_f$ and $\boldsymbol{F}_r$ make a constant angle $\delta_{fr}$ which is called the torque angle. It tells how much the rotor advances its equilibrium position in the stator magnetic field. This angle also tells about the phase delay between the emf phasor $\underline{E}$ and the terminal voltage $\underline{V_g}$. Another angle in the diagram is $\varphi$ which presents the power factor angle. This is the angle between the terminal voltage and current and thus determines the ratio between the active power $P$ and reactive power $Q$ of the machine.

For a better understanding of the mentioned derivation leading to the phasor diagram of a synchronous machine, in which a large number of interdependent quantities appear, it will be useful to clarify which quantities are the physical "cause" and which are the "effect". When deriving the phase diagram, the stator currents were used, from which the induced magnetomotive force in the stator winding $\boldsymbol{F}_a(t)$ was subsequently derived. Next, the resultant generator mmf $\boldsymbol{F}_r(t)$ was computed and finally the generator terminal voltage $\underline{V_g}$ was computed. In reality, however, there is a different cause-consequence sequence. Instead, the terminal voltage $\underline{V_g}$ is fixed as it is dictated by the electrical grid (large interconnected grid) and is independent of the actual state of the machine. So, the terminal voltage in fact acts as a starting point for the other quantities. On the contrary, the internal emf $\underline{E}$ depends solely on the actual state of the generator (rotor position and field current) and is independent of the state of the power grid. Armature currents arise as a *consequence* of the relative phase delay and amplitude of the two phasors $\underline{V_g}$ and $\underline{E}$. Referring to Fig. 1.16 it can be said that the phasors $\underline{V_g}$ and $\underline{E}$ are given and the phasors $\underline{I}$ or $\underline{E_a} = -jX_a\underline{I}$ are formed in such a way for the equation $\underline{V_g} = \underline{E} - \underline{E_a}$ to hold.

### 1.2.2 Electrical power and power factor

For a three phase synchronous generator, the active power $P$ is standardly calculated as

$$P = 3IV_g \cos\varphi\,, \tag{1.84}$$

where $I$ is the armature current, $V_g$ is the terminal voltage and $\varphi$ is the power factor. Looking at the phasor diagram, we can note the equivalence

$$V_g \cos\varphi = E\cos(\varphi + \delta) \tag{1.85}$$

which allows us to rewrite Eq. 1.84 as

$$P = 3IE\cos(\varphi + \delta)\,, \tag{1.86}$$

which also reflects the value of the field electromotive force $E$ and the load angle $\delta$.

Under typical circumstances, the phasor diagram is constructed based on the values of the quantities $P$, $Q$ and $V_g$ as these are the commonly measured quantities on a generator. From these the armature current can be determined as

$$I = \frac{\sqrt{P^2 + Q^2}}{V_g} \tag{1.87}$$

and the power factor angle as

$$\varphi = \arctan\frac{Q}{P}. \tag{1.88}$$

### 1.2.3 Generator air-gap torque model

In this chapter the generator air-gap torque will be computed. The nature of the force action between the rotor and stator is in the angular misalignment between the field mmf vector $\boldsymbol{F}_f(t)$ and the armature mmf vector $\boldsymbol{F}_a(t)$. The rotor and the stator resemble two magnets whose opposite poles attract each other.

The size of the air-gap torque can be computed from the actual active power $P$ which is given by Eq. 1.86 as

$$P = 3V_g I\cos\varphi = 3EI\cos\beta\,, \tag{1.89}$$

where $\beta = \delta_{fr} + \varphi$ is called the internal power factor angle.

According to Eq. 1.69 the rms value of the emf can be computed as $E = 1/\sqrt{2}\omega N_\phi \phi_f$ and the rms value of the current as $I = 1/\sqrt{2}\, I_m$. After substitution into Eq. 1.89 we have

$$P = \frac{3}{2}\omega N_\phi \phi_f I_m \cos\beta\,. \tag{1.90}$$

From the laws of mechanics follows that the power of a force acting on an object is equal to the dot product of the vector of that force and the speed vector. An analogous law holds in case of a torque acting on a rotating object. Thanks to the colinearity of these two vectors a simple scalar equation holds

$$P_{mech} = \tau\omega. \tag{1.91}$$

In a steady state the mechanical power $P_{mech}$ must be just equal to the generator active power $P$. By comparing Eq. 1.90 and 1.91, we get the equation for the air-gap torque as

$$\tau = \frac{P}{\omega} = \frac{3}{2} N_{\phi} \phi_f I_m \cos\beta\,. \tag{1.92}$$

By the interpretation of Eq. 1.92 it is necessary to keep in mind the mutual interconnection of the acting measures. Its validity must be understood only for a small neighbourhood of the actual generator operating point. For example, according to the equation there is proportionality between the amplitude of the field magnetic flux and the amplitude of the air-gap torque. In practice, however, an increase in excitation (i.e. field current) moves the armature current phasor $I_m$ and, eventually, increases the internal power factor angle $\beta$. However, the Eq. 1.92 will advantageously be used in Chapter 2 in the discussion about rotor torsional vibration as a consequence of transient events in the power grid.

# 2 Interaction of a turbine-generator with the electrical grid

In this chapter the most significant phenomena capable of torsional vibration excitation will be addressed. In general, they all are present continually. Their intensity, however, is usually below safety limits and the corresponding material stress is below endurance limit. However, isolated events of powerful torsional excitation followed by a considerable torsional vibration may occur. At these moments, fatigue life is exploited or other permanent material damage may occur.

## 2.1 Transient events in the electrical grid

In this chapter the effect of transient events in the power grid on the turbine-generator rotor will be analysed. Relevant transient events involve power grid configuration changes, lightning strikes to electrical facility, short-circuits, stepwise load changes, etc. In addition, non-ideal synchronization can also by a source of major torsional excitation.
First, the case of a step change of the terminal voltage phase will be analysed, i.e. the angle of the phasor $\underline{V_g}$. The emf phasor $\underline{E}$ is considered to be unchanged as it is fixed to the rotor inertia and the field current which is supposed to be constant. As a consequence, the torque angle $\delta_{fr}$ and the amplitude and angle of the current phasor $\underline{I}$ are subject to the step change so that the equation $\underline{V_g} = \underline{E} - jX_a\underline{I}$ still holds. The situation is illustrated by the Fig. 2.1.

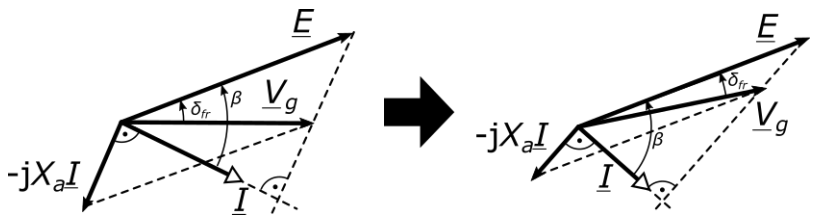


***Fig. 2.1 Terminal voltage phasor $\underline{V_g}$.angle change.***

It can be seen from Fig. 2.1 that the armature reaction phasor $-jX_a\underline{I}$ amplitude is larger. This can be achieved only by the increase of the current phasor $\underline{I}$. From the geometry of the situation follows that, in turn, the angle $\beta$ between the phasors $\underline{I}$ and $\underline{E}$ increses. Thanks to the increase of $\underline{I}$ and the simultaneous decrease of $\beta$, the projection $I\cos\beta$ of the phasor $\underline{I}$ into the direction of $\underline{E}$ increses.
As a consequence, the amplitude of the air-gap torque $\tau$ increases according to Eq. 1.92 (the number of turns $N_\phi$ is constant and the magnetic flux $\phi_f$ is dictated by the field current and thus constant as well). This breaks the balance between the power provided by the turbine and the generator active power. The machine starts to deccelerate. This decceleration also means the diminishing of the torque angle $\delta_{fr}$. After certain time the twist angle returns to the value equal to that before the voltage phasor change. In this state, the balance between the turbine power and the generator active power is re-established again. However, the rotor has a lower velocity than the grid frequency. Due to its inertia the rotor starts to delay the grid and the twist angle is increasing $\delta_{fr}$. Hence, the rotor is subject to an accelerating torque that is willing to bring the rotor back to equilibrium state. To summarize, the rotor is oscillating around its equilibrium state. This oscillation gradually diminishes thanks to energy loss on both the mechanic and electrict side of the system.

In the following we determine a relation which will be used in one of the case studies in Chapter 4. Let's consider the following situation. First, the generator is operating at a steady state described by $P_1$, $Q_1$, $V_g$ and $E$. This implies a power factor angle $\varphi_1$ and a load angle $\delta_1$. Then, a sudden increase in the load

angle happens due to a sudden rotation of the phasor of the terminal voltage $V_g$. Such a situation can occur, for example, due to a sudden change in network impedance due to a certain operational intervention. Let the magnitude of the terminal voltage phasor remain the same. Since the event occurs suddenly, the phasor of the electromotive force can also be considered fixed during the event. Thus, just after the event the generator operates at a different state described by new power quantities $P_2$, $Q_2$, the amplitudes of the voltage quantities remain the same $V_g$ and $E$ but there are new values of the power factor angle $\varphi_2$ and the load angle $\delta_2$.
For the analysis later in Chapter 4, we determine the equation for the ratio of $P_2/P_1$. From the phasor diagram it can be seen that

$$\sin\varphi \cdot X_d I = \cos\delta_{fr} \cdot E, \tag{2.1}$$

This implies that during the conditions of the previous paragraph, we get

$$\frac{I_2}{I_1} = \frac{\dfrac{\sin\delta_2 \cdot E}{\cos\varphi_2 \cdot X_d}}{\dfrac{\sin\delta_1 \cdot E}{\cos\varphi_1 \cdot X_d}} = \frac{\sin\delta_2 \cdot \cos\varphi_1}{\sin\delta_1 \cdot \cos\varphi_2}. \tag{2.2}$$

If we computed the ratio $P_2/P_1$ by substituting into Eq. 2.2, we get the following expression

$$\frac{P_2}{P_1} = \frac{\sin\delta_2}{\sin\delta_1}. \tag{2.3}$$

Recall this equation is not of general validity but its validity is limited to the conditions given above. However, in one of the case studies in Chapter 4 it helps us to determine the change of the load angle during an event.

## 2.2 Unbalanced power grid

The term grid unbalance describes a state when the voltage phasors of individual phases differ in amplitude or if they have a different angle than 120°. This situation can be the result of short-circuits, unbalanced load or absence of transmission line transposition.
First, the grid unbalance caused by unequal voltage amplitudes on three phases will be analysed. Specifically, let the phase A be subject to a voltage drop to 50 % of the original value. The Fig. 2.2 shows the time trends of voltage at the three phases in a time interval slightly greater than one period.

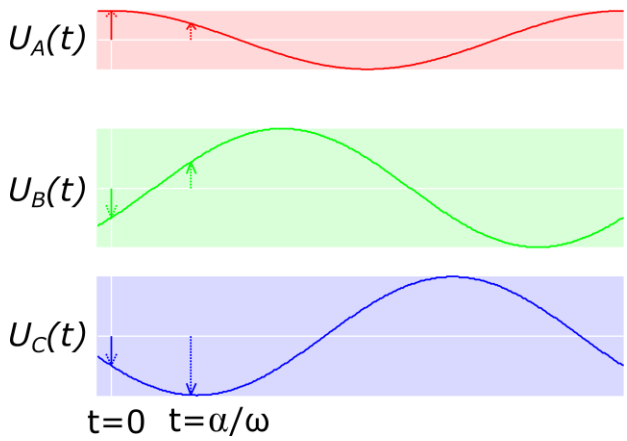


*Fig. 2.2 Time trend of unbalanced voltage – 50 % drop of voltage amplitude at phase A*

Figure 2.2 shows the resultant armature mmf vecor $\boldsymbol{F}_a(t)$ and its three phase components for two different time instances $t = 0$ and $t = \alpha/\omega$. It can be seen that the vector $\boldsymbol{F}_a(t)$ does not proceed in a circle any more but rather in an elipse. This means that the amplitude of $\boldsymbol{F}_a(t)$ decreases twice and

increases twice within one rotation and so does the resultant mmf. As a consequence the air-gap torque exhibits the same fluctuation leading to a torsional vibration excitation at twice the grid frequency. If the grid frequency is 50 Hz the torsional vibration excitation frequency caused by grid unbalance is 100 Hz.

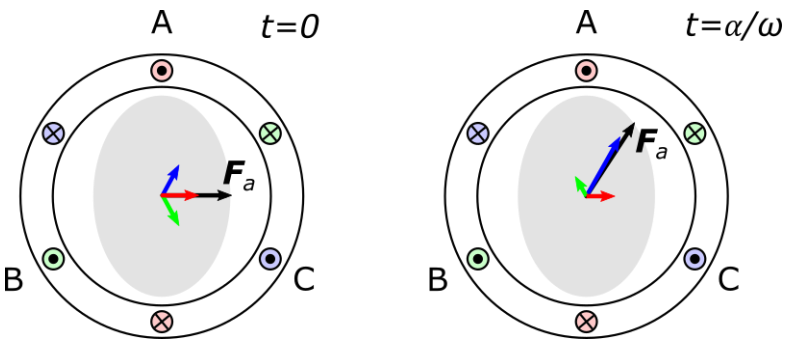


*Fig. 2.3 Armature mmf during grid unbalance – 50 % drop of voltage amplitude at phase A.*

Second, another type of grid unbalance will be analysed, namely the case of phasors distributed other than 120° from each other. In concrete, let the phase A phasor $U_A$ be delayed by 30°. Figure 2.4 shows the time trends of voltage at all three phases in a time interval slightly greater than one period.

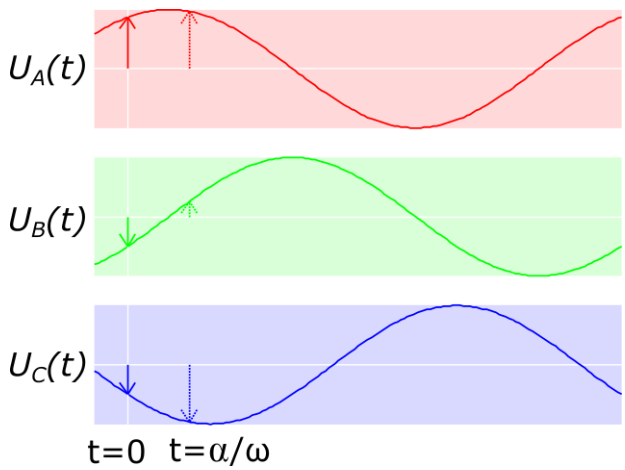


*Fig. 2.4 Time course of the voltage on the three phases in case of unbalance - phase A has a phase delay of 30°.*

Again, Fig. 2.5 shows the resultant armature mmf vecor $\boldsymbol{F}_a(t)$ and its three phase components for two different time instances $t = 0$ and $t = \alpha/\omega$. It can be seen that the vector $\boldsymbol{F}_a(t)$ does not proceed in a circle any more but in an elipse. From the same reason as in case of amplitude unbalance the rotor will be subject to torsional vibration excitation at twice the grid frequency.

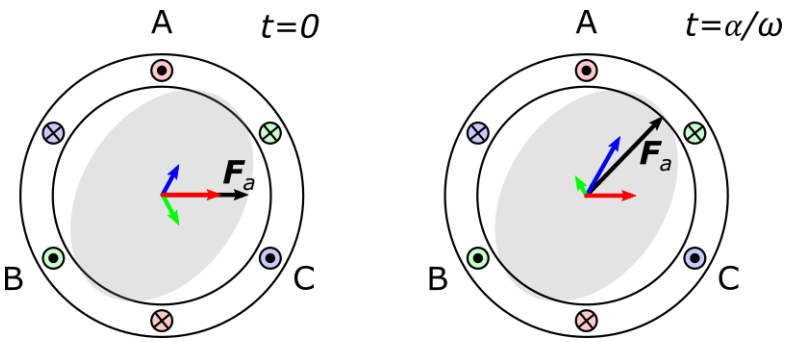


*Fig. 2.5 Armature mmf during grid unbalance – 30° delay of the voltage phasor at phase A.*

Grid unbalance can be interpreted by means of two sets of symmetrical components rotating in opposite direction and an additional direct component. These are known as positive, negative and zero components. The negative component is rotating in the opposite direction to the positive component and thus they build together twice per rotation. Hence, the resultant vector is subject to an oscillation at twice the grid frequency.

Figure 2.6 illustrates the break-up into symmetrical components. An arbitrary non-symmetrical set of phasors $\underline{U}_A$, $\underline{U}_B$ and $\underline{U}_C$ is transformed into three symmetrical components: the positive sequence $\underline{U}_{AP}$, $\underline{U}_{BP}$ and $\underline{U}_{CP}$, the negative sequence $\underline{U}_{AN}$, $\underline{U}_{BN}$ and $\underline{U}_{CN}$ and zero sequence which are put into a single phasor $\underline{U}_0$.

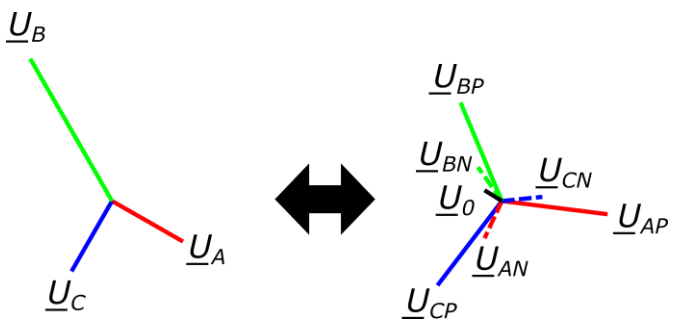


*Fig. 2.6 Transformation of an unbalanced set of voltages into symmetrical components.*

A positive sequence voltage put to armature windings creates a magnetic field $\boldsymbol{F}_{aP}$ rotating in the same direction as the resultant vecor of the original unbalanced voltages $\boldsymbol{F}_a$. That is why it is called positive. On the contrary, a negative sequence voltage put to armature windings creates a magnetic field $\boldsymbol{F}_{aN}$ rotating in the opposite direction relative to the resultant vecor of the original unbalanced voltages $\boldsymbol{F}_a$. This is why it is called a negative sequence. The two vectors $\boldsymbol{F}_{aP}$ and $\boldsymbol{F}_{aN}$ coincide twice per revolution, thus the resultant vector $\boldsymbol{F}_a$ moves along an elipse, similar to that shown in Fig. 2.3 and 2.5. This, as a consequence, creates air-gap torque spikes at twice the grid frequency.

## 2.3 Subsynchronous resonance

Subsynchronous resonance (SSR) is a term reffereing to an oscillation within the electro-mechanical system. Subsynchronous resonance can exist only if the electrical grid resonance frequency meets one of the rotor torsional natural frequencies. Electrical grids with long series-compensated lines are prone to SSR at most. This is because the series compensation brings a capacitive impedance to a system (transmission line) which has a dominant inductive impedance by nature. Thus, a full RLC circuit is created which has it's own natural frequency of oscillation. The natural (resonant) frequency is given by a simplified equation

$$f_{res} = \frac{1}{\sqrt{LC}}, \tag{2.4}$$

where $L$ is the series inductance and $C$ is the series capacitance of the transmission line. Practically, the resonance frequency $f_{res}$ is lower than the mains frequency, thus the term *subsynchronous* resonance. Subsynchronous currents enter the generator armature winding and induce an additional magnetic field. By the superposition with the synchronous rotatory magnetic field beats are produced. The frequency of the beats is $f_{SSR}$ which is equal to the subtraction of the synchronous and subsynchronous frequency

$$f_{SSR} = 50 - f_{rez}, \tag{2.5}$$

In case the frequency $f_{SSR}$ gets close to one of the torsional natural frequencies of the rotor, torsional vibration at this frequency is steadily excited. Thanks to the relatively low modal damping of the torsional vibration the resultant amplitude can be high enough to cause fatigue damage.
Kilgore et al. [14] present a detailed analysis of the autooscillations caused by the subsynchronous resonance. First, the authors present the relation between the mechanical oscillation f the generator rotor and the existence of two positive sequence components of voltage and current in the electrical grid at the frequencies of $\omega_{rot} - \omega_m$ a $\omega_{rot} + \omega_m$. This relation is obtained as follows.
Let the rotor be subject to a steady rotary motion with the velocity of $\omega_0$ and, in addition, to oscillations at the frequency $\omega_m$ and amplitude $A$

$$\omega(t) = \omega_{rot} + A\cos(\omega_m t)\,. \tag{2.6}$$

Under this condition the rotor angular position is given by

$$\varphi(t) = \omega_{rot} t + \frac{A}{\omega_m}\sin(\omega_m t)\,. \tag{2.7}$$

Now it will be shown that the magnetic field of the generator rotor whose motion is defined by Eq. 2.6 induces in the stator a couple of alternating emfs at frequencies $\omega_{rot} - \omega_m$ a $\omega_{rot} + \omega_m$. According to Eq. 1.80 the armature flux linkage is dependent on the cosine of the rotor angle

$$\psi(t) = k\cos\big(\varphi(t)\big)\,, \tag{2.8}$$

where $k = L_a I_m$. The corresponding induced emf is given by the time derivation of Eq. 2.8 as

$$e(t) = -\frac{\mathrm{d}\psi(t)}{\mathrm{d}t} = k\sin\big(\varphi(t)\big)\frac{\mathrm{d}\varphi(t)}{\mathrm{d}t} = k\sin\big(\varphi(t)\big)\,\omega(t). \tag{2.9}$$

By the substitution for $\varphi(t)$ and $\omega(t)$ according to Eq. 2.7 and Eq. 2.9 we obtain

$$e(t) = k\sin\left(\omega_{rot} t + \frac{A}{\omega_m}\sin(\omega_m t)\right)(\omega_{rot} + A\cos(\omega_m t)). \tag{2.10}$$

Rewriting the sine and cosine function by complex exponential functions using Euler's formula the Eq. 2.10 can be written as

$$e(t) = \frac{k}{2i}\left(e^{i\left(\omega_{rot}t + \frac{A}{\omega_m}\sin(\omega_m t)\right)} - e^{-i\left(\omega_{rot}t + \frac{A}{\omega_m}\sin(\omega_m t)\right)}\right)\left(\omega_{rot} + \frac{A}{2}\left(e^{i\omega_m t} + e^{-i\omega_m t}\right)\right). \tag{2.11}$$

By multiplying the large parenthesis in Eq. 2.11 we get

$$\begin{aligned} e(t) = {} & \frac{k\omega_{rot}}{2i}e^{i\left(\omega_{rot}t + \frac{A}{\omega_m}\sin(\omega_m t)\right)} - \frac{k\omega_{ot}}{2i}e^{-i\left(\omega_{rot}t + \frac{A}{\omega_m}\sin(\omega_m t)\right)} + \\ & \frac{kA}{4i}e^{i\left(\omega_{rot}t + \frac{A}{\omega_m}\sin(\omega_m t) + \omega_m t\right)} - \frac{kA}{4i}e^{-i\left(\omega_{rot}t + \frac{A}{\omega_m}\sin(\omega_m t) - \omega_m t\right)} + \\ & \frac{kA}{4i}e^{i\left(\omega_{rot}t + \frac{A}{\omega_m}\sin(\omega_m t) - \omega_m t\right)} - \frac{kA}{4i}e^{-i\left(\omega_{rot}t + \frac{A}{\omega_m}\sin(\omega_m t) + \omega_m t\right)}. \end{aligned} \tag{2.12}$$

An appropriate rearrangement of the members in Eq. 2.12 and the conversion of the complex functions back to trigonometric functions the Eq. 2.12 can be simplified to

$$e(t) = k\omega_{rot}\sin\left(\omega_{rot}t + \frac{A}{\omega_m}\sin(\omega_m t)\right) + \frac{kA}{2}\sin\left((\omega_{rot} - \omega_m)t + \frac{A}{\omega_m}\sin(\omega_m t)\right)$$
$$+\frac{kA}{2}\sin\left((\omega_{rot} + \omega_m)t + \frac{A}{\omega_m}\sin(\omega_m t)\right). \tag{2.13}$$

Note the term $A/\omega_m$ inside the parenthesis – it is very small as the amplitude of the torsional vibration is very small compared to the frequency of the mechanical oscillation. Under the condition of small oscillation Eq. 2.13 can be simplified to

$$e(t) = k\left[\omega_{rot}\sin(\omega_0 t) + \frac{A}{2}\sin\big((\omega_{rot} - \omega_m)t\big) + \frac{A}{2}\sin\big((\omega_{rot} + \omega_m)t\big)\right]. \tag{2.14}$$

It is therefore clear that mechanical oscillation at the frequency of $\omega_m$ induces currents at the frequencies of $\omega_{rot} - \omega_m$ and $\omega_{rot} + \omega_m$ in the armature winding.

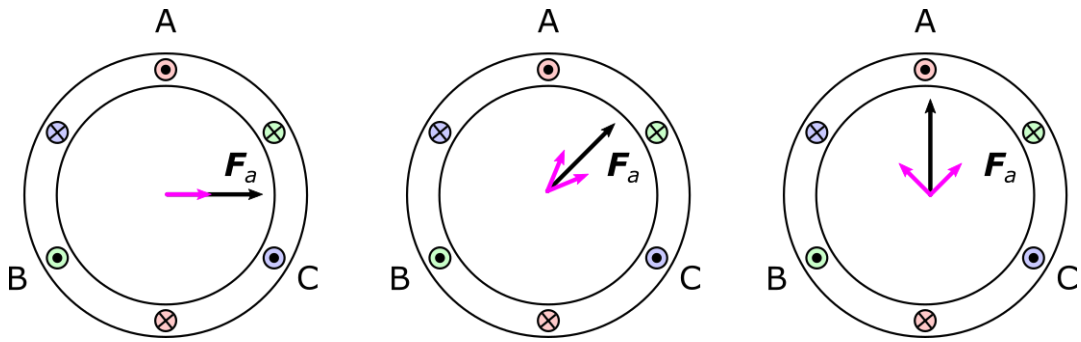


*Fig. 2.7 Armature mmf (black) and the induced mmfs caused by SSR (magenta).*

# 3 Torsional vibration analysis based on incremental encoder data

In the previous chapters the problem of turbine-generator rotor torsional vibration has been discussed in the perspective of vibration mechanics as well as the underlying electro-mechanical processes inside the generator. It was explained that their understanding is crucial when building the overall picture of the torsional vibration.
This chapter, which can be seen as the core of this thesis, is devoted to the development of a system providing information about turbine-generator rotor vibration. In the very beginning, the reader is kindly asked to consider following facts which demonstrate the complexity of the problem and justify the extent of research and development being presented.
In operation, the generator rotor is rotating at $3000\,rpm$ which is $314\,rad \cdot s^{-1}$. A level of torsional vibration of a 380 MW unit which is considered to be dangerous is about $0{,}004\,rad \cdot s^{-1}$. Comparing these two numbers it gets obvious that the torsional vibration causes only a *fluctuation* of the angular speed by the order of 0,001 % (!). It is right this small amplitude which makes torsional vibration undetectable with conventional measurement devices. Instead, a specialized monitoring system and data analysis has to be developed.

As already written, this chapter is devoted to the design of a torsional vibration monitoring system. As a first step, requirements on such a system have been defined:

- The system must be able to provide up-to-date information on torsional vibration
- This information must be available within a maximum predefined delay, e.g. 2 seconds
- The error of the result must be kept below a predefined limit
- The inputs of the system are time increments measured on the incremental encoder together with the encoder geometry

From the first two requirements, there is a need to structure the system as a real-time system. In this case, the data does not have the same weight in time. Their weight decreases from the newest data to oldest data. From this it is clear that some recursive algorithm will have to be implemented in the system. In other words, the system will certainly not provide some sort of offline analysis in historical data where the entire time horizon of the measurement would be available. Such an analysis would require different methods.
The condition that the result error must be kept below a certain limit is natural with regard to the intended integration of the system into a wider turbine-generator protection system. In this case, the accuracy of the results needs to be at least in order of magnitude comparable to the alarm values of the turbine-generator protection system.
According to the fourth requirement, time increments measured by an incremental encoder are the system input. In this context, it must be said that no prefabricated incremental encoder is used in this work. This would be difficult to install in a turbine-generator rotor environment. Instead, a self-design solution is used, consisting of an encoder tape glued to the circumference of the rotor.
The chapter starts with an introduction including the definition of the system structure and its inputs and outputs. Then we develop a method for precise encoder geometry estimation. Afterwards we present methods for instantaneous angular speed evaluation. And the last two sections are focused on error evaluation and the explanation of a structural limitation of the proposed method.

## 3.1 System structure and input data

It is reasonable to start the chapter with the overall system description where individual components and their purpose will be presented. Also the characteristics of the measured signals will be discussed as these are the input information for the subsequent torsional vibration analysis.
Figure 3.1 shows the structure of the measurement system. On the left-hand side there is the turbine rotor presenting the mechanical part which is subject to the torsional vibration to be analysed. On the

rotor circumference a kind of zebra tape is attached. The zebra tape consists of a repeating pattern of black and white stripes. A sensor attached to the stator part of the machine is able to distinguish between these two levels by means of a rectangular signal on its output. The principle of the zebra-tape measurement can be optical or elecro-magnetic as discussed in Appendix 6.1 in more detail.
The rectangular signal is then fed to a high precision A/D converter with an electronic preprocessor which is able to determine the *time increments*, i.e. the time differences between two consecutive rising edges in the rectangular signal. The time increments are the input information to the torsional vibration analysis implemented in the torsional vibration monitoring system.
The time increments are used to compute the turbine instantaneous angular speed. Recall that torsional vibration causes a fluctuation of the angular speed. Therefore, it is possible to evaluate torsional vibration based on the knowledge of the angular speed. The reason, why we sometimes use the adjective *instantaneous*, is to highlight the fact that not the standardly monitored turbine rotational speed but only a precise angular speed can be used for torsional vibration evaluation. The computed angular speed will always be given for a given measurement plane. The measurement plane is defined by the rotor cross section whose axial location is given by the sensor.
The angular speed is, like any other velocity, rate of change of position with respect to time. In our case it will be computed based on the measured time increments and the known encoder geometry. In order to calculate the speed accurately, both of these quantities must also be known accurately. This means that not only the measurement of the time increments must be precise but also that the encoder geometry must be known accurately. As will later be shown, the encoder stripes can not be considered equidistant but their individual widths must also be evaluated. Hence, encoder geometry is one of the sought-after quantities.
For the end user which is supposed to be a power plant operation engineer the most important information is whether torsional vibration is within limits or if the limits were exceeded. Hence, the major outputs of the system are the torsional vibration amplitudes and frequencies.

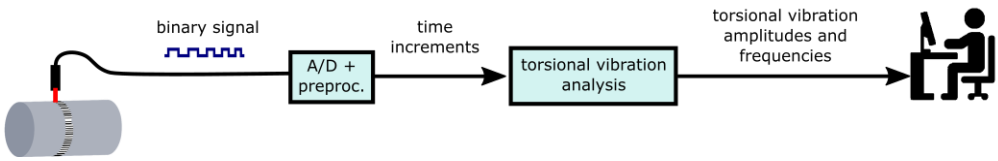


*Fig. 3.1 The torsional vibration monitoring system.*

To illustrate how the presence of torsional vibration manifests itself in the output signal, let us have a look at Fig. 3.2. The left-hand part shows the situation of no torsional vibration. It can be seen that the output signal (blue line) forms a periodic rectangular function. On the contrary, in case of torsional vibration, a phase modulation of the rectangular function can be seen. The phase modulation contains the torsional vibration information.

*Fig. 3.2 Rectangular signal in case of zero (left) and nonzero (right) torsional vibration.*

Let us introduce important parameters and measures which will be used throughout the work. In Fig. 3.3, we see a zebra tape and a sensor which is able to detect the rising edges in the signal. A rising edge is generated at each transition from a black area to a white area. As a result we obtain the same number of rising edges over a single revolution as is the number of white (or black) areas. That is why we introduce a general term *stripe* which refers to every white-black couple. As a result the number of stripes is equal to the number of white (or black) areas. The number of stripes is denoted as $N$.
Next, we define the angular width of a stripe as $\phi$ $[rad]$. Obviously, the sum of all angular widths gives $2\pi$ because the zebra tape goes around the whole circumference

$$\sum_{n=1}^{N} \phi_n = 2\pi. \tag{3.1}$$

The time during which the rotor rotates by a single stripe is denoted by $t$. The meaning of the measures $\phi$ and $t$ should be clear from the highlighted lines of magenta color.

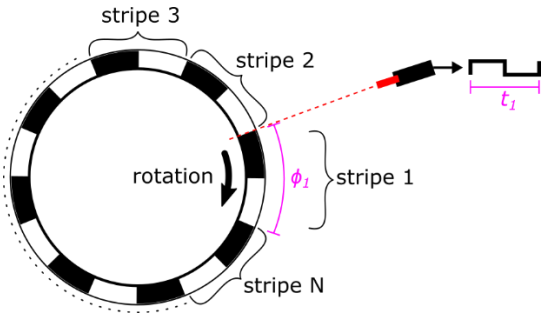


***Fig. 3.3 Zebra tape and introduction of important measures.***

Because most of the later derived methods will make use of continuous data, we introduce a continuous index $i$. From the sensor's point of view, one particular zebra tape stripe comes every $N$ stripes, i.e. indices $i$, $i+N$, $i+2N$ all refer to the same stripe. It should be clear that the sum of $N$ consecutive stripes always gives $2\pi$ no matter what is the starting index $i$ because $N$ consecutive stripes always build the whole circumference. A similar principle holds also for the time increments. Both principles are described by the following equations

$$\phi_i + \phi_{i-1} + \ldots + \phi_{i-N+1} = 2\pi \tag{3.2}$$

$$t_i + t_{i-1} + \ldots + t_{i-N+1} = T_i \tag{3.3}$$

## 3.2 Encoder geometry and a method of its estimation

This chapter presents a self-design solution for encoder geometry computation based on the measured time increments. Under the term encoder geometry we will understand a set of $N$ angular distances between $N$ consecutive encoder stripes, formally written as

$$\phi_i, \phi_{i+1}, \ldots, \phi_{i+N}. \tag{3.4}$$

As a sidenote please note, that for the term *distance between adjacent stripes*, the term *gap width* is also used in the text.

Chapter 3.2.1 presents one of the proposed methods of calculating the encoder geometry from the measured time increments. This method would give accurate results assuming a constant encoder geometry. However, in the beginning of Chapter 3.3.2 we will explain that this assumption is not fulfilled in practice and the method of determining the encoder geometry must therefore be extended to give usable results even in the case of changing encoder geometry. The result will be a system for estimating the geometry of the encoder which will be the subject of Chapter 3.3.2.

### 3.2.1 Algorithm for calculating the gap width from measured time increments

The problem to be solved in this chapter is defined as follows. We assume an encoder with $N$ stripes. The goal is to calculate $N$ angular distances, gap widths, formally written as

$$\phi_i, \quad i = 1, \ldots, N \quad [rad]. \tag{3.5}$$

In an idealized case without any disturbances, the width ratio of two adjacent gaps would be very well approximated by the time increment ratio corresponding to these two gaps, as the effect of speed change as well as the effect of torsional vibrations on the range of these two gaps would be negligible. In

addition, this ratio for a given pair of adjacent gaps does not depend on the machine speed and therefore does not need to be additionally compensated.

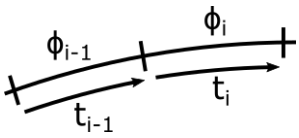


*Fig. 3.4 The meaning of the quantities t (time increment) and ϕ (gap width).*

Let us denote the ratio by the letter $r$ and define it by the equation

$$r_i \triangleq \frac{t_{i-1}}{t_i} \equiv \frac{\phi_{i-1}}{\phi_i} \quad [-]. \tag{3.6}$$

The measure $r_i$ can be evaluated in every iteration $i$ and a history of the last $N-1$ values can be kept in memory

$$r_i,\ r_{i-1},\ \dots\ ,\ r_{i-N+2} \tag{3.7}$$

In view of the above, the following equations must hold

$$r_i = \frac{\phi_{i-1}}{\phi_i},\ \ r_{i-1} = \frac{\phi_{i-2}}{\phi_{i-1}},\ \ \dots\ ,\ \ r_{i-N+2} = \frac{\phi_{i-N+1}}{\phi_{i-N+2}}. \tag{3.8}$$

Equations 3.8 can be seen as a system of $N-1$ linear equations of $N$ unknowns.

However, there is an additional condition for gap widths $\phi_i, \phi_{i-1}, \dots, \phi_{i-N+1}$, that their sum is equal to $2\pi$, because they just fill the whole circumference. Recall that we assume a tape with $N$ stripes. So it is possible to write

$$\phi_i + \phi_{i-1} + \dots + \phi_{i-N+1} = 2\pi \tag{3.9}$$

Combining equations 3.8 and 3.9 we obtain a system of $N$ linearly independent equations of $N$ unknowns. Its solution leads to exactly one solution $\phi_i, \phi_{i-1}, \dots, \phi_{i-N+1}$. We solve the system by first expressing the terms in numerators from Eq. 3.8 as

$$\phi_{i-1} = \phi_i r_i,\ \ \phi_{i-2} = \phi_{i-1} r_{i-1},\ \ \dots\ ,\ \ \phi_{i-N+1} = \phi_{i-N+2} r_{i-N+2} \tag{3.10}$$

and we recursively substitute into each equation from the equations to the left so that on the right side of each equation we get the product of $\phi_i$ and the terms $r$. The resulting notation is therefore as follows

$$\phi_{i-1} = \phi_i r_i,\ \ \phi_{i-2} = \phi_i r_i r_{i-1},\ \ \dots\ ,\ \ \phi_{i-N+1} = \phi_i (r_i r_{i-1} \cdots r_{i-N+2}). \tag{3.11}$$

Now we substitute these expressions for $\phi_{i-1}, \phi_{i-2}, \dots, \phi_{i-N+1}$ into Eq. 3.9, which yields

$$\phi_i + \phi_i r_i + \phi_i r_i r_{i-1} + \dots + \phi_i (r_i r_{i-1} \cdots r_{i-N+2}) = 2\pi. \tag{3.12}$$

By sticking the term $\phi_i$ on the left side of the equation and converting the remaining expression to the right side, we get

$$\phi_i = \frac{2\pi}{1 + (r_i) + (r_i r_{i-1}) + \cdots + (r_i r_{i-1} \cdots r_{i-N+2})} \tag{3.13}$$

Equation 3.13 gets even simpler if we substitute the terms $r$ by the time increments ratios according to Equation 3.8. By making this adjustment and a small rearrangement of the fraction, we get the resulting relation

$$\phi_i = 2\pi \frac{t_i}{t_i + t_{i-1} + t_{i-2} + \cdots + t_{i-N+1}} \tag{3.14}$$

The last equation gives instructions on how to calculate the width of the $i$-th gap $\phi_i$ from the last $N$ time increments $t_i,\ t_{i-1},\ t_{i-2},\ \dots\ ,\ t_{i-N+1}$. This process can be applied in each iteration $i$ in order to always calculate the width of the most recent gap $\phi_i$. However, keep in mind, that from the nature of

the continuous indexing, gap widths $\phi_{i+k\cdot N}$ where $k \in \mathbb{Z}$ all correspond to one physical gap. So, we get the value of the gap width in every rotor revolution. It may seem like unnecessary work to count one value over and over, but as we will show in the next chapter, there are reasons why it makes sense.

### 3.2.2 Mathematical model for encoder geometry estimation

In practice, it is not possible to ensure that the gap widths, i.e. the distances between the encoder stripes in the measurement plane is constant over time. Rather, during the measurement, phenomena may occur, the effect of which cannot in principle be distinguished from a situation in which the gap widths would change.

For illustration, Fig. 3.5 shows the long term course of three selected gap widths, specifically those of indices 17, 48 and 61. Note that the size of the vertical axis interval is equal for all signals. First, it can clearly be seen that the variance of the signals is not the same. Instead, signal $\phi_{17}$ seems to have the largest variance whereas signal $\phi_{61}$ has the lowest variance. This will be an important finding for later analysis. In addition, while the gap width $\phi_{17}$ remains relatively constant over the one day period, the gap widths $\phi_{48}$ and $\phi_{61}$ are subject to a variation of the magnitude of up to 0,09 % in case of $\phi_{48}$. This proves that encoder gaps can not be considered constant in time. Finaly, between the time 21 h and 24 h a significant increase of variation can be seen in the signal $\phi_{48}$ to which we will focus our attention later as well.

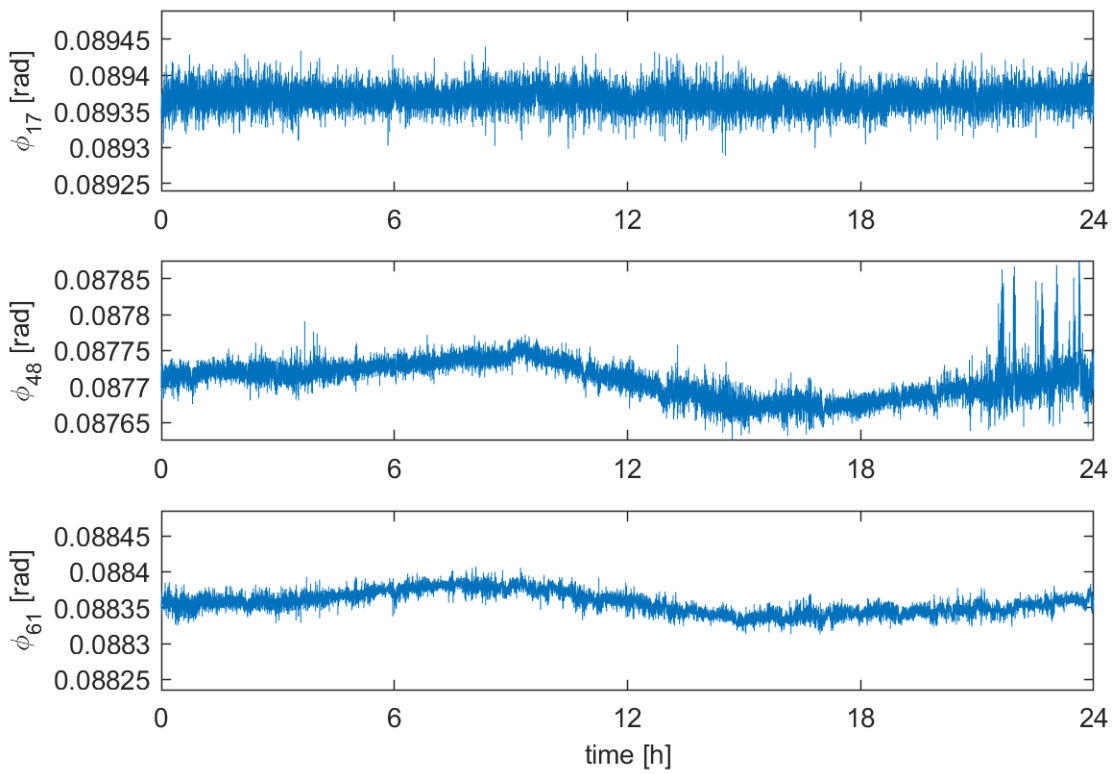


*Fig. 3.5 Long term course of three selected gap widths.*

A whole range of hypothesis can be devised to explain the fact that the gap width is not constant:

- the combination of the axial movement of the rotor and the non-parallelism of the edges of the encoder stripes causes apparent changes in the gap width
- uneven thermal deformation of the encoder tape may change the gap width
- relative movement of the stator (on which the sensor is located) relative to the rotor (to which the tape is attached) may be a cause of apparent gap width changes

- contamination of the tape, especially in the optical measuring principle, may shift the point at which the edge is detected and cause apparent changes in the gap width
- also a change in the lighting conditions in the engine room may shift the point at which the edge is detected and again cause apparent changes in the gap width

An analysis of the action mechanism of some of the above disturbances is given in Appendix 2.
From the above, it is clear that the encoder geometry can not be considered constant, but it is necessary to continually update the information during the measurement. From Fig. 3.5 we can see that the effect of encoder geometry changes on the resulting calculated instantaneous angular speed is in the order of $10^{-1}$ %. This error is not negligible in the context of the turbine-generator rotor torsional vibration analysis. Therefore, it will be necessary to design an algorithm that takes into account the variability of the encoder geometry and appropriately compensates for these changes.

From now on, we will assume that the gap width is a time-varying quantity. Gap width changes can generally occur continuously over time. From the point of view of the structure of our measurement, however, it is relevant how this quantity changes between revolutions, i.e. between the detection of one and the same gap in one revolution and the following revolution. Therefore, from now on we will investigate the discrete quantity $\phi_i(k)$ at the moments of its detection in the $k$-th revolution. The index $i$ stands for the gap position over the rotor circumference.
To allow changes in the time evolution of the quantity $\phi_i(k)$ we will formally look at the quantity $\phi_i$ as a random variable. In a general form, the time evolution of the random variable $\phi_i(k)$ can be described by the relation

$$\phi_i(k+1) = \phi_i(k) + \xi(k). \tag{3.15}$$

The quantity $\xi$ represents the change of the random variable $\phi_i$ between two consecutive revolutions. As shown in the following Chapter 3.2.3, Eq. 3.15 is a special case of a first order process that can plausibly be used to describe the gap width. The quantity $\xi$ includes all effects that affect the change of gap widths. It determines the distribution of the random variable $\phi_i$. In the beginning, we do not know the distribution of the random variable $\phi$. Depending on $\xi$, the random variable $\phi$ can have normal distribution, the nature of a Wiener process or some completely other distribution. Formally, even the case of $\xi \equiv 0$ would have been of interest as this will simply indicate that the gap widths are not changing. However, in Chapter 3.2.3 we show that a white noise is a good approximation of $\xi$.

The gap width estimation system can formally be described by the two following equations

$$\begin{aligned} \phi_i(k+1) &= \phi_i(k) + \xi_i(k) \quad [rad] \\ y_i(k) &= \phi_i(k) + \eta_i(k) \quad [rad] \end{aligned}, \tag{3.16}$$

where we forward that the quantity $y_i(k)$ is a function of time increments according to the following relation (detailed derivation can be found in Chapter 3.2.1)

$$y_i(k) \triangleq \frac{2\pi t_i(k)}{\sum_{j=i+1}^{N} t_j(k-1) + \sum_{j=1}^{i} t_j(k)} = 2\pi \frac{t_i(k)}{T}. \tag{3.17}$$

The quantity $\phi_i(k)$ expresses the true width of the $i$-th gap in the $k$-th revolution. We can therefore look at it as the state of the system, which we will try to estimate as accurately as possible. The first equation expresses the dynamics of the system, i.e. the time evolution of the gap width.
The quantity $\xi(k)$ will be called state noise and presents the gap width change between the $k$-th and $(k+1)$-th revolution. The reasons for the gap width to change have been mentioned above, such as tape contamination or axial rotor movement. Because the causes can be different and independent of each other, each can be expressed by its own quantity, leading to a more complex notation $\xi = \xi(\xi_a, \xi_b, \dots)$. However, the explicit decomposition of $\xi$ into individual components is out of the scope of this thesis.
But what we will consider is the different state noise value for different encoder stripes. Practical data show that the time change of the gap width is different for different stripes. Some stripes have more significant time change than others. Therefore, we introduce a total of $N$ generally different state noise quantities for $N$ encoder stripes denoted by the indices $i = 1, \dots, N$, written as

$$\xi_i, \;\; i = 1, \dots, N. \tag{3.18}$$

Because we have no closer information about $\xi$, we will assume it is a random variable with a normal distribution $\xi \sim N(0, \sigma_\xi)$. In fact, this assumption is only an obvious approximation. The nature of $\phi$ is not that of a Wiener process. The reasons why we still get plausible results under this assumption, is discussed in Chapter 3.2.3. The derivation of the standard deviation $\sigma_\xi$ will be the objective of Chapter 3.2.5. Here we also revise the original assumption on the normal distribution of the quantity $\xi$.

The second equation of the estimation system defined by Eq. 3.16 is the measurement equation. It gives information about the model of the measured data, i.e. what is the relationship between the state variable $\phi_i(k)$ and the measured time increments. The quantity $y(k)$ is the measured quantity that will serve as an input in each iteration. We will keep in mind that not the quantity $y$ itself is measured. Instead, the time increments $t$ are measured and these are, afterwards, used to calculate the quantity $y$ according to Eq. 3.17.
The quantity $\eta(k)$ will be called the measurement noise and it represents the uncertainty in the relation of the measured quantity $y(n)$ and the system state $\phi_i(n)$. It can be defined as a random variable with a normal distribution $\eta \sim N(0, \sigma_\eta)$.

Assuming that the measured time increments $t$ are subject to a normal distribution error with a standard deviation $\sigma_t$, the derived quantity $y$ is also subject to a normal distribution error with a standard deviation $\sigma_\phi$ according to the error transmission rules, where

$$\sigma_y = \frac{2\pi}{T} \cdot \sigma_t \tag{3.19}$$

In Eq. 3.19 we consider the error of the determination of the measure $T$ small compared to that of the quantity $t$. Thus, the measure $T$ can present a constant value in Eq. 3.19.

### 3.2.3 Identification of the parameters of the model of the quantity gap width

In this chapter we look into detail at the state equation of the model given by Eq. 3.16, i.e. the time evolution of the gap width. To simplify the notation we omit the index $i$ knowing that our discussion is appliable for all encoder stripes $i = 1, \dots, N$. The equation 3.16 is a special case of a more general linear process given by

$$\phi(k) = a_1 \cdot \phi(k-1) + a_2 \cdot \phi(k-2) + \cdots + a_n \cdot \phi(k-n) \tag{3.20}$$

which respects a natural expectation of some sort of causal dependence of consecutive samples. We will investigate the simplest variant of this dependence for $n = 1$, in which we will determine only one single parameter $a$, i.e.

$$\phi(k) = a \cdot \phi(k-1). \tag{3.21}$$

Now we can define a new variable $\Delta\phi(k) \triangleq \phi(k) - \phi_0$ which will represent the deviation of the gap width from the idealized value $\phi_0$, i.e.

$$\Delta\phi(k) = \phi(k) - \phi_0. \tag{3.22}$$

where the value of $\phi_0 = 2\pi/N$ represents the gap width of an idealized encoder with $N$ equidistant markers.

$$\Delta\phi(k) = a \cdot \Delta\phi(k-1). \tag{3.23}$$

It can not be expected that this equation will accurately represent the actual situation. For that reason, we will also introduce an error quantity $\epsilon$, which will express the error of the model. The resulting relation including the error quantity $\epsilon$ therefore has the form

$$\Delta\phi(k) = a \cdot \Delta\phi(k-1) + \epsilon(k). \tag{3.24}$$

We can write Eq. 3.24 for a set of $l$ values $\Delta\phi(k)$, ..., $\Delta\phi(k+l)$. We then write the obtained set of equations in a matrix form as

$$\begin{bmatrix} \xi(k) \\ \xi(k+1) \\ \vdots \\ \xi(k+l) \end{bmatrix} = \begin{bmatrix} -\xi(k-1) \\ -\xi(k) \\ \vdots \\ -\xi(k+l-1) \end{bmatrix} a + \begin{bmatrix} \epsilon(k) \\ \epsilon(k+1) \\ \vdots \\ \epsilon(k+l) \end{bmatrix}. \tag{3.25}$$

The vectors in the equation will be denoted by Greek letters $\Theta, \Xi$, and $\varepsilon$. We thus obtain a compact notation of the equation

$$\Xi = \Theta a + \varepsilon. \tag{3.26}$$

The calculation of parameters $\alpha$ can be viewed as an optimization problem of minimizing the squares of $\epsilon$. So we can write the criterion

$$J = \varepsilon^T \varepsilon \tag{3.27}$$

By substituting from Eq. 3.26 and further modifications, it is possible to write

$$\varepsilon^T \varepsilon = (\Xi - \Theta a)^T (\Xi - \Theta a) = \Xi^{\mathrm{T}} \Xi - \Xi^{\mathrm{T}} \Theta a - a^T \Theta^{\mathrm{T}} \Xi + a^T \Theta^{\mathrm{T}} \Theta a. \tag{3.28}$$

The minimum $J$ criterion value is obtained for the optimal $a^*$ value in the minimum of the function $J(a)$, i.e. in the point where the derivation is zero. Thus, we get

$$\frac{\partial J(a)}{\partial a} = 0 \Leftrightarrow a = a^* \tag{3.29}$$

$$a^* = \left(\Theta^{\mathrm{T}} \Theta\right)^{-1} \Theta^{\mathrm{T}} \Xi \tag{3.30}$$

At this point, we have derived a procedure for calculating the parameter $a$ that minimizes the error of the model according to Eq. 3.24 in the sense of least mean squares. Now we are going to use a portion of a measured signal to evaluate the value of $a$. After doing this computation in the MATLAB environment, we get the value

$$a = 0{,}9999997 = 1 - 3 \cdot 10^{-7}. \tag{3.31}$$

As the resulting value of $a$ is a number smaller than one, the model described by Eq. 3.24 is a stable first-order process. Furthermore, as the value is close to one, we can approximate the process by a Wiener process. This lead us to the state equation in the form of a Wiener process as written in Eq. 3.21.

### 3.2.4 Determination of measurement noise $\eta$ characteristics ($\sigma_t$ and $\sigma_y$)

It can be reasonably assumed that the measurement noise $\eta$ has a zero mean value. If this were not the case, for example if the state noise of the first gap $\eta_1$ had a mean value $> 0$, then there would necessarily have to be at least one other index $i$, where the state noise $\eta_i$ would have a mean value $< 0$. This follows from the principle of the measurement, where the "end" of one time increment is also the "beginning" of the next time increment. In addition, there are no physical reasons why the measurement noise should have a non-zero mean. Even if the rising edge was detected in, say, half of the encoder stripe following the actual edge, then this would happen on all stripes, and ultimately the edge detection times would only shift by a certain offset and the measured differences and their statistical properties would remain correct.

Figure 3.6 gives a better understanding of the course of the measured signal. The essence of the signal consisting of alternating low and high voltage levels is clearly visible. The period of individual pulses is equal to the product of the rotational period of the turbine and the total number of stripes of the zebra tape. As there are 70 encoder stripes and the turbine was rotating at its nominal frequency 50 Hz, the frequency of the pulses in the measured signal is $70 \cdot 50 = 3500\ s^{-1}$. In the place marked with a red arrow, we can notice a gap that is slightly wider than the other gaps. This gap corresponds to the place where the two opposite ends of the zebra tape connect to each other. It will serve us as a reference gap for subsequent analysis.

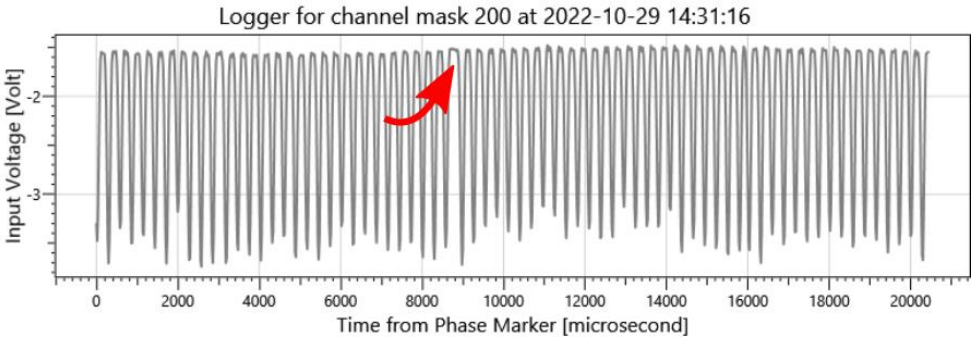


***Fig. 3.6 Time course of the measured voltage signal.***

Figure 3.7 shows a $200\ \mu s$ long portion of the measured signal in the vicinity of the rising edge of the gap being investigated. On the left the rising edge connecting the two voltage levels $-3{,}6\ V$ and $-1{,}6\ V$ can be seen. On the right a part of the high level portion of the signal can be seen. In this measurement setup, the value of $-2{,}5\ V$ was used as the threshold value indicating the time of the rising edge.

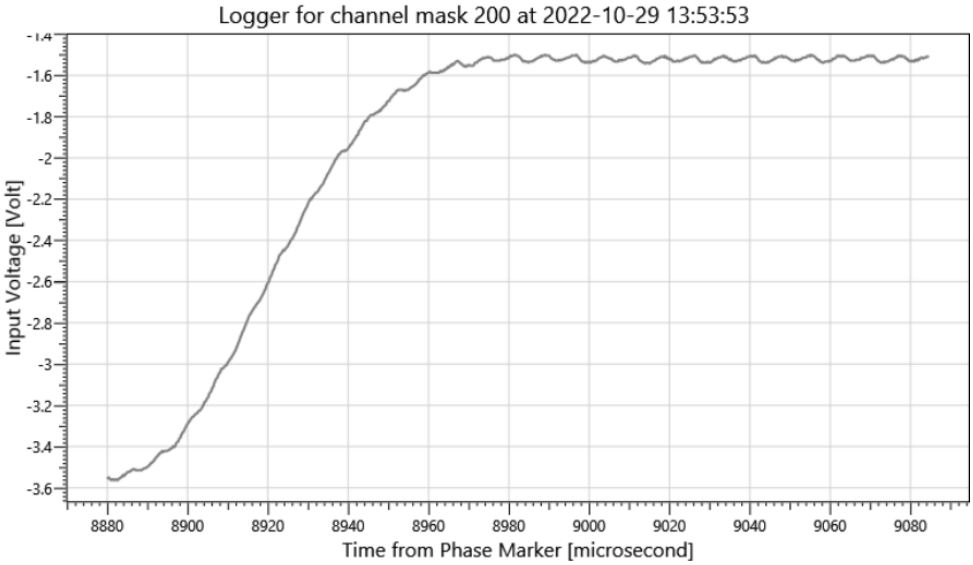


***Fig. 3.7 Time course of the measured voltage signal***

Unfortunately, measured signal was also contaminated by a harmonic noise as can also be seen in Figure 3.3. This noise is best seen in the right part of the graph where the useful signal is constant. However, the harmonic noise is present all the time, including the rising and falling edges in the signal. This harmonic noise is a source of error in the rising edge detection. The numerical expression of the error associated with it will be derived shortly.

Figure 3.8 provides even more detailed views on the signal from Figure 3.7. The upper part shows the part of the signal around the leading edge. In this graph, the slope of the leading edge at the point where the signal passes the threshold level is also indicated by the red line. This slope is closely related to the leading edge detection error, as will be shown in a moment. The lower part of the image shows a zoomed-in view of the high-level signal, which will later be used to determine the amplitude of the harmonic noise contained in the signal.

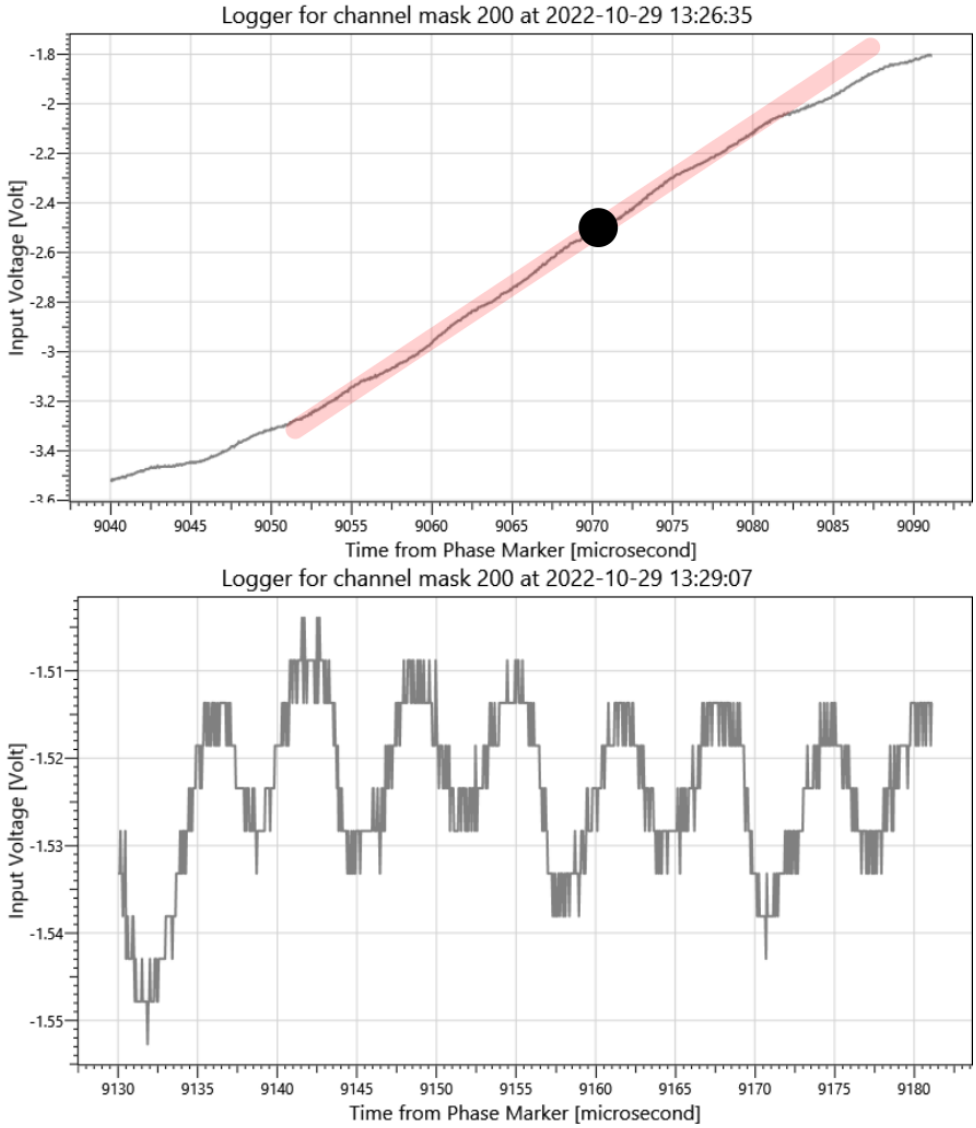


*Fig. 3.8 Time course of the measured voltage signal*

The leading edge slope is crucial for the accuracy of the leading edge time detection. The slope is shown by the red thick line in Figure 3.8. In addition, the black circle indicates the threshold level of $-2{,}5\ V$ which is used for the rising edge detection. The leading edge slope is $0{,}043\ V/\mu s$.
The quantization step of the measured signal is $0{,}005\ V$ and the amplitude of the harmonic noise is $0{,}013\ V$. Based on these values, it can be concluded that the quantization error alone would affect the detection time with the error

$$\delta_{qant} = \frac{0{,}005}{2} \cdot \frac{1}{0{,}043} = 0{,}058\ [\mu s] \tag{3.32}$$

and therefore the specified detection time is given as

$$t_{det} = t_{det} \pm 0{,}058\ \ [\mu s]. \tag{3.33}$$

Similarly, the error in detection time solely caused by harmonic noise would affect the detection time with the error

$$\delta_{harm} = 0{,}013 \cdot \frac{1}{0{,}043} = 0{,}30\ [\mu s] \tag{3.34}$$

and therefore the specified detection time is given as

$$t_{det} = t_{det} \pm 0{,}30 \ \ [\mu s]. \tag{3.35}$$

It can be noted that $\delta_{harm} \gg \delta_{kvant}$. Therefore, from now on only the quantization error $\delta_{harm}$ will be used in the calculations. For the transition from absolute error to standard deviation, the approximation from Appendix 6.4 can be used, according to which

$$\sigma_{t_{det}} \approx \frac{\sqrt{3}}{3}\delta_{harm}. \tag{3.36}$$

Furthermore, it should be considered that the standard deviation of the time increments $\sigma_t$ is equal to twice the $\sigma_{t_{det}}$, because $t$ is obtained by the difference of the detection times of the two adjacent leading edges. So it applies

$$\sigma_t \approx 2\frac{\sqrt{3}}{3}\delta_{harm} \doteq 0{,}35 \ \ [\mu s]. \tag{3.37}$$

To cross-check the results, we determine the standard deviation $\sigma_t$ calculated from the measured data. To do this, we use the signal of the time increment on the 32nd gap (i.e. the gap that has been analysed) of the encoder, which is shown in Fig. 3.9. A relatively short time of 6 $s$ is used, during which the speed can be considered constant and the fluctuations in the displayed signal can be attributed almost exclusively to the leading edge detection error.

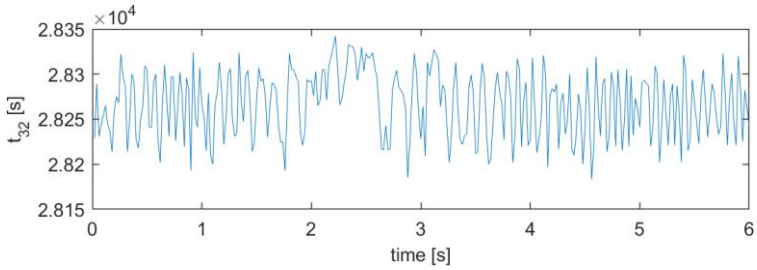


*Fig. 3.9 Time course of the time increment on the investigated gap.*

The standard deviation of the time increments calculated from the measured data is

$$\sigma_t \ = 0{,}34 \ [\mu s]. \tag{3.38}$$

It can be seen that the standard deviation calculated on the basis of the theoretical derivation from the error transmission rules from Eq. 3.17 and the standard deviation evaluated directly from the measured signal from Eq. 3.38 come out very close to each other.

In the next part, the standard deviation $\sigma_y = \sigma_y(\sigma_t)$ of the quantity $y$ according to Eq. 3.17 will be determined similarly. This standard deviation will then be identified with the standard deviation of the measurement noise $\sigma_y \equiv \sigma_\eta$.
Substituting for $\sigma_t$ from equation 3.25 to equation 3.19 we obtain

$$\sigma_y = 2\pi \cdot 0{,}35 \cdot 10^{-6}/0{,}02 \doteq 110 \cdot 10^{-6} \ \ [rad]. \tag{3.39}$$

Again, to cross-check the results we determine the standard deviation $\sigma_y$ from the measured data. Figure 3.10 shows the course of the width of the first gap calculated from the measured data $t$ according to Eq. 3.17.

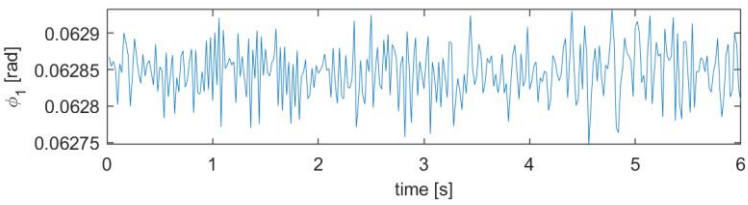


*Fig. 3.10 Time course of the width of the first gap.*

The standard deviation of the quantity $y$ calculated from the measured data is

$$\sigma_y = 115 \cdot 10^{-6}\ [rad]. \tag{3.40}$$

Again, it can be stated that the theoretically calculated value according to Eq. 3.39 is in a relatively good agreement with the value according to Equation 3.40.
From the point of view of the model described by equations 3.16, the quantity $\sigma_y$ expresses the standard deviation of the measurement noise, therefore it is possible to write

$$\sigma_\eta \equiv \sigma_y = 115 \cdot 10^{-6}\ [rad]. \tag{3.41}$$

### 3.2.5 Determination of state noise $\xi$ characteristics ($\sigma_\xi$).

In the next part we will focus on determining the state noise $\xi$. Again, it can be assumed that the state noise $\xi$ has a zero mean value. If this was not the case, e.g. on a certain index the mean value of the noise would be positive, there would have to be at least one other index on which it would be negative in order for the sum of the gaps across all indices to be equal to $2\pi$. Moreover, there are no physical reasons for the existence of a state noise value other than zero.
The standard deviation of state noise $\sigma_\xi$ is calculated using a large number of short-term non-recursive state averages, i.e. averages of the widths of a given gap. In our case, the phrase "large amount" will mean data from one whole day. The short-term averages will be calculated from measured data sections of 4 s, which is long enough to eliminate the effects of torsional vibration with frequencies in the tens of Hz and short enough to eliminate the effect of long-term turbine speed changes with frequencies in the order of small fractions of a second.
Fig. 3.11 shows such all-day trends of four second averages of the width of the 17$^{th}$ and 61$^{st}$ gap, i.e. the values of $\phi_{17}$ and $\phi_{61}$. Note the same signals have already been shown in Fig. 3.5. In addition to these signals, the adaptive mean value and the interval $\pm\sigma$ are also shown in the graphs. It can be seen that the standard deviation of the signal $\phi_{17}$ is larger than that of the signal $\phi_{61}$.

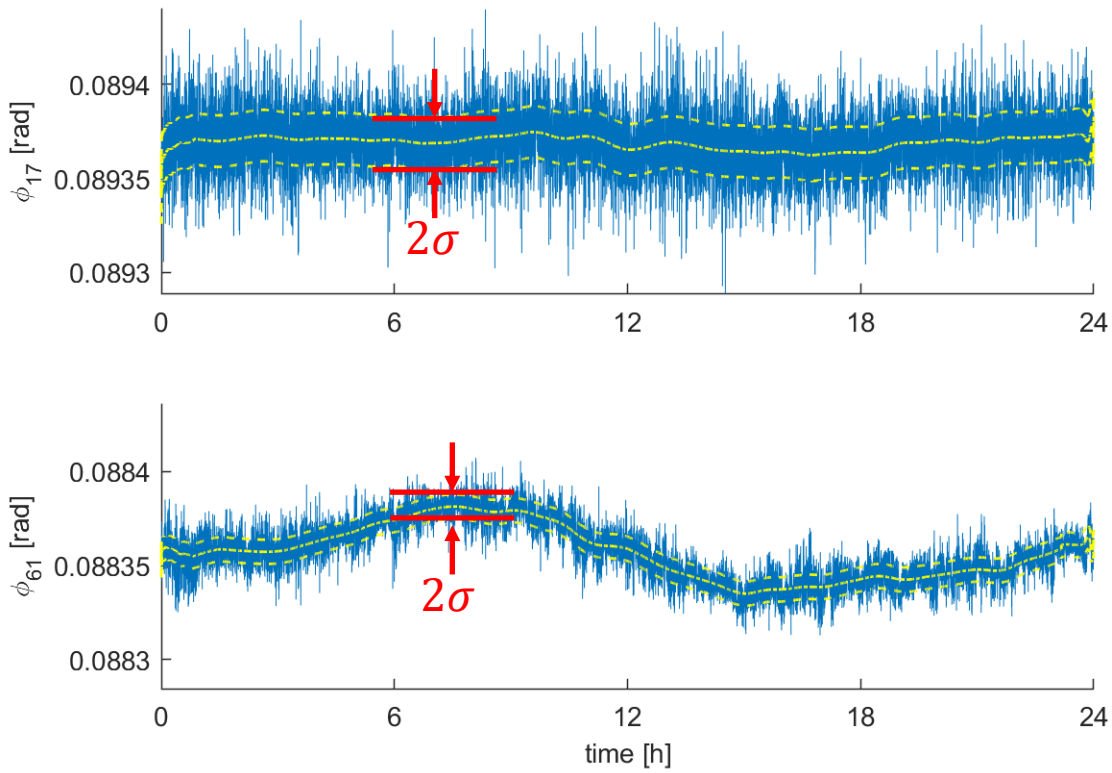


***Fig. 3.11 Long-term gap width signals with the mean value and standard deviation trends.***

To give a larger picture of the situation, Fig. 3.12 shows the mean values and especially the standard deviations for all encoder gaps as computed over the same one day. It can be seen in Fig. 3.12 that there are gaps where the state noise is stronger than elsewhere. Also, comparing the upper and lower graphs in Fig. 3.12, it can be seen that there is no relationship between the magnitude of the state noise and the size of the gap.

The only way to deal with this property is to allow different standard deviations of noise $\xi$ for different indices $i$, i.e. to introduce a set

$$\begin{gathered} \xi_1 \sim N\left(0,\ \sigma_{\xi_1}\right) \\ \xi_2 \sim N\left(0,\ \sigma_{\xi_2}\right) \\ \vdots \\ \xi_N \sim N\left(0,\ \sigma_{\xi_N}\right) \end{gathered} \tag{3.42}$$

with generally different standard deviations. This notion makes it possible to consider for each encoder gap its own standard deviation, which is denoted as $\sigma_{\xi_i}, i = 1, \dots, N$.

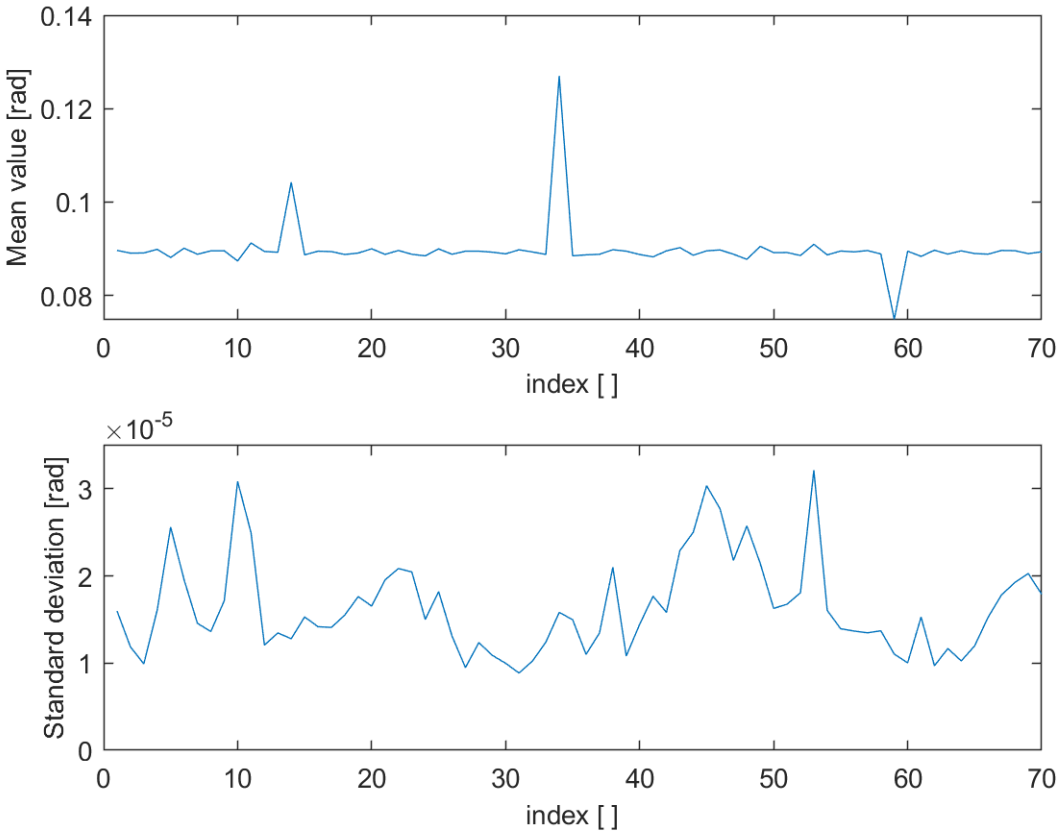


*Fig. 3.12 Characteristics of the quantity gap width*

### 3.2.6 Gap width random variable – running summary

At this point, we have designed a procedure to compute the properties of the gap width random variable $\phi$. Specifically, in section 3.2.4 we have designed a procedure to express the standard deviation of the measurement error of the time increment and in section 3.2.5 we have designed a procedure to express the standard deviation of the time change of the gap width quantity.
This gives us a complete description of the state noise $\xi$ and the measurement noise $\eta$ which appear in the equation 3.5.
For illustration, we can show a complete description of the properties of noises $\xi$ and $\eta$ for the 17th encoder gap:

$$\begin{aligned} \xi_{17} &\sim N(0,\ 16 \cdot 10^{-6}) \\ \eta_{17} &\sim N(0,\ 37 \cdot 10^{-6}) \end{aligned} \tag{3.43}$$

Having the full information of the noises $\xi$ and $\eta$ we can now focus on the development of an algorithm which will be able to compute the gap widths and cope with the problems presented in section 3.2.2. This will be the objective of the next section.

### 3.2.7 Kalman filter design for system state estimation

For the system defined by Eq. 3.16 state estimation can be performed using a Kalman filter in the form of

$$\hat{\phi}_i(k+1) = \hat{\phi}_i(k) + K_i(k) \cdot \left(y_i(k) - \phi_i(k)\right) \tag{3.44}$$

with the initial conditions

$$\sigma^2[\phi_i(0)] = P_i(0) = \infty,$$
$$E[\phi_i(0)] = \hat{\phi}_i(0) = 2\pi/N. \tag{3.45}$$

Additionally, variance $P_i(k+1)$ of the quantity $\hat{\phi}_i(n+1)$ is calculated at each step as

$$P_i(k+1) = \big(1 - K_i(k)\big) \cdot P_i(k) + \sigma_\eta^2 \tag{3.46}$$

This variance is then used to compute the Kalman gain in the following step according to the equation

$$K_i(k) = P_i(k) \cdot \big(P_i(k) + \sigma_\xi^2\big)^{-1} \tag{3.47}$$

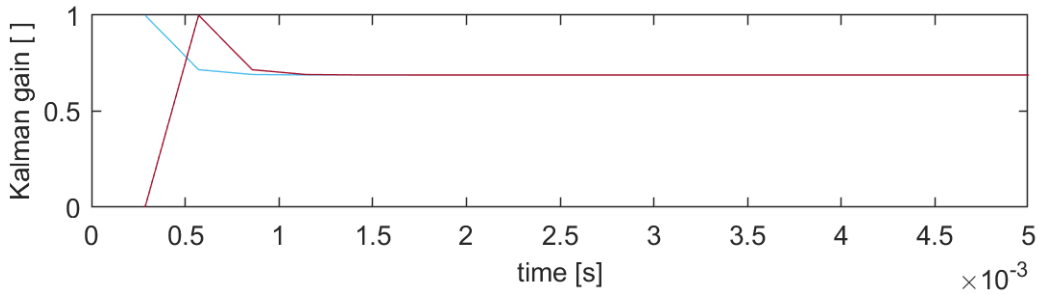


*Fig. 3.13 Kalman gain.*

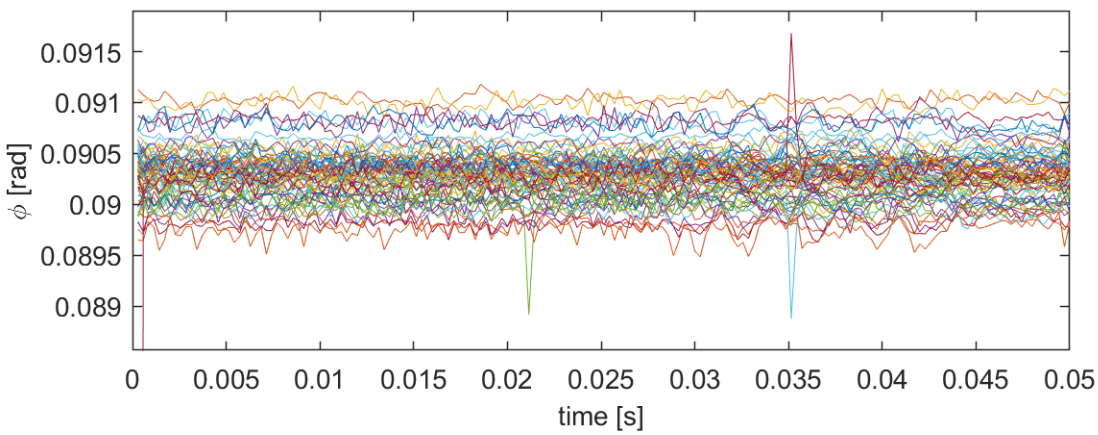


*Fig. 3.14 Kalman filtered gap widths.*

## 3.3 Instantaneous angular speed evaluation based on incremental encoder measurement

Data measured by the incremental encoder described in Chapter 3.1, i.e. the time differences between the rising edges in the output signal of the sensor, are subsequently used for rotor instantaneous angular speed computation. This quantity presents a superposition of nominal rotation of the rotor, subject to some low-frequency fluctuations, and higher-frequency components that are associated with torsional

vibration. In the frequency domain it is therefore relatively easy to separate the information about torsional vibration and get the torsional vibration velocities in $[rad/s]$. If needed, these velocities can then be integrated to get vibration angular deflection in $[rad]$.
The methods on how to calculate the instantaneous angular speed are the topic of this chapter.

### 3.3.1 Velocity computation by definition

The basic principle of the angular speed computation is relatively simple. It follows from the definition of the angular speed as a time change of the angle of rotation

$$\omega(t) = \frac{\mathrm{d}\varphi(t)}{\mathrm{d}t}. \tag{3.48}$$

If we choose a sufficiently short time interval so that the change in speed during it is negligible we can rewrite Eq. 3.48 as

$$\omega = \frac{\Delta\varphi}{\Delta t}. \tag{3.49}$$

For the nominator in Eq. 3.49 the angular distance between two consecutive encoder stripes can be substituted. It should be clear that this value equals the gap width between these two stripes and thus $\Delta\varphi = \phi_i(k)$. For the denominator the time difference between the detection times of these two consecutive rising edges in the measured signal can be substituted. This quantity equals the time increment $t$ as defined in Chapter 3.2.1. For a general situation of a rotation within the $i$-th encoder gap the following equation can be written

$$\omega_i = \frac{\phi_i(k)}{t_i(k)}. \tag{3.50}$$

Note that the form of writing in Eq. 3.50 is rather symbolic. Strictly speaking, it does not cover the case of a transition between the last mark of one revolution and the first mark of the next revolution. However, a formal notation that would apply in general would be disproportionately more complicated. Since in practice the transition between revolutions is not more complicated, we will prefer a simpler symbolic notation.

### 3.3.2 Velocity computation without encoder geometry compensation

To justify the effort devoted to calculating the exact geometry in Chapter 3.2, we will first assume a hypothetical, simplified case assuming the geometry is constant. The encoder geometry only expresses the arrangement of stripes on the encoder tape and without additional knowledge it can reasonably be assumed that the angular distance of every two consecutive stripes is $2\pi/N$ where $N$ is the total number of encoder stripes. In the following paragraphs it will be shown what consequences this assumption has and the need for a more precise algorithm will be more obvious.

Figure 3.15 shows angular speed signal computed according to Equation 3.50. The time increments that were used for the calculation were practically measured time increments on a turbine-generator. The encoder tape consists of 36 stripes and the rotational speed was at the nominal value of $3000\ RPM$, i.e. $314\ rad/s$.
It can be seen that the offset of the signal is at an expected value of $314\ rad/s$ and besides this there are some peaks of the amplitude of approximately $1\ rad/s$. Because the actual motion of the rotor is not known, it can not be distinguished whether these peaks are caused by a noise or whether they correspond to the actual motion of the rotor. In addition, regular peaks of the amplitude of approximately $2\ rad/s$ can be seen showing up every $0{,}02\ s$ which means they appear at every single revolution ($\frac{2\pi\ [rad]}{314\ [rad/s]} = 0{,}02\ [s]$).

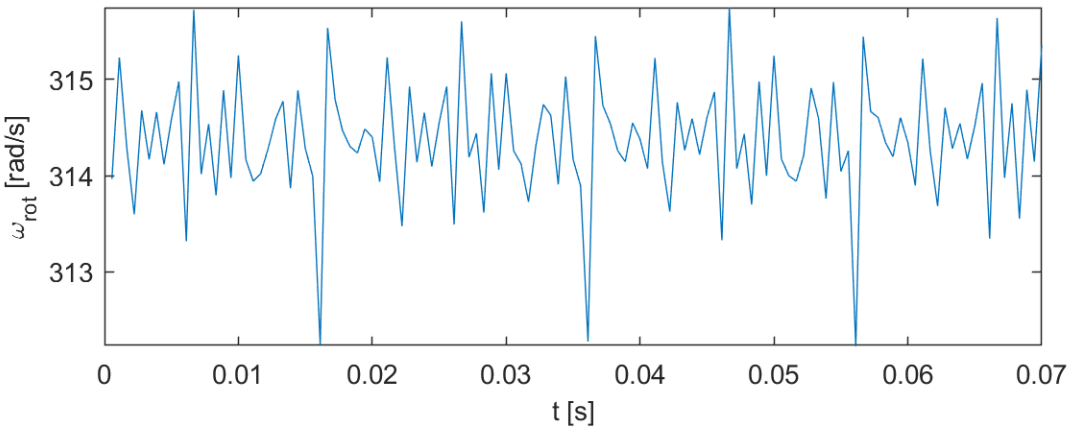


*Fig. 3.15 Computed rotor angular speed*

Looking at Fig. 3.15, it is obvious that the angular speed computation in its simplest form is not suitable for practical use. The resultant signal contains elements which do not correspond to the actual motion of the rotor.
A question is which part of Eq. 3.50 contaminates the resultant signal with these undesirable elements. Is it the term in the numerator relating to the encoder geometry or is it the denominator relating to the detection times? A clue to answer this question provides the fact that the undesired elements show up at a frequency equal to the rotor rotational frequency. Yes, theoretically there could be a measurement error showing up at a frequency equal to the rotational frequency but there is no physical reason for that. Thus, it is reasonable to focus on the way how the angular positions of the encoder stripes are represented. We accept that the encoder marks are not equidistant and we use the encoder geometry estimation system derived earlier in Chapter 3.2.

### 3.3.3 Velocity computation algorithm incorporating the encoder geometry estimation

As shown, the simple algorithm for angular speed computation described in Chapter 3.3.2 does not yield satisfactory results. The reason for that is that the size of the encoder stripes is not constant. This is why we developed a separate algorithm for encoder geometry estimation.
The objective of this chapter is to link the knowledge from Chapter 3.2 to advance the basic algular speed computation formula given by Eq. 3.50. This will give us the final form of the algorithm for rotor instantaneous angular speed evaluation.
First, recall the estimation system for encoder geometry

$$\begin{aligned} \phi_i(k+1) &= \phi_i(k) + \xi_i(k) \quad [rad] \\ y_i(k) &= \phi_i(k) + \eta_i(k) \quad [rad] \end{aligned}, \tag{3.51}$$

where the quantity $y_i(k)$ is a function of time increments according to the following relation (detailed derivation can be found in Chapter 3.2.1)

$$y_i(k) \triangleq \frac{2\pi t_i(k)}{\sum_{j=i+1}^{N} t_j(k-1) + \sum_{j=1}^{i} t_j(k)} = 2\pi \frac{t_i(k)}{T}. \tag{3.52}$$

These equations will be incorporated into the angular speed equation

$$\omega_i = \frac{\phi_i(k)}{t_i(k)}. \tag{3.53}$$

The nominator in Eq. 3.53 is the gap width at stripe $i$ and the denumerator is the time increment over that same gap. After substitution
Thus, we get

$$\omega_i = \frac{\hat{\phi}_i(k)\big(1 - K_i(k)\big) + 2\pi K_i(k)\frac{t_i(k)}{T}}{t_i(k)}. \tag{3.54}$$

Eq. 3.54 presents the final form of the algorithm for rotor instantaneous angular speed evaluation. It includes the Kalman filter for encoder geometry estimation that was developed in Chapter 3.2.

## 3.4 Error of the encoder geometry and angular speed calculation

As shown in previous parts of Chapter 3, the path from measuring the detection times of the encoder stripes to the resulting torsional vibration signal is a chain of several steps. Each element of this chain brings certain error to the result. The goal of this chapter is to present and analyse these partial sources of error.

Specifically, we focus on the random measurement noise, the choice of the measuring principle, the SNR of the sensor used and the systematic error of the proposed algorithm for calculating the instantaneous angular speed.

### 3.4.1 Random measurement noise

The designed torsional vibration method starts with measuring the incremental encoder signal. The idealized course of that signal was shown in Fig. 3.2 and a portion of a real signal was shown in Fig. 3.7. Random noise contained in the measured signal affects the accuracy of the rising edge detection in this signal. It can be shown that the steeper the leading edge, the less is the effect of signal noise to the detection time evaluation.

Let the sensor output $x(t)$ consist of a useful signal $x^*(t)$ and an additive white noise $\kappa(t) \sim N(0, \sigma_x^2)$. Therefore, $x(t) = x^*(t) + \kappa(t)$. The leading edge detection time is determined as the time at which the signal $x(t)$ exceeds a predefined threshold value. The additive noise $\kappa$ modelled as a white noise with a variance $\sigma_x^2$ is a physical cause of the error in the determination of the rising edge time of arrival. This error can, similarly, be modelled as a white noise with a variance $\sigma_t^2$ and the following relation holds

$$\sigma_t^2 = \tan\gamma \cdot \sigma_x^2. \tag{3.55}$$

The validity of this relationship can be seen by the illustration in Fig. 3.16.

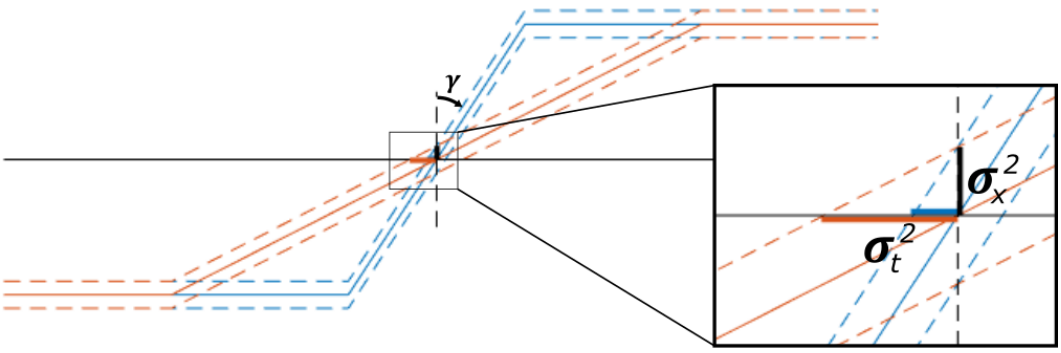


*Fig. 3.16 Sensitivity of the result on the slope of the rising edge.*

According to Eq. 3.55, the detection time variance is directly proportional to the measured signal variance provided the angle of the rising edge is constant. Alternatively, for a given measurement variance the detection time variance is directly proportional to $\tan\gamma$ where $\gamma$ is the slope angle of the leading edge. The latter statement implies that a signal with steeper rising edges is, in general, more robust to additional measurement noise.

### 3.4.2 Systematic error of the instantaneous angular speed calculation algorithm

In this chapter we will analyse the influence of torsional vibration, or more generally of the variability of the rotor angular speed, on the computed encoder geometry. We will perform the analysis for two special cases. The first case is an uniformly accelerated/decelerated motion in which the rotor is subject to a constant acceleration or deceleration. The second case is a harmonic motion that simulates the case of torsional vibration.
First, consider an uniformly accelerated motion described by the following equation of motion

$$\omega(t) = \omega_{rot} + \alpha t, \tag{3.56}$$

where $\omega(t)$ represents the instantaneous angular speed at time $t$, $\omega_{rot}$ the initial angular speed and $\alpha$ the angular acceleration of the rotor. By integrating Eq. 3.56 and assuming a zero initial condition, the relation for the instantaneous angular position can be written as

$$\varphi(t) = \omega_{rot} t + \frac{1}{2}\alpha t^2. \tag{3.57}$$

For a specific $i$-th encoder gap of the width $\varphi(t) = \varphi_i$ and with a time increment $t_i$ we get

$$t_i = \frac{-\omega_{rot} + \sqrt{\omega_{rot}^2 + 2\varphi_i \alpha}}{\alpha}. \tag{3.58}$$

Similarly, the period of rotation $T$ can be obtained by the substitution $\varphi \equiv 2\pi$. As a sidenote, who reads this sentence deserves great admiration from the author of the thesis. Thus, we get

$$T = \frac{-\omega_{rot} + \sqrt{\omega_{rot}^2 + 4\pi\alpha}}{\alpha}. \tag{3.59}$$

For the following discussion, let us first consider Eq. 3.44 which presents the Kalman filter state equation. It is a recursive equation where the Kalman gain $K$ controls the weight of the previous value of the state variable compared to the measured value on the actual value of the state variable. Considering a special case of $K = 1$ we get a situation where the filter output is purely dictated by the measurement. This is helpful for current analysis, as we can directly substitute from Eq. 3.17 into 3.44 and get

$$\varphi_i^* = 2\pi \frac{t_i}{T} = 2\pi \frac{-\omega_{rot} + \sqrt{\omega_{rot}^2 + 2\varphi_i \alpha}}{-\omega_{rot} + \sqrt{\omega_{rot}^2 + 4\pi\alpha}}. \tag{3.60}$$

As a cross-check, the value $\varphi_i^*$ can be calculated at zero acceleration $\alpha = 0$. Because this would lead to a limit of the type „0/0“ the L'Hospital can be employed (note all requirements for the L'Hospital rule are met). Hence, we get

$$\varphi_i^*|_{\alpha=0} = \lim_{\alpha\to 0} 2\pi \frac{-\omega_{rot} + \sqrt{\omega_{rot}^2 + 2\varphi_i \alpha}}{-\omega_{rot} + \sqrt{\omega_{rot}^2 + 4\pi\alpha}} = \lim_{\alpha\to 0} 2\pi \frac{\frac{1}{2}\frac{\omega_{rot}^2 + 2\varphi_i\alpha}{\sqrt{\omega_{rot}^2 + 2\varphi_i\alpha}} \cdot 2\varphi_i}{\frac{1}{2}\frac{\omega_{rot}^2 + 4\pi\alpha}{\sqrt{\omega_{rot}^2 + 4\pi\alpha}} \cdot 4\pi} = \varphi_i. \tag{3.61}$$

Equation 3.61 proves that in case of unaccelerated rotational motion the calculated gap width $\varphi_i^*$ is just equal to the actual gap width $\varphi_i$.

A useful quantity will be the relative error of the calculated gap width obtained as a subtraction of the calculated and actual gap width divided by the mean gap width

$$\epsilon \triangleq \frac{\varphi_i^* - \varphi_i}{2\pi/N}. \tag{3.62}$$

After substitution from Eq. 3.60 into 3.62 we get

$$\epsilon = \frac{N}{2\pi} \cdot \left( 2\pi \frac{-\omega_{rot} + \sqrt{\omega_{rot}^2 + 2\varphi_i \alpha}}{-\omega_{rot} + \sqrt{\omega_{rot}^2 + 4\pi\alpha}} - \varphi_i \right) \tag{3.63}$$

and after a small adjustment

$$\epsilon = N \cdot \frac{\sqrt{1 + 2\varphi_i \alpha / \omega_{rot}^2} - 1}{\sqrt{1 + 4\pi\alpha / \omega_{rot}^2} - 1} - \frac{N\varphi_i}{2\pi}. \tag{3.64}$$

From a practical point of view, it will be useful to analyse 2 dependencies:

1. $\epsilon = \epsilon(\varphi_i)$
2. $\epsilon = \epsilon(\alpha)$

The dependency of the computed $i$-th gap width on its index $i$, in other words on its position relative to the phase stripe, is shown in Fig. 3.17. It can be seen that the error reaches the maximum value around the $25^{th}$ stripe, i.e. in the middle of the revolution.

Practical consequence is that during the machine start-up the method will systematically yield wrong computed angular positions of the encoder stripes. This error would not be eliminated even by the filtering algorithm from Chapter 3.2.7.

From a quantitative point of view, the magnitude of the error in the order of $10^{-5}$, i.e. about $10^{-3}$ %, can be assessed as insignificant.

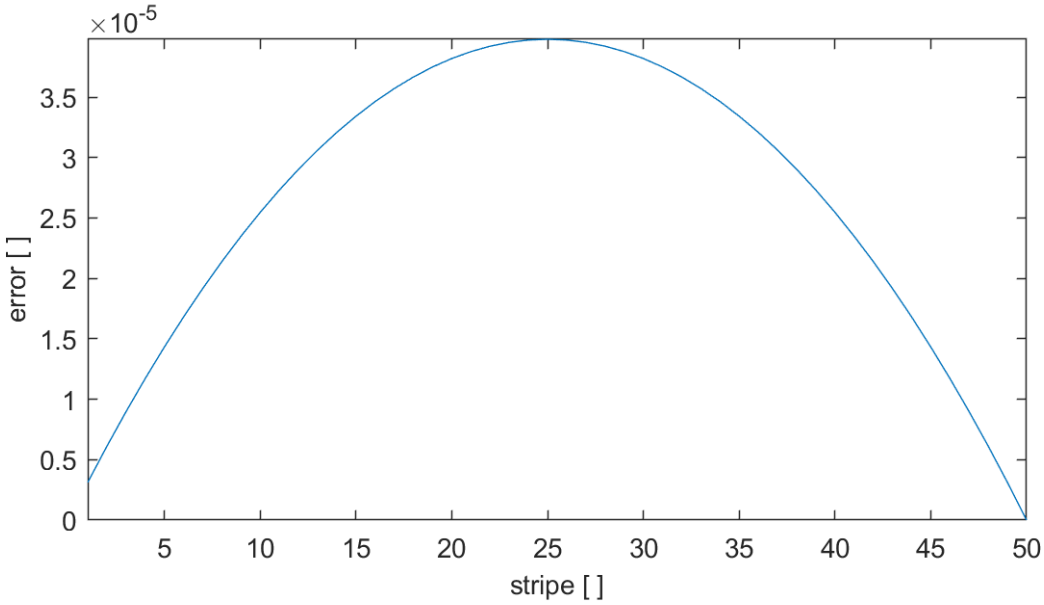


***Fig. 3.17 The systematic error of the calculated angular position of the encoder stripes depending on their location.***

Figure 3.18 shows the error $\epsilon$ of the computed angular position of the first encoder stripe depending on the rotor acceleration $\alpha$. As expected the error linearly increases as the acceleration increases. At zero acceleration the error is zero as already shown before.

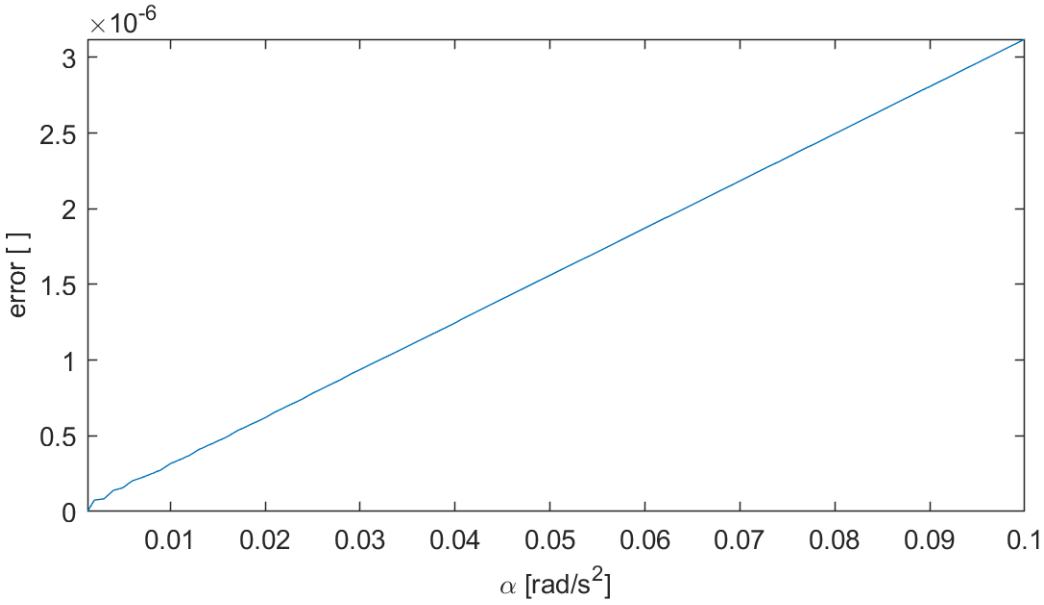


*Fig. 3.18 The systematic error of the computed angular position of the first encoder stripe depending on the rotor acceleration.*

In the following the case of harmonic fluctuation of the angular speed will be considered. This reflects the situation of simple harmonic torsional vibration.
In this case, the angular speed is described by the following equation

$$\omega(t) = \omega_{rot} + A\sin(2\pi f t + \phi)\,, \tag{3.65}$$

where $\omega(t)$ presents the instantaneous angular speed at time $t$, $\omega_0$ is the DC component of angular speed, $A$ is the torsional vibration amplitude in the units of angular speed, $f$ is the frequency of torsional vibration and $\phi$ is the initial phase of the harmonic oscillation relative at time $t = 0$. By the integration of Eq. 3.65 and assuming zero initial conditions the equation for instantaneous angular displacement can be rewritten as

$$\varphi(t) = \omega_{rot} t - \frac{A}{2\pi f}\cos(2\pi f t + \phi) + \frac{A}{2\pi f}\cos(\phi)\,. \tag{3.66}$$

Equation 3.66 is a transcendent equation whose general analytical solution for $t$ does not exist. However, using numeric solvers, solutions can be found for specific values of $\varphi$, $\omega_{rot}$, $A$, $f$ a $\phi$.
As in the previous case, special attention will be paid to the dependence $t = t(\varphi_i)$, which will now be extended by the initial phase $\phi$. Hence we get a function of two variables $t = t(\varphi_i, \phi)$. The three-dimensional plot of the function $t = t(\varphi_i, \phi)$ is shown in Fig. 3.19. The remaining parameters are set as follows: $\omega_{rot} = 2\pi \cdot 50 = 314\ rad/s$, $A = 1 \cdot 10^{-3}\ rad/s$, $f = 20\ Hz$.

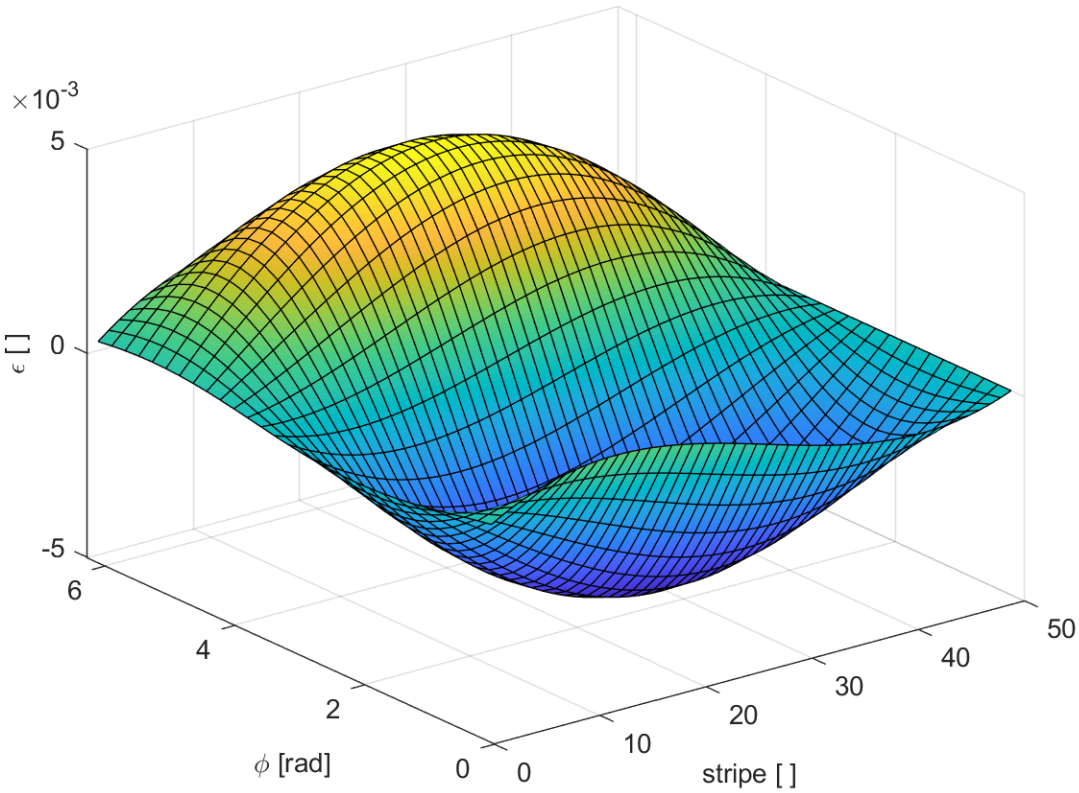


***Fig. 3.19 Three dimensional plot of the function $t = t(\varphi_i, \phi)$.***

On one hand, after averaging over the axis of initial phases $\phi$ the error $\epsilon$ is zero for all stripes. On the other hand, averaging over the entire interval of the initial phases $0 < \phi \leq 2\pi$ does not occur in practise. This is an interesting fact that will now be proved.
Consider torsional vibration at the frequency of 20 Hz, i.e. period 0,05 s, superimposed on a rotational frequency $f_{rot} = 50\ Hz$, i.e. rotational period 0,02 s. As a result only 5 distinguish initial phases $\phi$ exist reoccuring with a period of 0,1 s. In fact this number is the least common multiple of the numbers 0,02

and 0,05. This principle is illustrated in Fig. 3.20 which shows the relative position of two harmonic functions with frequencies of 20 Hz and 50 Hz. In addition, the black lines depict the phase of the „20 Hz“ harmonic function at the times when the „50 Hz“ harmonic function starts a new period, i.e. when the rotor starts a new revolution. It can be seen that 5 different initial phases exist on any time interval of 0,1 s.

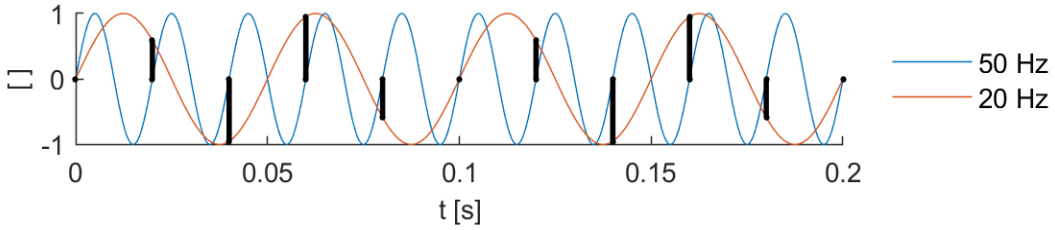


*Fig. 3.20 Relative position of two harmonic functions at frequencies 20 Hz and 50 Hz.*

However, a remarkable fact is shown in Fig. 3.21. The existence of only 5 different initial phases $\phi$ has no effect on increasing the error in the calculation of angular positions by averaging. Figure 3.21 shows the error of the angular positions after averaging over the entire interval $0 < \phi \leq 2\pi$ (blue line with crosses) and Fig. 3.22 shows the error after averaging over the set of five reachable initial phases (red line).

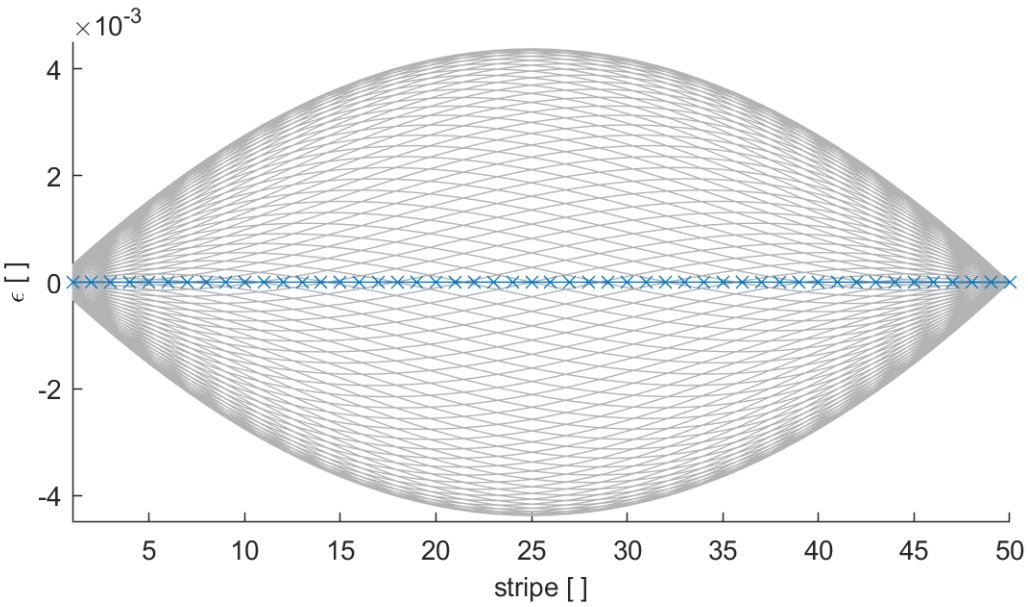


*Fig. 3.21 Error of the angular positions after averaging over the entire interval* $\mathbf{0 < \phi \leq 2\pi}$ *(blue line with crosses).*

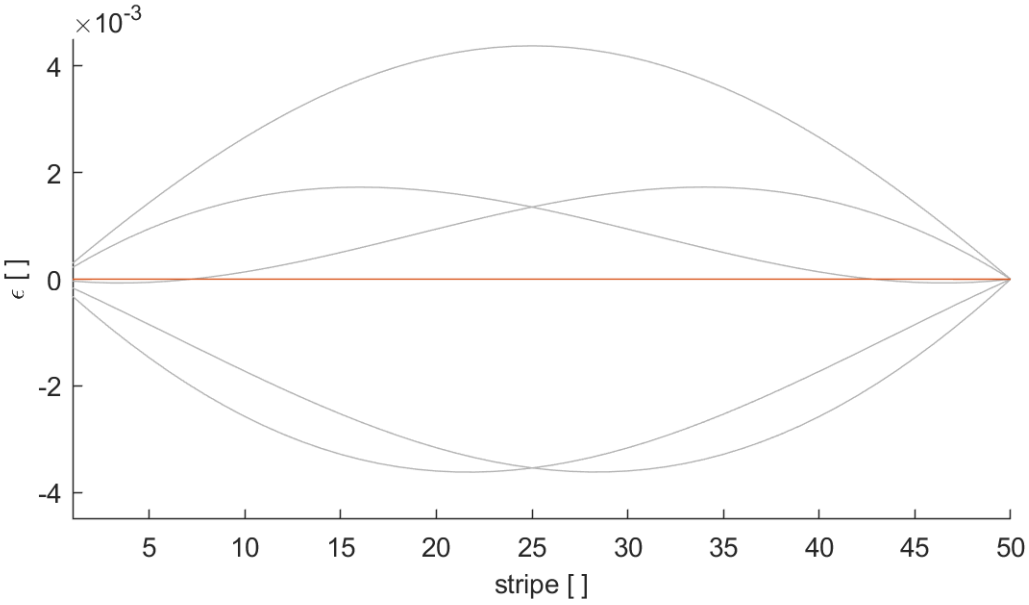


***Fig. 3.22 Error of the angular positions after averaging over the set of five reachable initial phases (red line).***

As can be seen in Fig. 3.22 the error is zero also if only the five reachable initial phases are used in the averaging. This property applies in general, which will be analytically proven in the next paragraph.

<u>Proof:</u>
Consider a harmonic function of frequency $f$ and be interested in the sum of its values in equidistant time intervals $\tau_i, i = 1, \dots, n, n \in \mathbb{N}$ represented by

$$s = \sum_{i=1}^{n} \sin(2\pi f \tau_i + \phi_0)\,. \tag{3.67}$$

In addition, let $\tau_n = \frac{m}{f}, m \in \mathbb{N}$, hence more generally $\tau_i = \frac{i}{n}\frac{m}{f}$. The sum according to Eq. 3.67 can be rewritten in the form

$$s = \sum_{i=1}^{n} \sin\left(2\pi i \frac{m}{n} + \phi_0\right), \tag{3.68}$$

$$s = \sum_{i=1}^{n} \left[\sin\left(2\pi i \frac{m}{n}\right)\cos\phi_0 + \cos\left(2\pi i \frac{m}{n}\right)\sin\phi_0\right]\,, \tag{3.69}$$

$$s = \cos\phi_0 \sum_{i=1}^{n-1} \sin\left(2\pi i \frac{m}{n}\right) + \sin\phi_0 \sum_{i=1}^{n} \cos\left(2\pi i \frac{m}{n}\right). \tag{3.70}$$

The next step will be to prove that both sums on the right side of Eq. 3.66 are under the condition that $m, n \in \mathbb{N}$ equal to zero. First, the following identity will be used whose proof will be left on the reader

$$\sum_{i=1}^{n} \sin\left(2\pi i \frac{m}{n}\right) = 0 \ \wedge \ \sum_{i=1}^{n} \cos\left(2\pi i \frac{m}{n}\right) = 0 \Leftrightarrow \sum_{i=1}^{n} e^{j\left(2\pi m \frac{i}{n}\right)} = 0. \tag{3.71}$$

The term $\sum_{i=1}^{n} e^{j\left(2\pi m \frac{i}{n}\right)}$ is a sum of complex numbers thus also a complex number. A complex number is zero if and only if the real and imaginary parts are both zero.

It will be useful to first deal with the case where $m = 1$. In this case, the phasors of complex numbers $e^{j\left(2\pi \frac{i}{n}\right)}$ in the complex plane form a symmetrical pattern and their sum will therefore always be zero, see the upper left plot in Fig. 3.23.

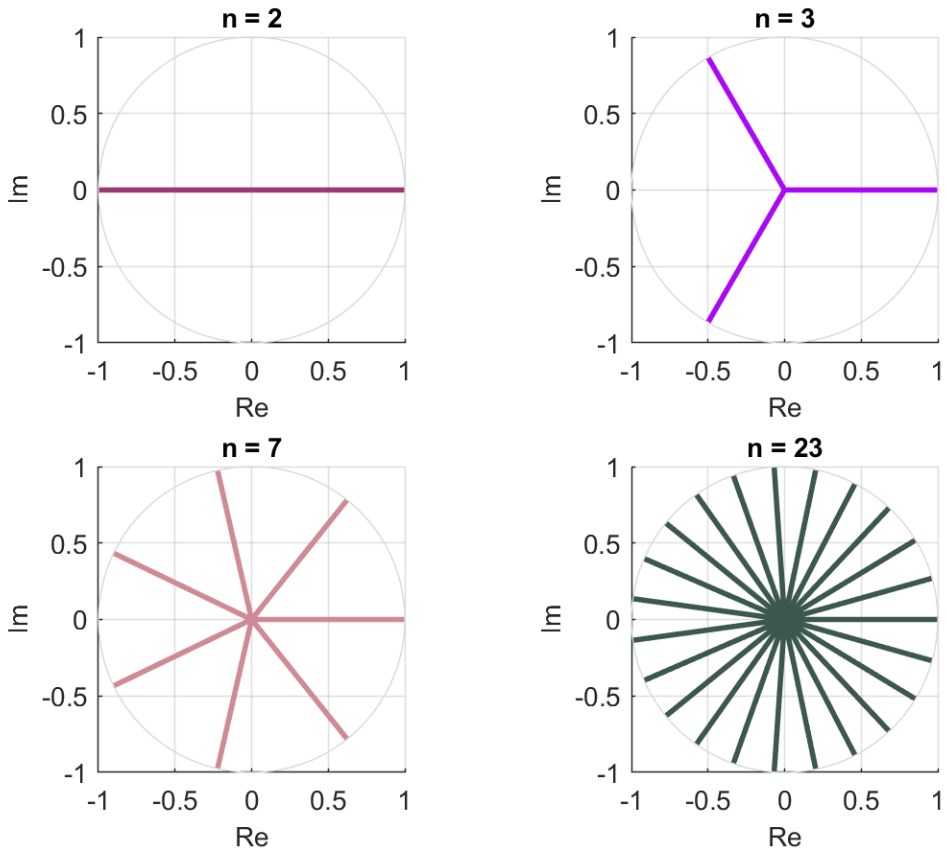


***Fig. 3.23 Demonstration of the principle that the sum of complex exponentials according to Eq. 3.37 is always zero.***

For a general value of $n \in \mathbb{N}$, it can be noticed that the expression $\sum_{i=1}^{n} e^{j\left(2\pi m \frac{i}{n}\right)}$ is a sum of $n$ complex numbers, whose position vectors in complex plane uniformly divide the angle $2\pi m$. What happens if $m = 2$, e.g. in case of $n = 23$? The angle between two adjacent position vectors is doubled, but the resulting pattern is the same as in the lower right plot in Fig. 3.23.

$$\begin{array}{ccccc}
e^{j\left(2\pi \cdot 1 \cdot \frac{m}{n}\right)} & + \cdots + & e^{j\left(2\pi \cdot n \cdot \frac{m}{n}\right)} & + \\
e^{j\left(2\pi \cdot 1 \cdot \frac{m}{n}\right)} e^{j\left(2\pi \frac{1}{n}\right)} & + \cdots + & e^{j\left(2\pi \cdot n \cdot \frac{m}{n}\right)} e^{j\left(2\pi \frac{1}{n}\right)} & + \\
\vdots & & \vdots & \\
e^{j\left(2\pi \cdot 1 \cdot \frac{m}{n}\right)} e^{j\left(2\pi \frac{m-1}{n}\right)} & + \cdots + & e^{j\left(2\pi \cdot n \cdot \frac{m}{n}\right)} e^{j\left(2\pi \frac{m-1}{n}\right)} &
\end{array}$$

$$\sum_{i=1}^{n-1} \sin\left(2\pi i \frac{m}{n}\right) = \frac{1}{2}\left(\sum_{i=1}^{n-1} \sin\left(2\pi i \frac{m}{n}\right) + \sum_{i=1}^{n-1} \sin\left(2\pi (n-i) \frac{m}{n}\right)\right) =$$
$$\frac{1}{2}\sum_{i=1}^{n-1}\left[\sin\left(2\pi i \frac{m}{n}\right) + \sin(2\pi)\cos\left(2\pi \frac{im}{n}\right) - \cos(2\pi)\sin\left(2\pi \frac{im}{n}\right)\right] =$$
$$\frac{1}{2}\sum_{i=1}^{n-1}\left[\sin\left(2\pi i \frac{m}{n}\right) + 0 \cdot \cos\left(2\pi \frac{im}{n}\right) - 1 \cdot \sin\left(2\pi \frac{im}{n}\right)\right] = 0 \tag{3.72}$$

$$\sum_{i=1}^{n} \cos\left(2\pi i \frac{m}{n}\right) = \frac{1}{2}\left(\sum_{i=1}^{n} \cos\left(2\pi i \frac{m}{n}\right) + \sum_{i=1}^{n} \cos\left(2\pi (n-i) \frac{m}{n}\right)\right) =$$
$$\frac{1}{2}\sum_{i=1}^{n}\left[\cos\left(2\pi i \frac{m}{n}\right) + \cos(2\pi m)\cos\left(2\pi i \frac{m}{n}\right) + \sin(2\pi m)\sin\left(2\pi i \frac{m}{n}\right)\right] =$$
$$\frac{1}{2}\sum_{i=1}^{n}\left[\cos\left(2\pi i \frac{m}{n}\right) + 1 \cdot \cos\left(2\pi i \frac{m}{n}\right) + 0 \cdot \sin\left(2\pi i \frac{m}{n}\right)\right] \tag{3.73}$$

In this case, the property of the cosine function was used, that $\cos\left(2\pi n \frac{m}{n}\right) = \cos\left(2\pi \cdot 0 \cdot \frac{m}{n}\right)$.

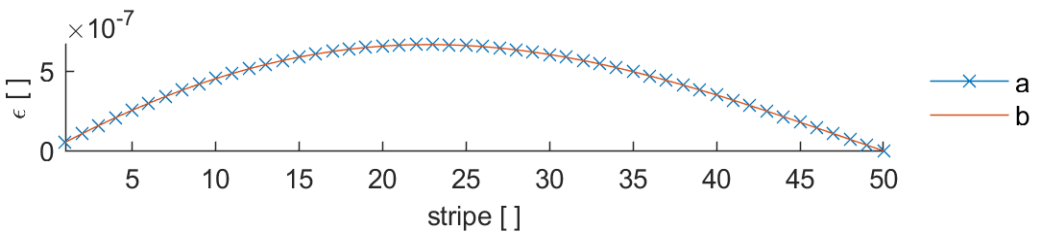


*Fig. 3.24 Error of the angular positions after averaging over all initial phases.*

A repeated solution can be used to construct the function $t = t(\varphi_i)$, which determines the encoder stripes detection times. Having this function the formula for the angular position of the $i$-th stripe can be written as

$$\varphi_i^* = 2\pi \frac{t(\varphi_i)}{t(2\pi)}. \tag{3.74}$$

The error of the calculated angular position will be written by the following equation

$$\epsilon \triangleq \frac{\varphi_i^* - \varphi_i}{2\pi/N}. \tag{3.75}$$

After the substitution

$$\epsilon \triangleq N \frac{t(\varphi_i)}{t(2\pi)} - \frac{N\varphi_i}{2\pi}. \tag{3.76}$$

The dependence of the error of the calculated angular position of the $i$-th mark on its index $i$ is shown in Fig. 3.25. It can be seen that the maximum value is reached around the 16th encoder mark. In addition, on the other parts the function is not monotonous any more as opposed to the situation in Fig. 3.24. Namely, there is a local minimum around the 47th encoder mark.

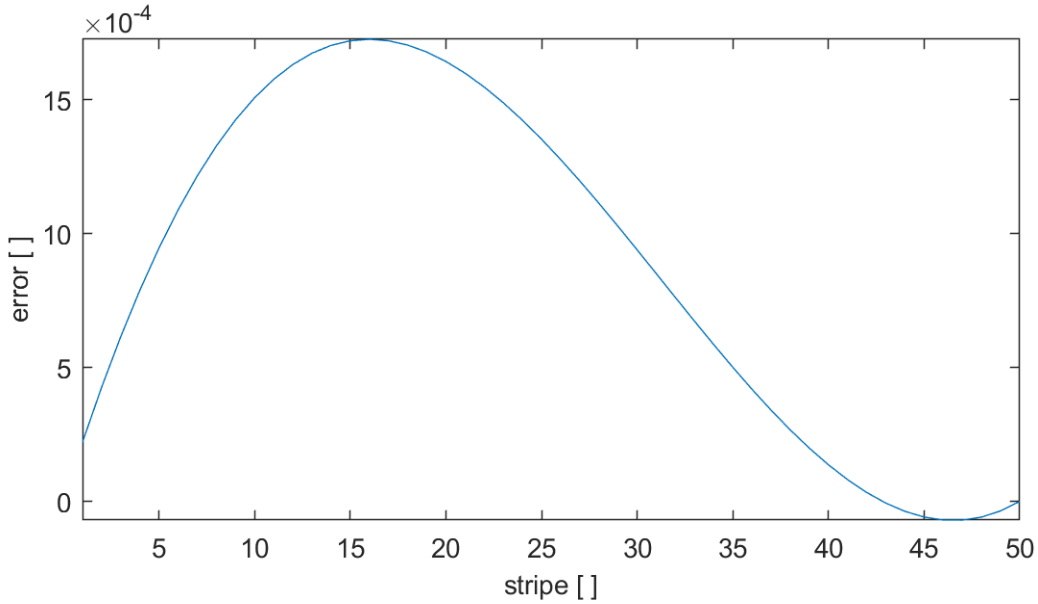


*Fig. 3.25 Error of the angular positions after averaging after averaging over all initial phases..*

However, the shape of the curve in Fig. 3.25 depends on the initial phase of the harmonic component of the rotor speed and to properly evaluate the effect of torsional vibration, it will therefore be appropriate to extend the graph by another dimension representing the initial phase of the harmonic component.

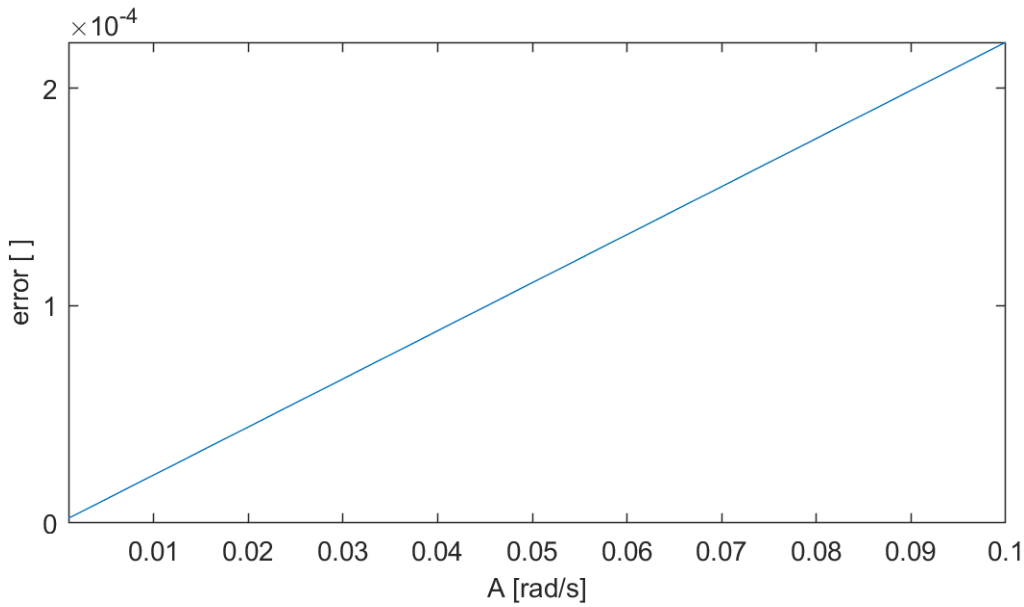


*Fig. 3.26 Error of the angular position of the 1st encoder stripe as a function of torsional vibration amplitude.*

### 3.4.3 The problem of oscillation at the rotational frequency and its multiples

In this chapter we will discuss one major structural limitation that exists when using a simple incremental encoder of unknown geometry for torsional vibration evaluation. This limitation is that torsional oscillations at the rotational frequency and its multiples can not be distinguished from the encoder geometry error.

We will first answer the question of when this fact is really limiting. Are there situations in practice where the rotor oscillates synchronously with its rotation? As for oscillations at natural frequencies, rotors are typically designed so that their natural torsional frequencies are not close to the nominal rotational frequency and multiples thereof. However, the situation is different for forced oscillation caused by harmonic fluctuations of the air-gap torque. As was discussed for example in Chapter 2.2, when the three-phase network is unbalanced, an air-gap torque component is created in the generator oscillating at twice the network frequency, i.e. at 100 Hz. In the case of two-pole synchronous machines, it is therefore an excitation at twice the rotational frequency. This would be the situation where the described limitation comes into play. On the contrary, this limitation does not apply to asynchronous machines operating with a certain frequency slip to the mains frequency or to oscillations at a frequency other than synchronous.

Table 3.1 presents an overview of combinations of generator frequency slip during operation and frequency of torsional vibrations. Recall zero slip reflects the synchronous machines and non-zero slip reflects asynchronous machines. Only case 4. is subject to the limitation discussed in this chapter.

| | |
|---|---|
| 1. Non-zero slip, non-synchronous vibration | 2. Zero slip, synchronous vibration |
| 3. Non-zero slip, non-synchronous vibration | 4. Zero slip, synchronous vibration |

***Tab. 3.1 Overview of combinations of generator frequency slip during operation and frequency of torsional vibrations. Only case 4. is subject to the limitation discussed in this chapter.***

For a better understanding, the situation can also be represented graphically, as in Fig. 3.29. This figure is divided into four parts that correspond to the definitions of the operating state according to Tab. 3.1. First, we explain how to interpret the figures. The black thick circle shows the circumference of the rotating rotor. The position of the stationary sensor of the incremental encoder is represented by the black circle on the right adjacent to the circle. Thanks to the blue and red lines, the mutual movement of the rotor and the excitation air-gap torque can be read.

The blue line can be thought of as a record of the angular speed of the rotor over time. For each point, the angle of its position vector is given by the momentary rotation angle of the rotor from the beginning of the measurement, and its amplitude is given by the momentary angular speed. As the angular speed in our model example is given by the superposition of the nominal rotational speed and an additive harmonic component representing the torsional oscillation, the amplitude of the position vector fluctuates between two concentric circles representing the resulting extreme values of the rotor angular speed.

The red line can be imagined as a record of the time course of the air-gap torque. For each point, the angle of its position vector is given by the momentary rotation angle of the rotor from the beginning of the measurement, and its amplitude is given by the momentary air-gap torque amplitude. As the air-gap torque in our model example is given by the superposition of a nominal value and an additive harmonic component representing the torsional oscillation, the amplitude of the position vector fluctuates between two concentric circles representing the resulting extreme values of the air-gap torque.

In our model example, we suppose the mains frequency is fixed to 50 Hz. In cases 1. and 2., where non-zero slip is indicated, the rotor rotation frequency is 10% below mains frequency, i.e. 45 Hz. This means that on the 0,08 s time window of 4 mains revolutions the rotor ends up in a position delayed by $4 \cdot 360°/10 = 144°$. This fact is highlighted by the blue arrows indicating the position vector of the final point on the blue line. On the other hand, in cases 3. and 4. there is zero slip therefore the rotor motion keeps in unison with the mains frequency. Again, this fact is highlighted by the blue arrows being collinear with the red arrows.

In cases 1. and 3. we consider non-synchronous vibration (there is a harmonic component in the air-gap torque oscillating at 120 Hz). This fact reflects itself in the shape of the red lines. After the end of one mains revolution the phase of the vibration does not end up at the initial value but has an advance of

$$360° \cdot \frac{\frac{1}{50} - \frac{1}{120}}{\frac{1}{120}} \,\%\, 360 = 144°$$

in every mains revolution. On the other hand, in cases 2. and 4. we consider synchronous vibration. This means the value of the air-gap torque for a particular mains phase is the same in all revolutions. Therefore the red lines overlap on our 0,08 s time interval of 4 revolutions and form a single ellipse-like shape.

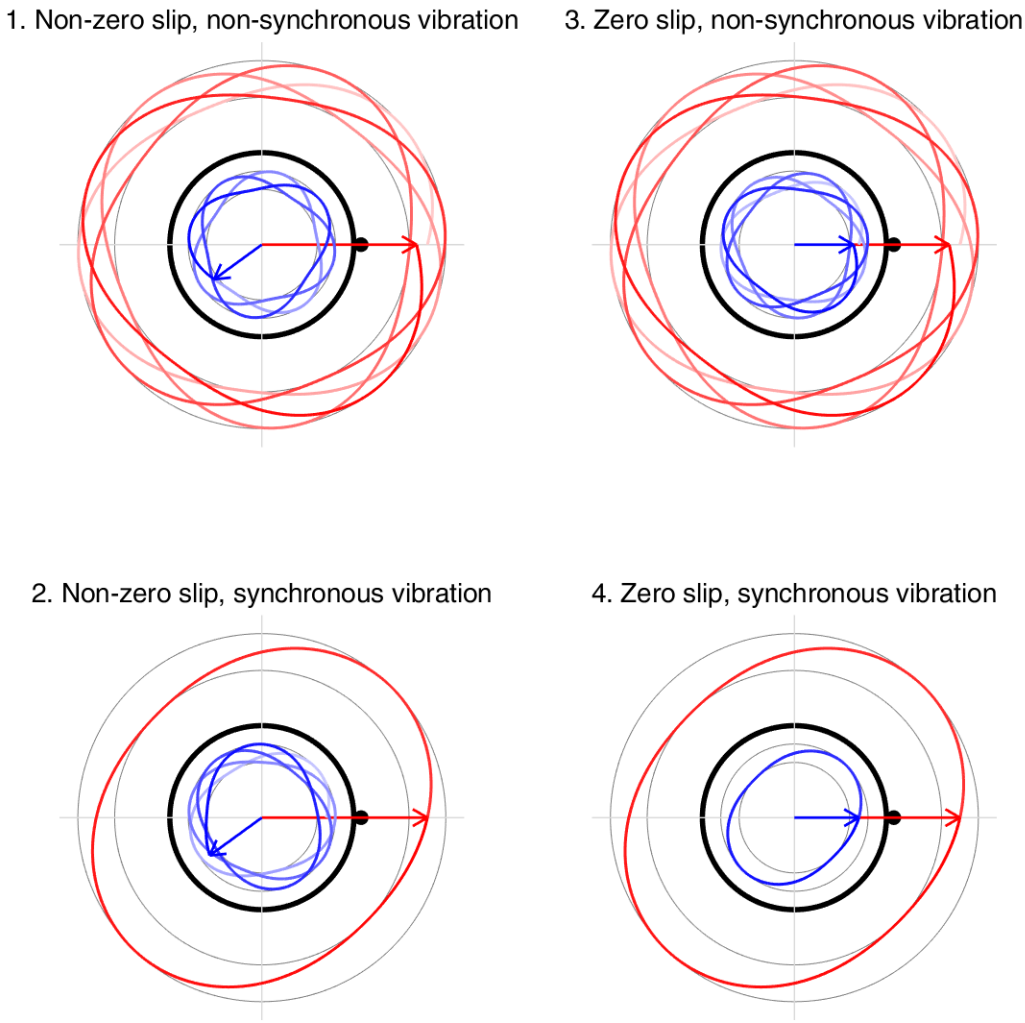


*Fig. 3.27 Excitation force (red) and rotor acceleration (blue).*

Now let's realize what is relevant in terms of influencing the encoder geometry calculation by the existence of torsional oscillation. In order for the recursive algorithm to yield an unbiased value of the gap width estimate, it is necessary that the torsional oscillation does not always affect a given gap in the same way, but that the positive and negative contributions from the torsional oscillation be distributed as best as possible, i.e. the blue line has at a specific point for different revolutions different values. This condition is obviously fulfilled in all cases except case 4. In case 4, for each encoder stripe the contribution from torsional oscillation will be the same in each revolution, and it will not be possible to distinguish the effect of torsional oscillation from the error of the encoder geometry. For a specific

example, if due to torsional oscillations the rotor is always slowed down at the moment when the $i$-th strip passes around the sensor, this fact will not be distinguishable from the condition where the $i$-th stripe would be oversized compared to other stripes.

## 3.5 Programmatic implementation of the algorithm

The algorithm for torsional vibration evaluation described in this chapter has been developed and tested extensively in Matlab software. However, for the practical use on power plants a copy in LabVIEW software has been made. The LabVIEW environment brings several benefits such as

- clarity of interconnections between functional blocks
- the possibility of color differentiation of functional blocks according to their classification into a logical unit
- easy connection to the used HW from NI
- easier code readability for people unfamiliar with the code

The following figure shows an example snippet from the code. The function block nature of the code can be seen. Furthermore, the hierarchical structure of multiple sub-VI levels and the united coloring of sub-VIs of similar logical function can also be seen (note the pink sub-VIs on the right side).

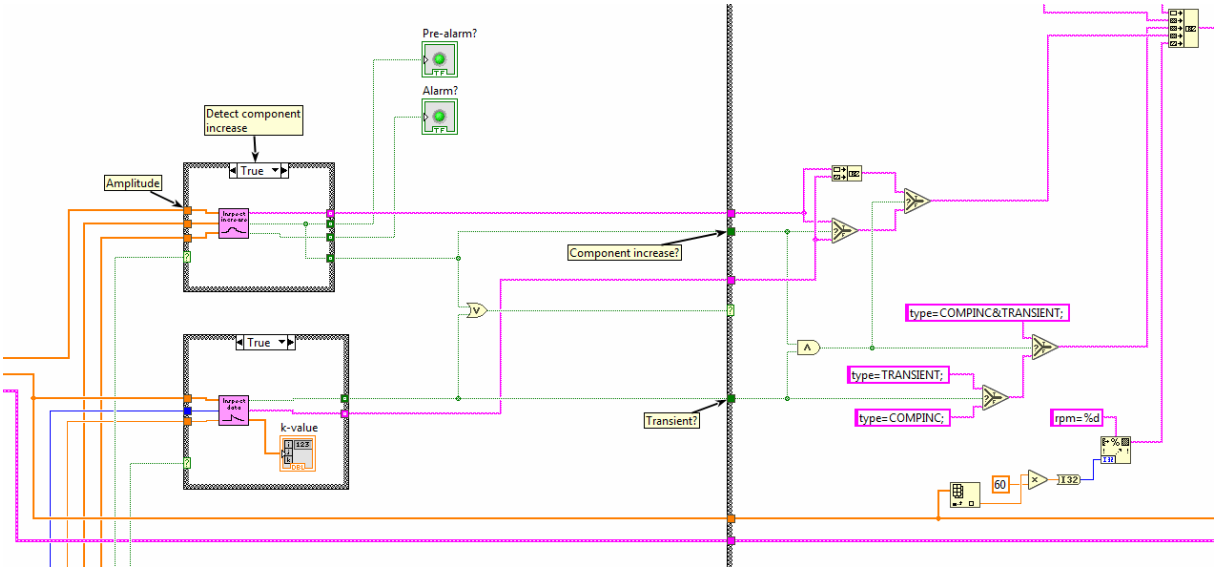


*Fig. 3.28 Example snippet of the LabVIEW code.*

The LabVIEW environment is also beneficial by providing an easy graphical user interface (GUI) capability. The GUI of the torsional vibration monitoring system has been designed with respect to clarity and functionality. It allows the user to set all necessary parameters and show important values and graphs.

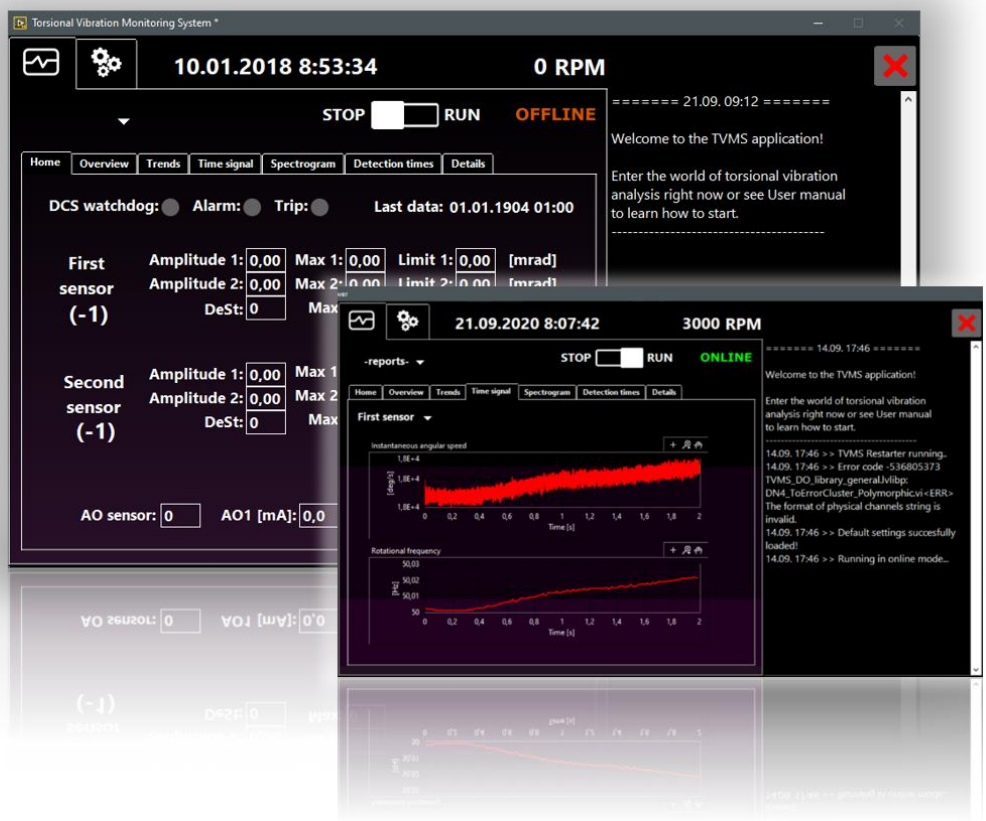


*Fig. 3.29 Graphical user interface.*

# 4 Practical case studies for the analysis of torsional vibration interaction with the power grid

In this chapter, several practical case studies will be presented. They allow us to show the correct functioning of the proposed algorithm for the evaluation of instantaneous angular speed and torsional vibrations and its applicability in the detection of manifestations of electro-mechanical interaction of the power grid and the turbine-generator units.
In order to avoid possible misunderstanding, let us state that all input data were obtained based on measurements in power plants using the hardware and procedures presented in this thesis and were subsequently processed also in the spirit of the methods also developed in this thesis.
Some case studies presented in this chapter stand out by documenting rare instances of interaction. It can be said that we were lucky in these cases and were in the right place at the right time. These highlights are definitely

- evaluation of torsional vibrations of the turbine-generator rotor of a 385 MW unit of a coal-fired power plant in the event of a three-phase short circuit at the generator terminals
- detection of manifestations of interaction between the power grid and turbo-generators in a network characterized by a long unbranched line
- capturing a transient event resulting in torsional vibration response with LP turbine blade vibration excitation
- analysis of torsional vibration together with generator terminal voltage signal at the time of a major power grid disturbance

## 4.1 Subsynchronous torsional vibration resonance events

This chapter will cover several case studies related to such a turbine-generator torsional vibration interaction with the power grid that has a nature of a resonance event. All case studies are associated with the same power plant. In the beginning we will introduce the powerplant setup and it's context in the power grid. This will help us to understand the phenomena that we are about to analyse.

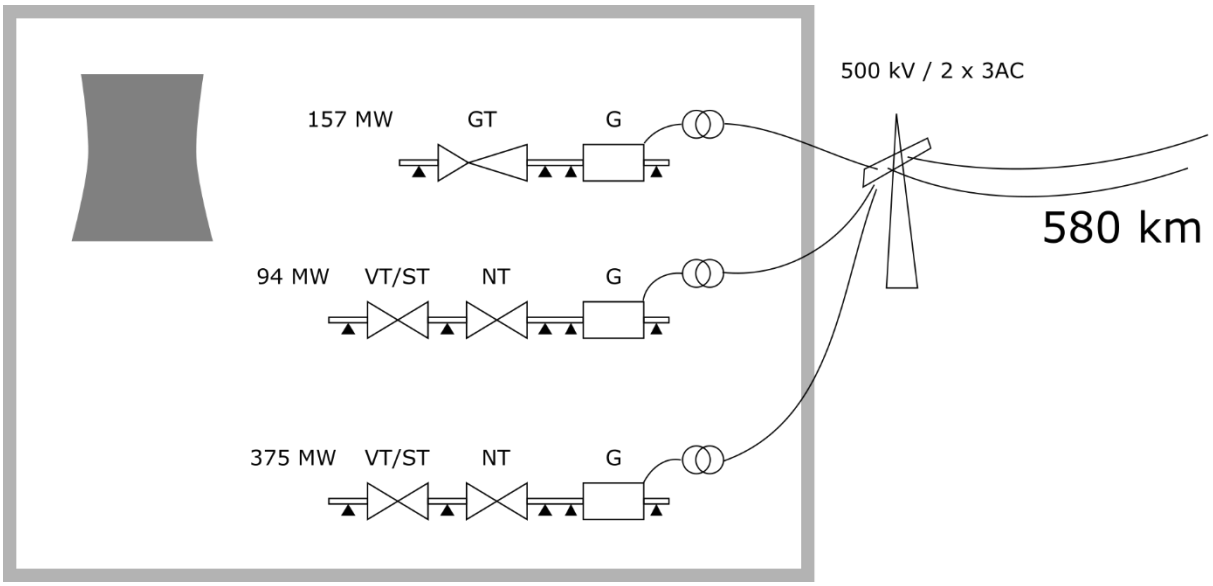


*Fig. 4.1 Power plant overview.*

The plant with a total installed capacity of more than 600 MW consists of three turbine-generator units. The first two units with a total installed power about 250 MW are parts of a combined-cycle unit (157

MW gas turbine + 94 MW steam turbine using the waste heat from the gas turbine). The third unit is a coal-fired unit with a 375 MW steam turbine. These three units are connected to the interconnected power grid via a relatively long line of 580 km.
The extensive length of this line presents a good initial condition for subsynchronous resonance effects. This fact was already known during the planning phase of the power plant, and therefore the requirement for on-line monitoring of torsional vibrations of the rotors was included in the conditions for approval for operation. Thanks to this, conditions were created under which an online torsional vibration monitoring system could be installed in the power plant, in which the author of this thesis also participated.

### 4.1.1 Subsynchronous resonance and forced vibration

One day between 21:33 and 21:48 local time, the 375 MW machine showed a significant increase in the amplitude of torsional vibrations at the first natural torsional frequency of 18.9 Hz. Given the shape of the amplitude increase at the beginning of the event and the amplitude decrease at the end of the event, see Fig. 4.2, and given the fact that there was no increase at any other natural frequency or twice the mains frequency, see Fig. 4.4, it can be assumed that the oscillation was caused by the presence of the relevant oscillating component in the voltage in the electricity network.

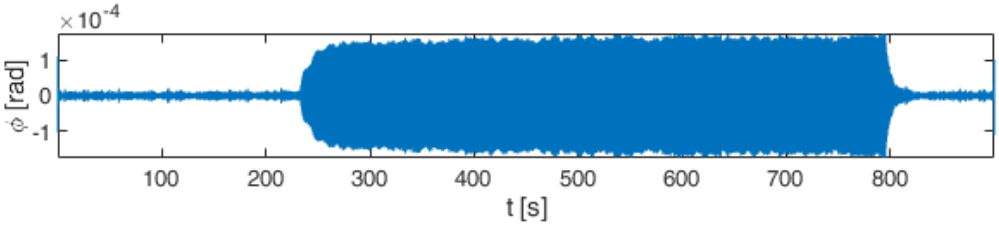


*Fig. 4.2 The overall view at the resonance event – band pass filtered vibration at the torsional natural frequency.*

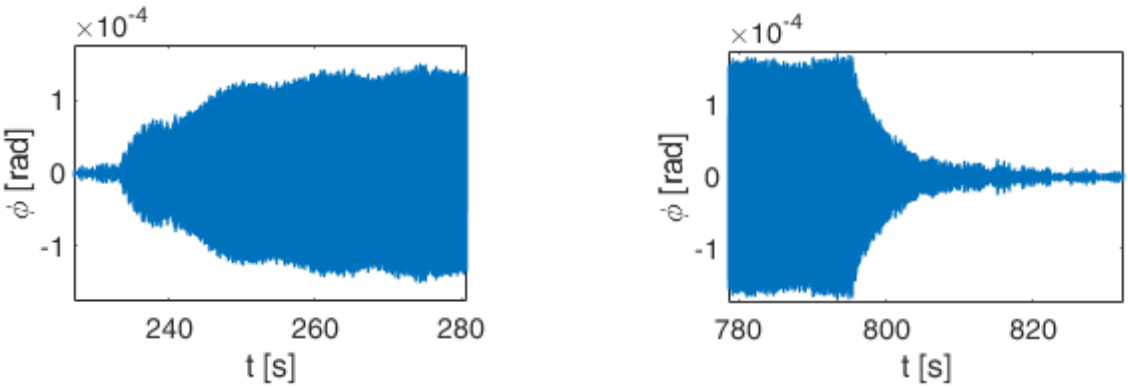


*Fig. 4.3 Detailed view at the initial and the terminal phase of the resonance event.*

In the following figure, the short-time Fourier transform spectrogram can be seen. This proves the timely localized nature of the resonance event. In addition, the frequency localization is also clearly visible. The amplitude increase at the frequency of 34 Hz corresponds to the second torsional natural frequency. This proves to be excited permanently and independently on the first torsional natural frequency.

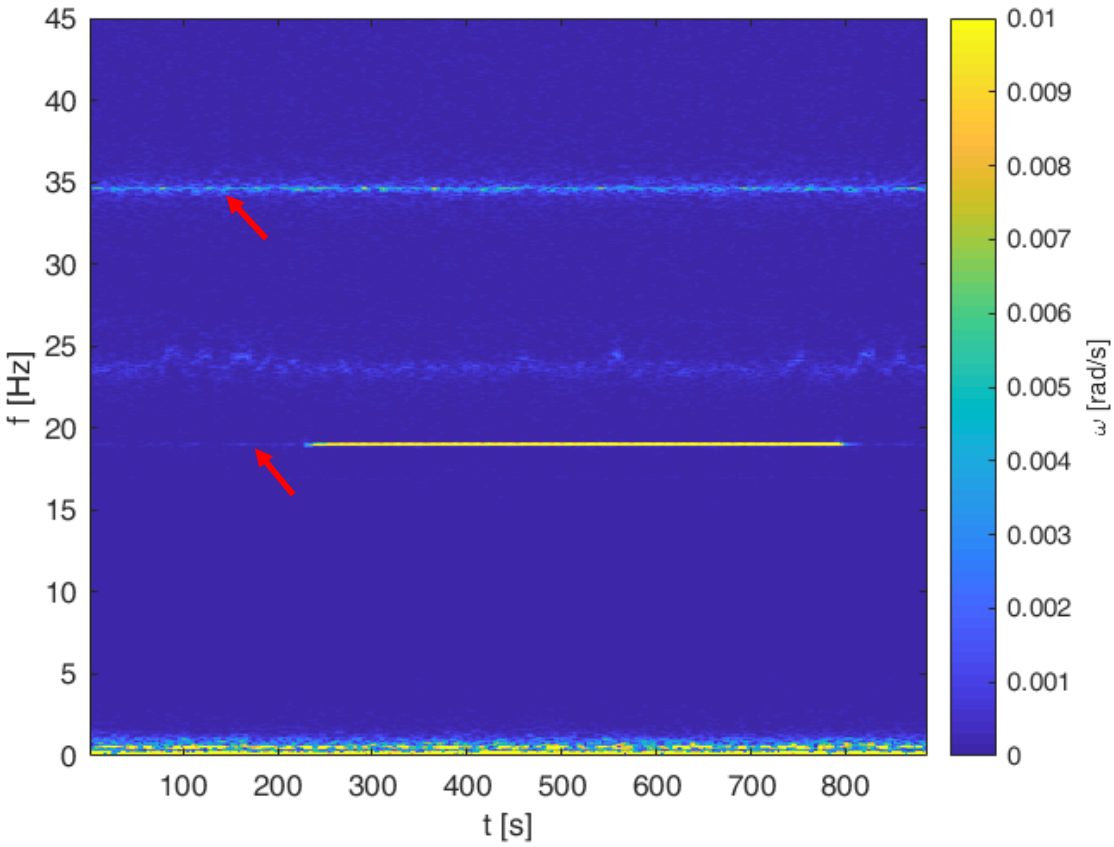


*Fig. 4.4 The same resonance event in terms of a short-time Fourier transform spectrogram.*

An extremely interesting observation was made by analysing the vibration of a nearby unit. Although this nearby unit has a different first torsional natural frequency of 20,3 Hz, the forced vibration at 19 Hz can be detected at this unit as well.

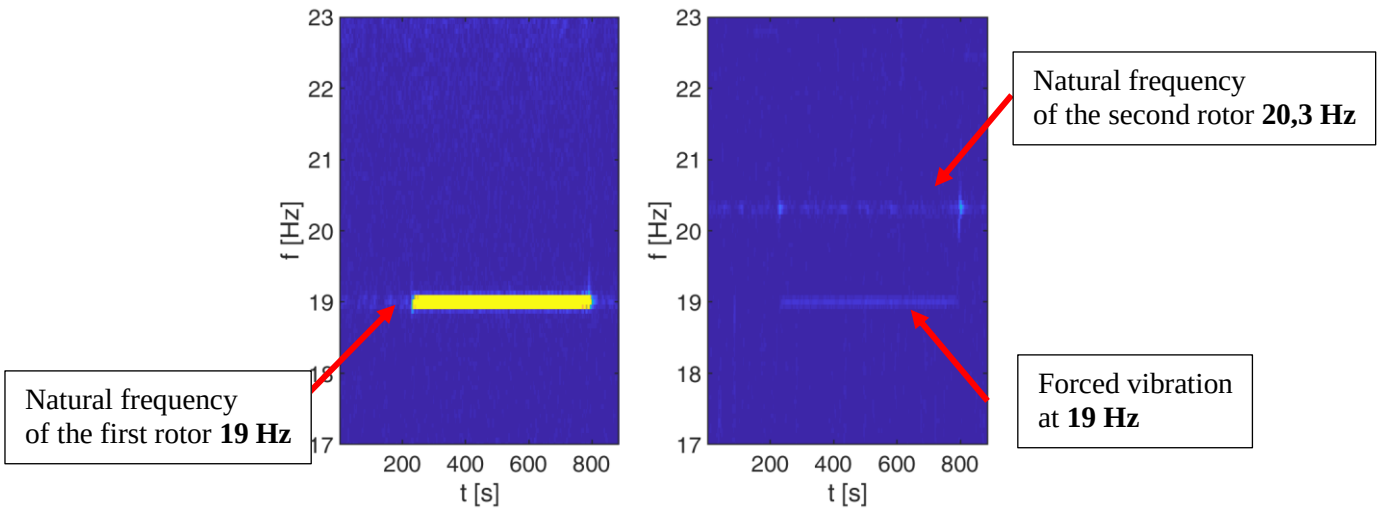


*Fig. 4.5 Comparison of the forced vibration at two different units – resonance occurs when the excitation frequency matches the natural frequency.*

We can conclude, there has been an oscillation component in the grid at 19 Hz, but only one of the units responded with a significant increase at this frequency as it was close to its natural frequency. For the

second unit, there is a larger gap between the grid frequency and the natural frequency and thus the resultant amplitude is much lower – no resonance occurs.

### 4.1.2 Subsynchronous resonance and beat phenomenon

Another example of subsynchronous resonance has been detected on 9.12.2018. Here, another highly interesting nature of the power grid oscillation can be observed. Figure 4.6 shows the time signal of the torsional vibration filtered out at the first torsional natural frequency as well as the corresponding short-time Fourier spectrogram.

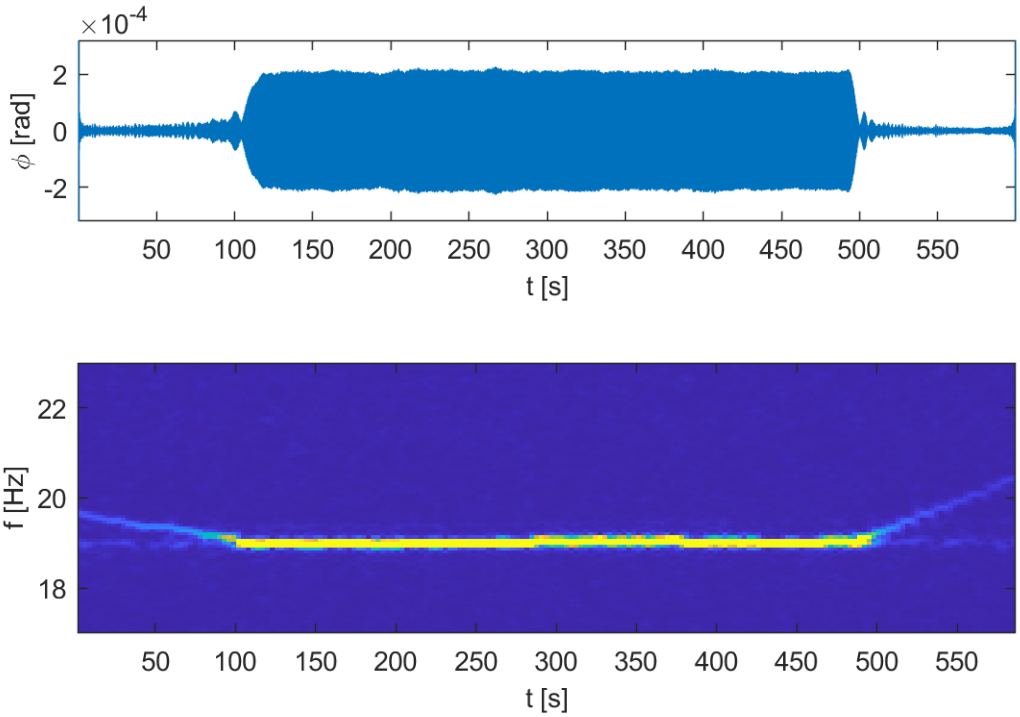


*Fig. 4.6 Subsynchronous resonance detected on the 09.12.2018.*

Contrary to the example in Fig. 4.4, in this case we can see a frequency component in the background which starts at the frequency of 20 Hz, then gradually decreases until it reaches the frequency 19 Hz. It keeps resting at this frequency for about 400 s and, afterwards, gradually increases back to higher frequencies. While the component rests at 19 Hz, torsional vibration gets excited significantly as this is the torsional natural frequency. The resonance takes place just like in the previous example.
Amazingly, we can also observe the beat phenomenon is this example. As the excitation frequency is close to but different from the torsional natural frequency at the beginning and at the end of the resonance (i.e. at times just before 100 s and just after 500 s), the forced response oscillation and the natural oscillation superimpose to each other and create beats. As the frequency difference is changing, the beat frequency is also changing which is demonstrated in Fig. 4.7. The left side of the figure shows a detailed view of the signal in Fig. 4.6 – at the time when the forcing oscillation leaves the torsional natural frequency and the beats phenomenon occurs. The right side of the figure proves that the frequency of the beats (blue line) matches well with the difference between the forced response oscillation frequency and the torsional vibration frequency. It is true that with an increasing difference between these two frequencies the beat frequency increases; on the other side, the system moves further away from resonance and thus the amplitude of the beats decreases.

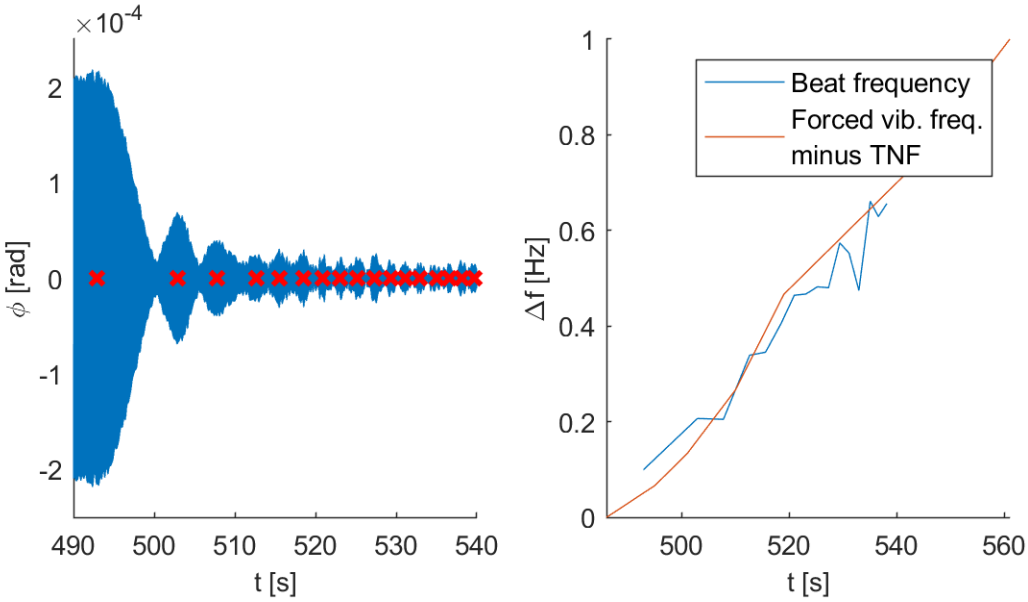


*Fig. 4.7 To the beat phenomenon analysis.*

### 4.1.3 Forced vibration components in all-day spectrograms

In this chapter we further investigate the nature of the vibration components which are clearly seen in the background of the short-time Fourier transform spectrograms of the torsional vibration signals. As there is no physical reason for this vibration to be mechanically induced (does not stick to natural torsional frequencies), the only possible explanation is they are a forced vibration excited by an electrical oscillations present in the power grid. Although this forced oscillation is not of great direct importance to the excessive oscillation of turbine-generator rotors, it is nevertheless useful to pay attention to it. It turns out, the frequency of this oscillation changes over time. These changes are apparently the result of a larger number of changes in the electricity network and its reconfiguration. And when the frequencies of these electrical oscillations change, intersection of the rotor natural frequencies may happen. At this point resonance and thus increased torsional vibration can occur.

To analyse this forced vibration we will use all-day short-time Fourier transform spectrograms of the instantaneous angular speed signals. First we show two all-day spectrograms for the same day for the two 385 MW and 97 MW units, according to the power plant overview in Fig. 4.1. A special attention should be paid for the forced vibration component highlighted with the dotted line. It can be seen this is a common vibration component for both machines. As these machines are of different type and thus having different natural vibration frequencies, the only explanation is there is such an oscillation in the power grid that causes this forced vibration response.

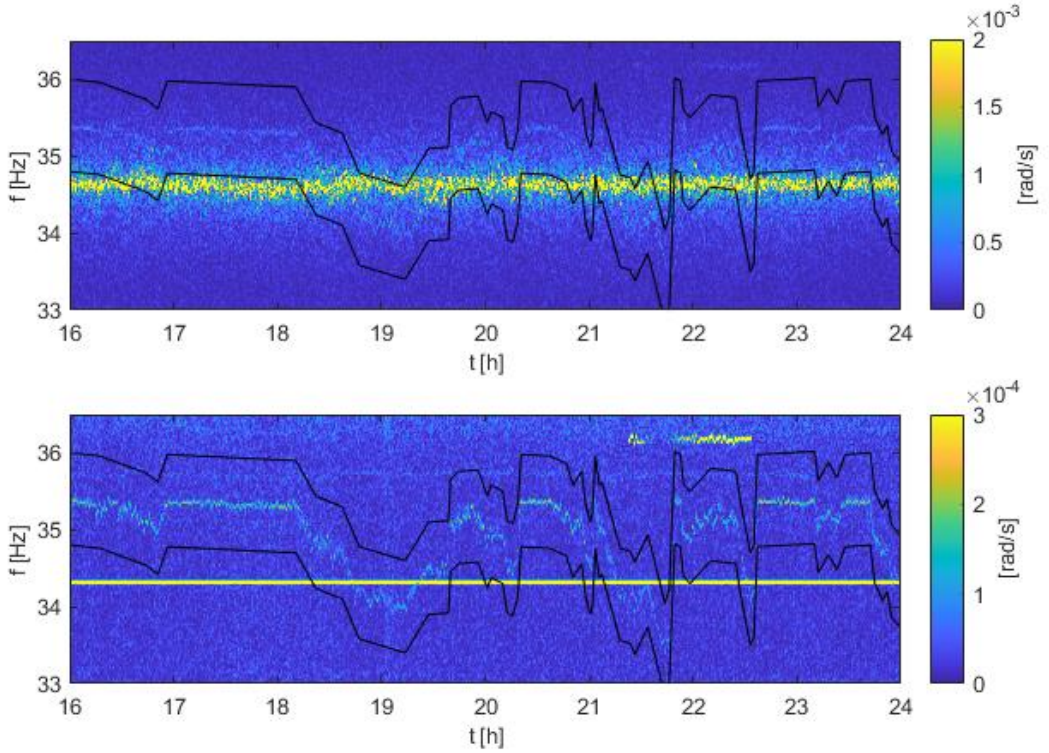


***Fig. 4.8 Forced vibration component tracking on the 385 MW machine (upper spectrogram) and the 94 MW machine (lower spectrogram).***

The forced vibration component present in the spectrograms in Fig. 4.8 does not intercept any of the torsional vibration components of the two machines, thus the vibration amplitude remains neglible. Recall, that the purpose of Fig. 4.8 was to demonstrate the existence of forced vibration excited by oscillation originating from the power grid.

A different situation can be seen in Fig. 4.9. Here we see similar forced vibration components, but this time these components intercept the second torsional natural frequency of the machine. Here, it can clearly be seen that while crossing the natural vibration frequency, resonance takes place and the vibration amplitude becomes significantly amplified. The upper and lower spectrogram in Fig. 4.9 shows exactly the same spectrogram, but in the lower one the forced vibration components are highlighted and also the resonance amplitude increase at the intersection with the torsional natural frequency („2nd TNF“) of 37 Hz is depicted with the circles.

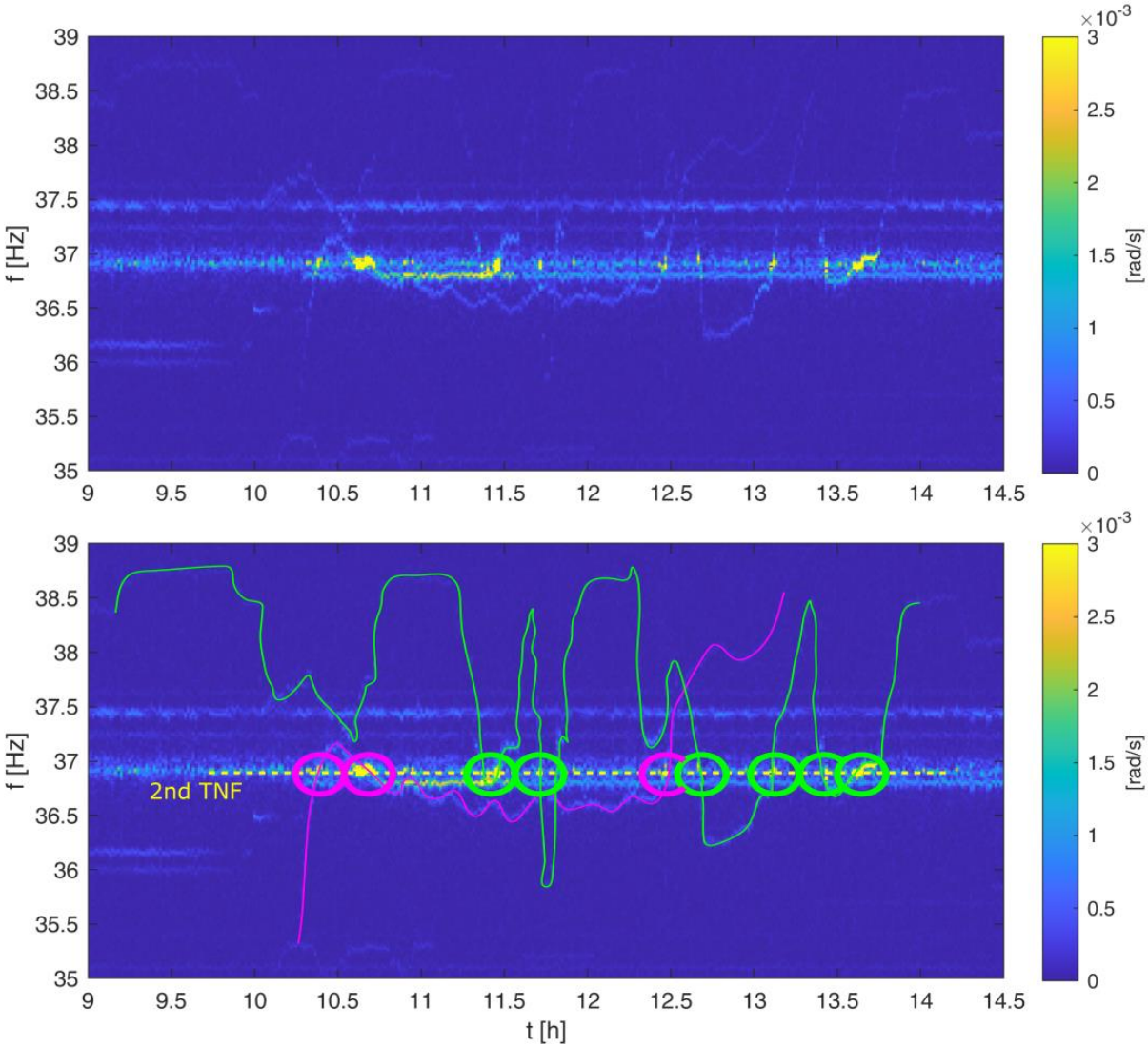


*Fig. 4.9 Forced vibration component trancking on the 94 MW machine from 26.6.2019.*

## 4.2 Torsional vibration response to air-gap torque disturbances

In this chapter, we will pay attention to another type of electro-mechanical interaction of the turbine-generator and the power grid, namely the one in which the initial impulse is a change in the operating point of the grid or synchronous machine. Such events are associated with a sudden change in the load angle of the machine, which leads to a sudden change in the air-gap torque and, eventually, the excitation of torsional vibration of the machine.

### 4.2.1 Three-phase generator terminal short-circuit torsional response diagnostics on RD

The first case study in this sub-chapter will concern the torsional vibration evaluation of the turbine-generator rotor of a 375 MW unit of a coal-fired power plant during a three-phase short circuit at the generator terminals. This is the turbine-generator of the same power plant that we have already discussed in Chapter 4.1 regarding subsynchronous resonance analysis.

The event occurred on during a short-circuit tests on a very high voltage line, near the block transformer. During the tests, the generator was disconnected from the network, however, at nominal speed and energized at nominal voltage (no-load operation). In the event of a short circuit, an extremely strong discharge occurred, resulting in the formation of a cloud of ionised air. By an unfortunate coincidence, according to witnesses, the ionised air reached the 40 m away outlets from the generator, where it caused a secondary short-circuit on the generator disconnector.

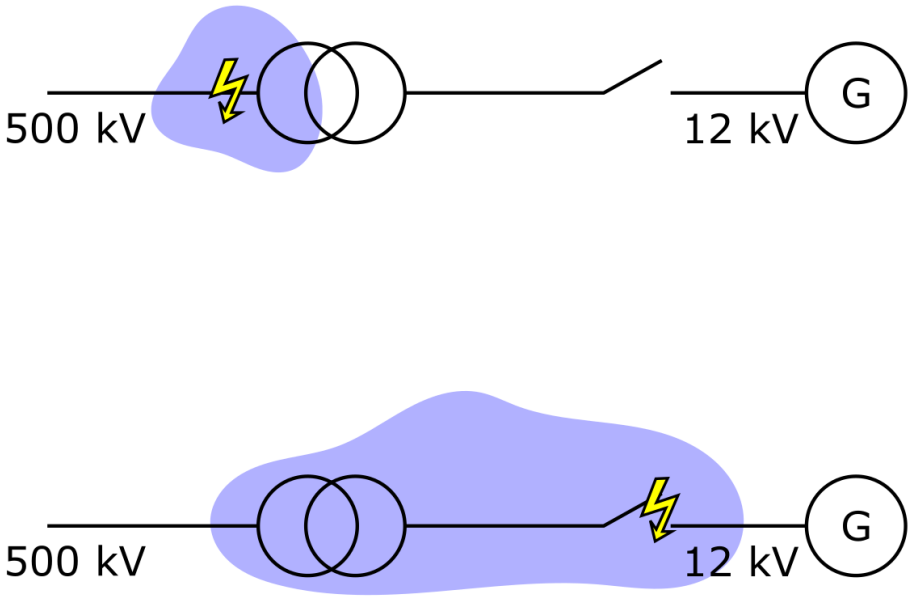


*Fig. 4.10 The upper picture shows the situation just after short-circuit on the very high voltage side of the transformer. The lower picture shows the situation few seconds later, as the cloud of ionised air reached the generator terminal.*

At the first moment, in accordance with the laws of physics, there was a sharp increase in the braking electric torque and the machine was slowed down. The turbine speed controller responded to this braking and opened the valves. However, about a second later, a black-out occurred from the short-circuit and the turbine was automatically tripped.
Figure 4.11 shows a simplified rotor model. Since the rotor is composed of 3 bodies, the first 2 natural frequencies can be expected as subsynchronous, i.e. less than 50 Hz, and the others supersynchronous (see Chapter 1). Indeed, the values of the first four rotor torsional natural frequencies provided by the operator are 18.83 Hz, 34.14 Hz, 116.59 Hz and 128.71 Hz.

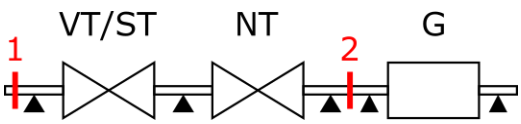


*Fig. 4.11 Schematic of the turbine-generator with marked measuring planes.*

At the same time, the position of two measuring planes is marked in the picture. One measuring plane was at the free end of the rotor where the standard machine speed measurement gear is located. The

second measuring plane is located between the low-pressure part of the turbine and the generator and is formed by a zebra-tape glued to an exposed piece of the rotor circumference.
For subsynchronous self-oscillations, the torsional deformation mainly takes place on relatively flexible pins, while the individual rotor bodies behave as rigid bodies. The approximate shape of the torsional natural shapes is shown in Fig 4.12.

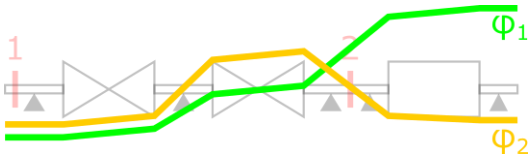


*Fig. 4.12 Torsional deflection for the first and second torsional natural shape.*

The first eigenshape (green line) can be expected to be detectable on both measurement planes, with greater amplitude at sensor 1, which is further from the node of this oscillation shape, and less at sensor 2, which is closer to the node. The second eigenshape (orange line) should be well detectable at sensor 1, but a very small amplitude can be expected at sensor 2, as this sensor lies close to the node of this oscillation. The next two figures 4.13 and 4.14 confirm these expectations. Figure 4.13 shows the instantaneous angular speed of the rotor at measurement locations 1 and 2. In addition to oscillations associated with torsional vibrations, the signals show an exponential decrease in speed caused by the fact that the machine was shut down immediately after the event.

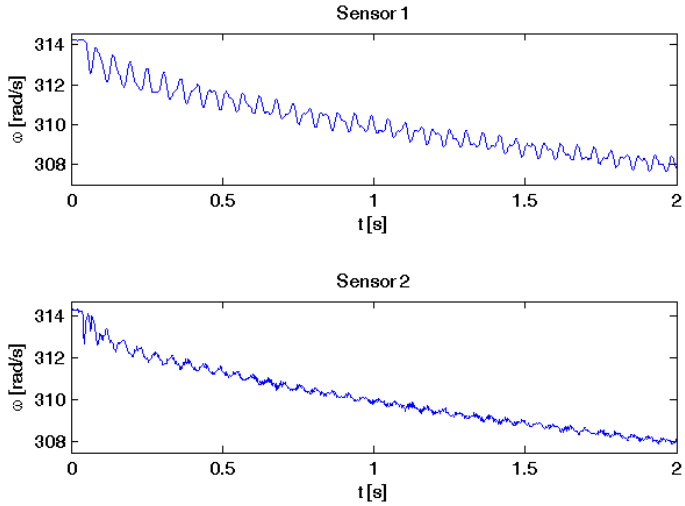


*Fig. 4.13 Instantaneous angular speed signals at sensors 1 and 2.*

The Fourier frequency-amplitude spectra of the instantaneous angular speed signals from Fig. 4.13 are shown in Fig. 4.14. It can be seen that while both first two natural frequencies are clearly excited on sensor 1, only the 1st torsional natural frequency is excited on sensor 2.
The values of the first two torsional natural frequencies of the rotor read from the spectrum are 18,9 Hz and 34,9 Hz. The following table shows a comparison of model natural torsional frequencies provided by the manufacturer and those determined based on measurements.

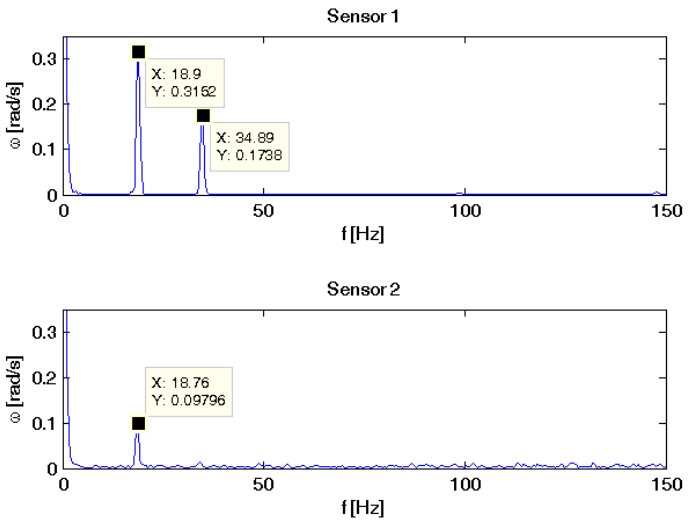


*Fig. 4.14 Amplitude frequency spectra of instantaneous angular speed signals.*

| | Model | Measurement | Error |
|---|---|---|---|
| 1st natural frequency | 18,8 Hz | 18,9 Hz | 0,5 % |
| 2nd natural frequency | 34,1 Hz | 34,9 Hz | 2,3 % |

*Tab. 4.1 Comparison of modelled and measured natural torsional frequencies.*

The amplitude of oscillations at the first natural frequency of sensor 1 is 0.3152 rad/s, which corresponds to 2.64 mrad. For sensor 2, the amplitude is 0.0980 rad/s, which corresponds to 0.82 mrad. The ratio of these two amplitudes is 3.2.
Finally, the course of the static twist of the rotor between measurement planes 1 and 2 will be shown. To obtain this signal, the instantaneous angular speed signals were first integrated, thereby obtaining the courses of the instantaneous angular position of the rotor, and these signals were subsequently subtracted from each other, thus obtaining the twist between the measurement planes.

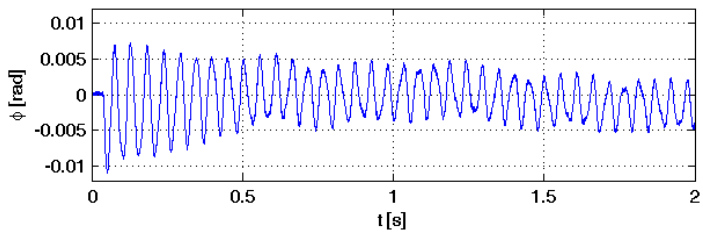


*Fig. 4.15 Rotor twist during the event.*

### 4.2.2 Evaluation of rotor torsional vibration and static torsion

Another case study will concern the evaluation of torsional vibrations of the turbine-generator rotor of a 250 MW unit of a coal-fired power plant. During torsional vibration monitoring, an event was captured during which the machine was tripped from full power. The event occurred due to exceeding the limit temperature of the stator winding. The sudden unloading of the rotor had the effect of a strong torsional excitation, which resulted in the excitation of the rotor's torsional natural frequencies.
Figure 4.16 shows a diagram of the turbine-generator with marked measurement planes of the TVMS system. In the plane marked with number 1, the existing gear with 80 teeth and a hall probe was used, in plane 2 a paper zebra tape with 137 marks was installed in combination with an optical sensor.

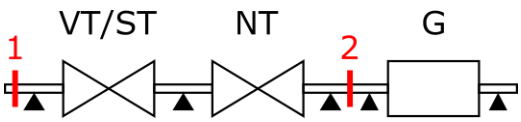


*Fig. 4.16 Schematic of the turbine-generator with marked measuring planes.*

First, we evaluate how the sudden unloading of the turbine-generator affects the value of the static torque between planes 1 and 2. When the turbine-generator is in operation and loaded, i.e. there is a constant transfer of energy from the turbine to the generator, the rotor transmits torque. The transmission of this torque is realized by elastic forces in the material of the rotor arising during its torsional deformation. Torsional deformation is smaller on the individual parts of the turbine-generator and larger on the pins between them, since the pins generally have a smaller radius and therefore less torsional stiffness. An approximate course of torque and torsional deflection along the axis of the rotor is shown in Fig 4.17.

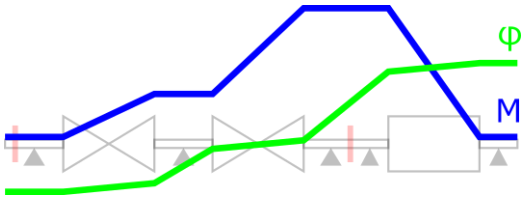


*Fig. 4.17 Approximate torque and torsional deflection course along the rotor related to the first torsional natural shape.*

From the measured data, information about the sudden change of the torsional twist can be obtained from the course of the detection times on the 1st mark of the encoder. A change in static twist manifests itself as a shift of the detection times of all encoder marks within one revolution by the same interval forward (if the twist change in the given plane was in the direction of rotation) or backward (if the twist change was in the opposite direction to rotation). The reason for choosing the 1st mark is that the detection time at the 1st mark is least affected by the instantaneous angular speed changes.
The course of detection times on the 1st mark of the encoders in planes 1 and 2 is shown in Fig. 4.18.

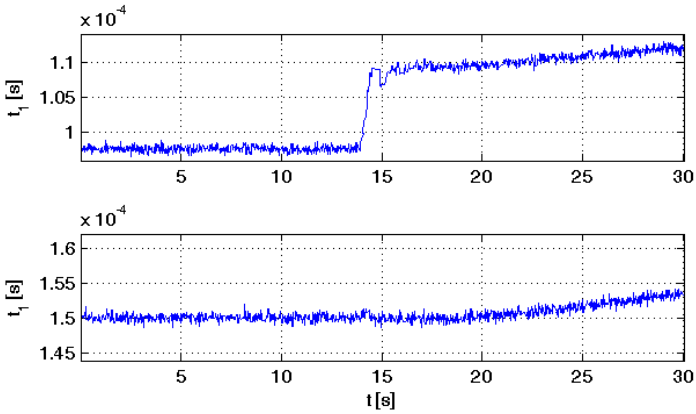


*Fig. 4.18 Detection time of the first encoder marker at the measurement planes 1 and 2.*

It can be clearly seen from the figure that the detection time of the 1st marker in plane 1 will step-up by $1{,}1 \cdot 10^{-5}$ s. No step change appears in plane 2, which is consistent with the fact that the phase marker was installed on plane 2 to synchronize the measurements. Therefore, the difference of the change in the detection times of the first stripe in planes 1 and 2 during before and after the event is equal to $1{,}1 \cdot 10^{-5}$ s. This means a angle value of $3{,}5 \cdot 10^{-3}$ rad at the nominal speed of $3000\,rpm$. This value represents the change in static twist between planes 1 and 2 during the event. The course of static torsion between planes 1 and 2 is shown in Fig. 4.19.

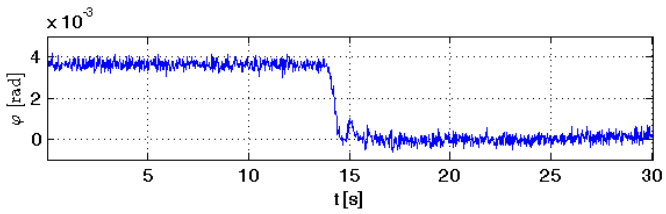


*Fig. 4.19 Rotor twist during the event.*

The change in torque between planes 1 and 2 during this event can also be computed. From the change in active power of 250 MW at 3000 rpm, the change in torque is 796 kNm. The comparison of the static twist and the torque change gives the turbine designer the opportunity to validate their calculations. This can also be considered a useful output of the analysis presented in this thesis.

### 4.2.3 Evaluation of instantaneous angular speed and generator terminal voltage signals of a 250 MW turbine-generator

The next case study will concern the same turbine-generator as in the previous subsection. In this case, however, it will be an evaluation of rotor torsional vibration during a significant event in the power grid. Due to operations at a nearby distribution station, a transient event occurred in the power grid, which caused a significant fluctuation of the performance of the machine.
During the monitoring of torsional vibration on this turbine-generator, the terminal voltage on one phase of the generator was also measured. The aim was to examine the interaction of transient events in the power grid and the relevant mechanical torsional response of the rotor. Thanks to this, it is possible to better show the connection between electrical and mechanical responses during the event.

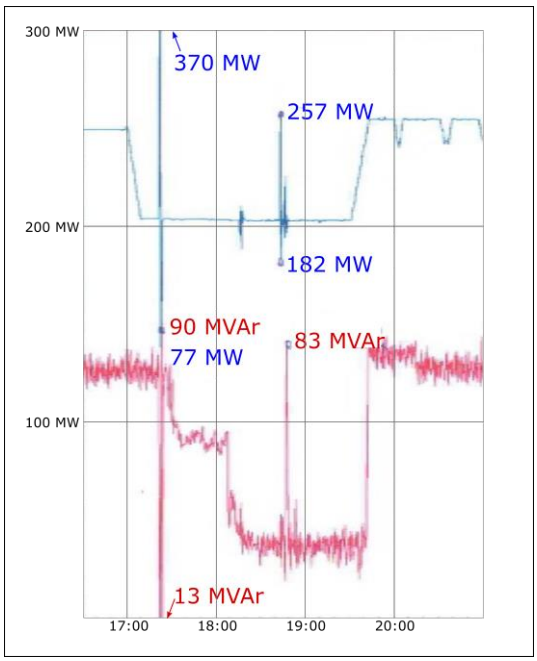


*Fig. 4.20 Active and reactive power waveforms. The event in question occurs at 17:23.*

Figure 4.20 shows the active and reactive power curves. The event in question occurred at 17:23 according to the horizontal axis. The graphs provide an idea of the machine's power state at the time of the event. It can be seen that before this event the machine was operating at a steady active power of 204 MW and a reactive power of 72 MVAr. During the event, the active power first fluctuated up to a maximum value of 370 MW, followed by a swing to the opposite side up to a minimum value of 77 MW, and then the machine re-stabilized at the original value of 204 MW. Reactive power also shows a

transient event with an initial decrease to 13 MVAr followed by an increase to 90 MVAr, finally settling down to the initial value. The subsequent reduction of reactive power around 17:30 is no longer directly related to the event. Note that the vertical axis belongs only to active power. The graphs were provided by the plant operator.
We will now analyse how this sudden active power increase affects the torsional response of the rotor. From the measured detection times, the instantaneous angular speed was first evaluated according to the algorithm described in Chapter 3. The course of the angular speed is shown in Fig. 4.21.

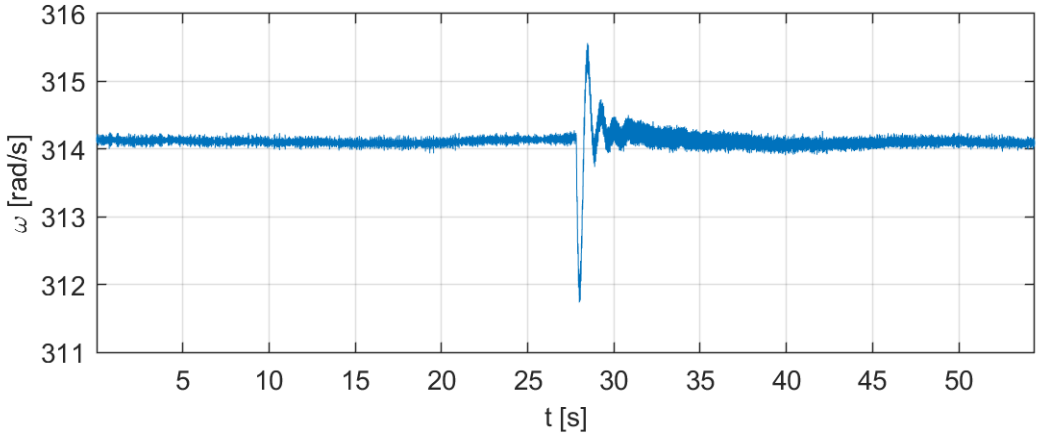


*Fig. 4.21 Evaluated instantaneous angular speed.*

The amplitude spectrogram of the short-time Fourier transform of the instantaneous angular speed signal in the vicinity of the event is shown in Fig. 4.22. In the spectrogram, the excitation of the first and second torsional natural frequency of the rotor is visible at 20,3 Hz and 39,3 Hz. It can be seen that the first of the natural torsional frequencies is more excited. This corresponds with the intuitive idea that a step change in the load at one end of the rotor best oscillates the rotor in the sense of the first natural shape, i.e. when the opposite ends of the rotor swing against each other.

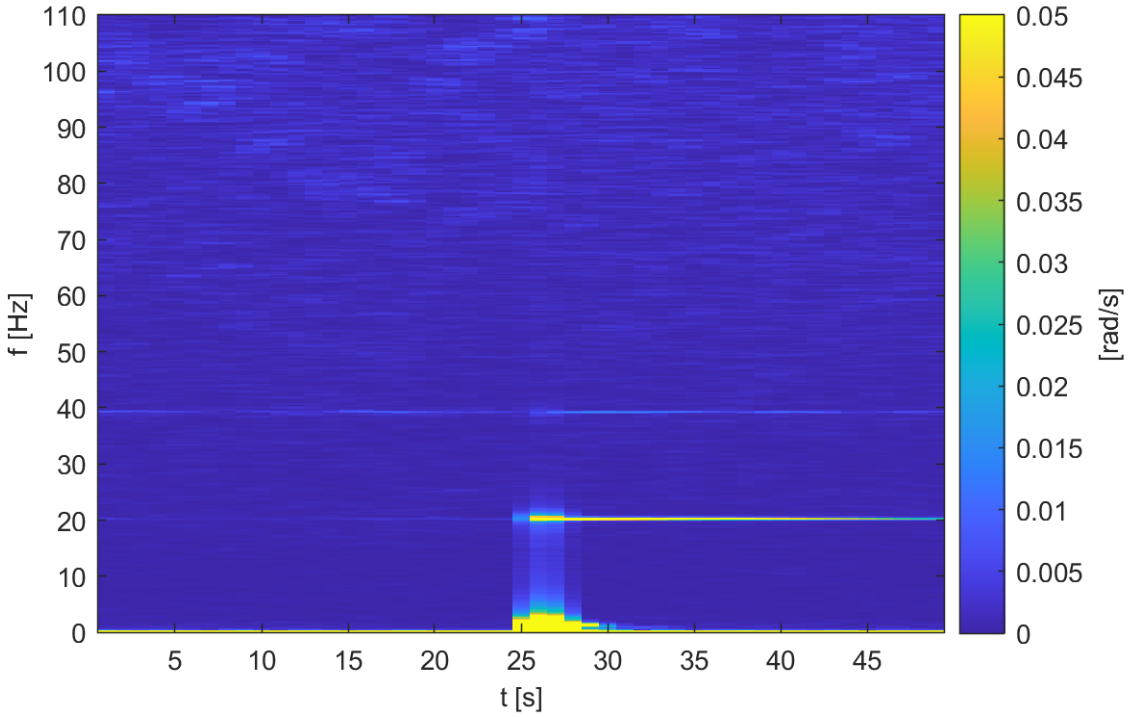


*Fig. 4.22 Instantaneous angular speed Fourier spectrogram.*

The detailed course of the oscillation at the first torsional natural frequency is shown in Fig. 4.23. This signal was obtained by band-pass filtration of the signal from Fig. 4.21. An exemplary oscillatory impulse response can be seen with a steep rising excitation and an exponential decay lasting several tens of seconds.

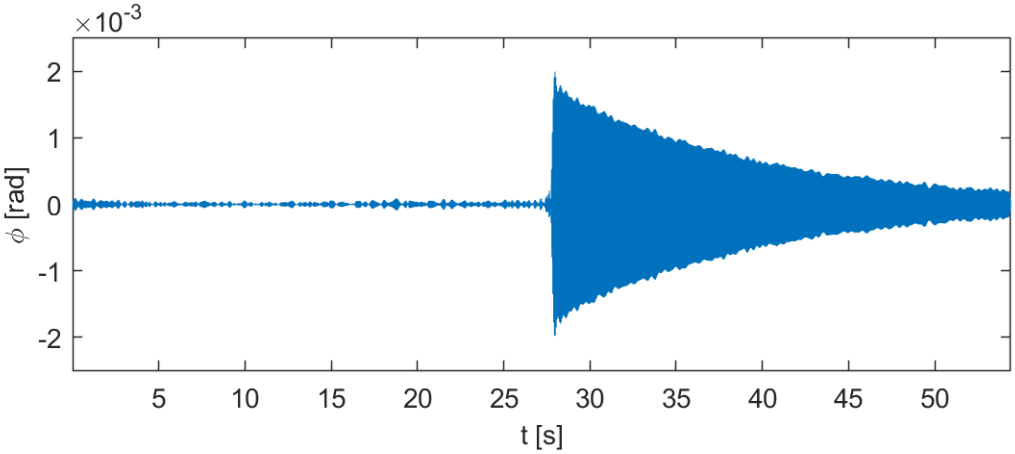


*Fig. 4.23 Torsional vibration amplitude at the 1st natural frequency.*

In the previous discussion we analysed the pure mechanical response of the turbine-generator rotor to the event. In the following we discuss the linkage with the electrical side of the problem. This can be achieved with the measured terminal voltage $V_g$ signal. Unfortunately, this signal was measured only on one phase, so our conclusions will only be approximative as we will not be able to reconstruct the true angles of the voltage phasors but we will assume a quasi-stationary states with symmetrical phasors. For the analysis to be reliable we should ideally have measured both voltage and currents of all three phases. However, the analysis still enables us to get a deeper understanding of what has happened during the event.

The measured voltage signal is a harmonic signal. Based on a hypothetical reference harmonic wave with the frequency of 50 Hz we can obtain the actual voltage phasor with a definite magnitude and phase in every period of the reference wave. The sampling frequency is 1613 Hz which yields slightly more than 32 samples per one period of the reference wave.

The course of the $V_g$ phasor magnitude is shown in Fig. 4.24. It can be seen that the amplitude changes only very slightly during the event at 27 s, and therefore we will consider the $V_g$ phasor magnitude as constant in the subsequent simplified description of the event.

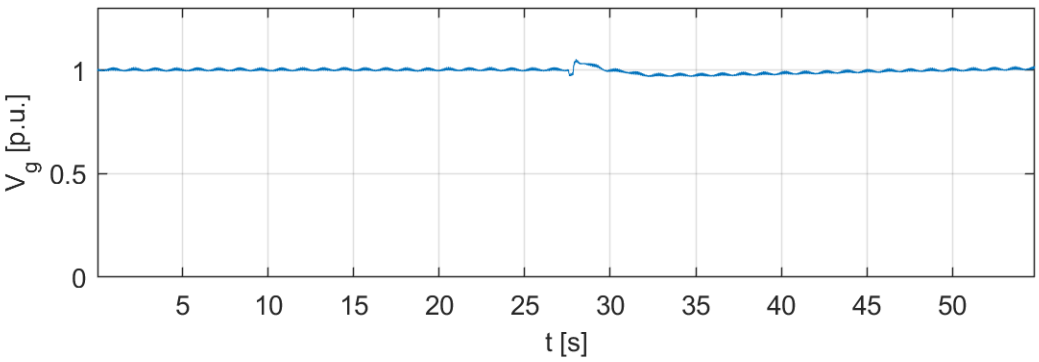


*Fig. 4.24 Terminal voltage phasor magnitude.*

The course of the $V_g$ phasor angle is shown in Fig. 4.25. It can be seen that the voltage phasor angle decreases over time, which is due to the fact that the instantaneous rotation frequency is less than 50 Hz

for most of the length of the monitored section. At about 27 s, the manifestation of the event is visible. This event manifests itself as a sudden drop followed by a dynamic transient response.

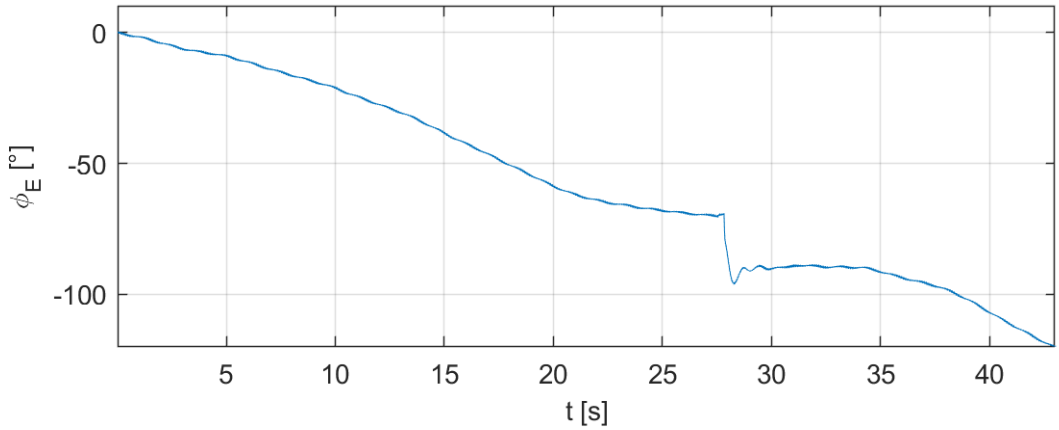


*Fig. 4.25 Terminal voltage phasor angle.*

A quantity tightly related to the terminal voltage phasor angle is the rotor angle with respect to a reference frame rotating with a constant frequency of 50 Hz. This quantity can be evaluated from the instantaneous angular speed signal by first subtracting the reference rotation speed of $2\pi * 50\ [rad/s]$ and then integrating it to change from speed quantity to angular quantity. Figure 4.26 shows the course of the rotor angle computed that way. It is not surprising that this quantity drops sharply at the first moment of the event, as this is related to the fact that the velocity drops. Similar to the terminal voltage phasor angle, the whole signal is decreasing because the rotation velocity was slightly below 3000 rpm.

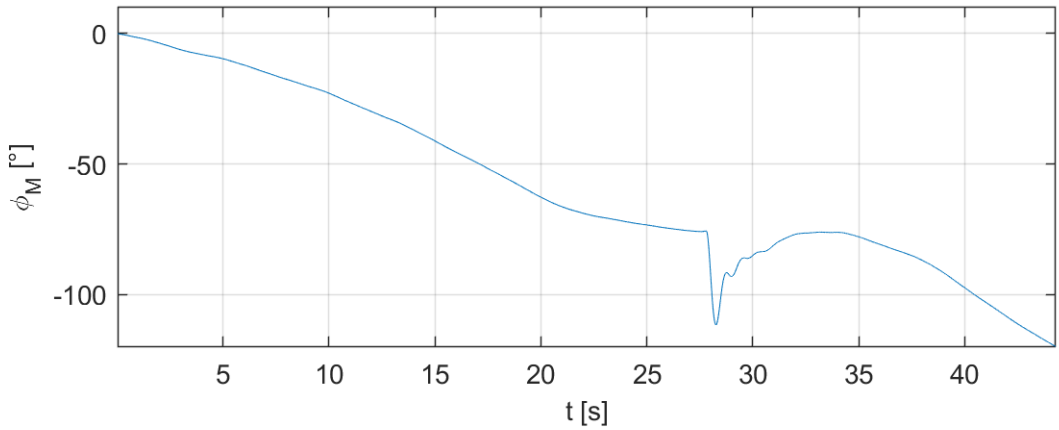


*Fig. 4.26 Rotor angle with respect to a reference frame rotating with a constant frequency of 50 Hz.*

At this moment we have evaluated the course of the voltage phasor angle and also the course of the rotation angle of the rotor relative to the rotating reference system. By subtracting these two values the course of the load angle change can be obtained. This quantity is shown in the following figure. The most important thing for us will be the size of the first swing of the load angle just after the event. According to the graph this value is $\delta \doteq 8°$.

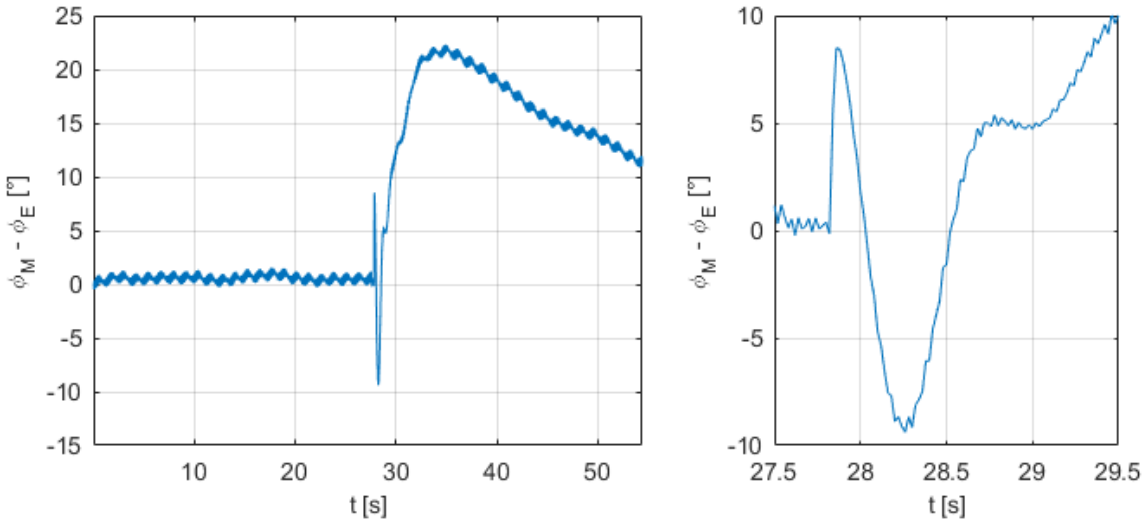


*Fig. 4.27 Load angle change course (for the course of the absolute value see Fig. 4.30).*

So far we have calculated the course of the load angle change but we do not know the absolute value. Furtunately, we have enough values to compute also the absolute value, yet making an approximative assumption that the voltage remains harmonic after the event.

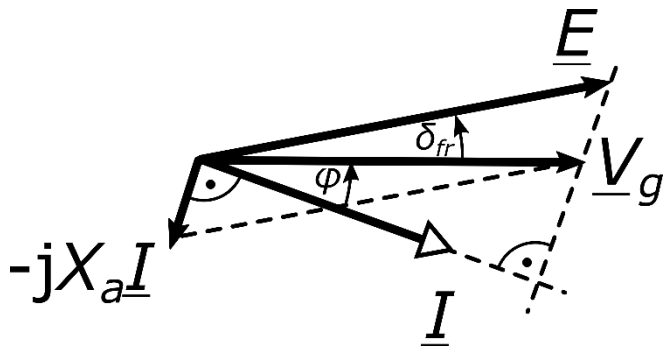


*Fig. 4.28 Phasor diagram of the generator just before the event.*

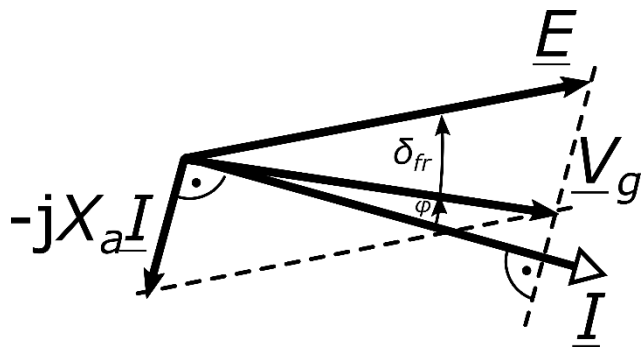


*Fig. 4.29 Phasor diagram of the generator just after the event.*

We start with a more detailed discussion of what happens during the event. The nature of the event in question is a transient event with the origin in the grid. The primary cause of the event was an abrupt rotation of the terminal voltage phasor $V_g$ by 8° as shown in Fig. 4.30. The magnitude of $V_g$ remains relatively unchanged as seen in Fig. 4.24. Next, we can assume the emf phasor $E$ to be constant during the event as its angle depends solely on the actual rotor rotation angle and its length depends on the excitation voltage and these are values that do not change on the short time scale of the event. This

assumption could be violated especially by the operation of the excitation regulator, which unfortunately we have no information about. An idealized view of the phasor diagrams before and after the event shows Fig. 4.28.
The following table summarizes the active power values obtained from Fig. 4.20 and the value of the load angle change that can be read from Fig. 4.27.

| | Before event | After event | Change |
|---|---|---|---|
| Active power [MW] | $P_1 = 204$ | $P_2 = 370$ | |
| Load angle [°] | $\delta_1 = ?$ | $\delta_2 = \delta_1 + 8$ | 8 |

***Tab. 4.2 Input data for the load angle computation.***

Based on the values from the table we are able to compute the initial load angle $\varphi_1$ just before the event- We will use the Eq. 3.35 and substitute, which relates the active powers and load angles before and after the event

$$\frac{P_2}{P_1} = \frac{sin(\delta_1 + 8)}{sin\,\delta_1},$$

where we substituted $\delta_1 + 8$ for the $\delta_2$ as the load angle after the event. This equation has an infinite number of solutions but the one that has physical sense in our case is the solution $\delta_1 \doteq 9{,}6°$. The following Fig. 4.30 shows the load angle over time, with the right image showing only a zoomed-in view of the right image. Unlike Fig. 4.27, this time the load angle curve is plotted with the correct offset 9,6° in the vertical axis.

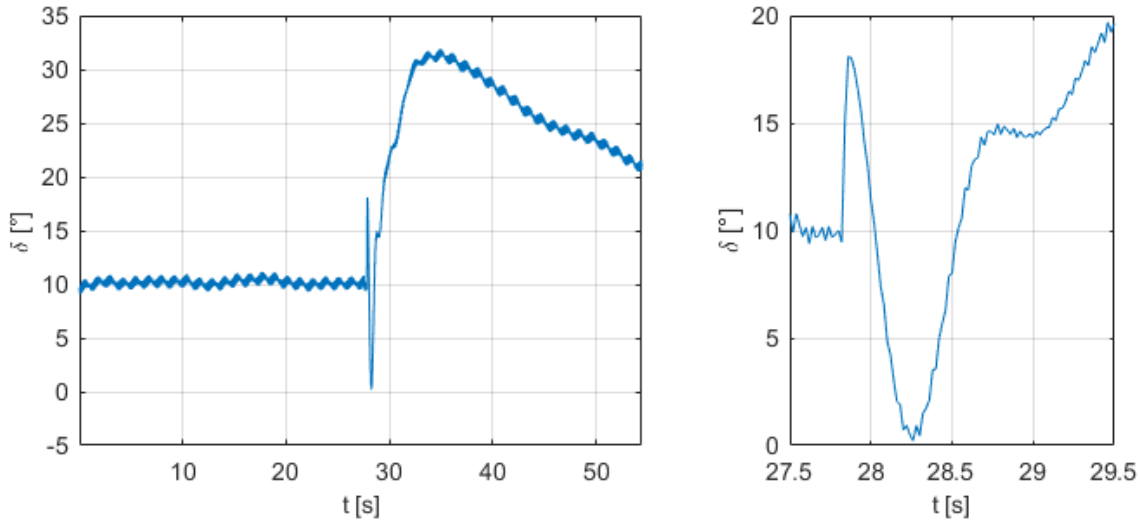


***Fig. 4.30 Load angle course offset to true values.***

To conclude our analysis, based on the available active power data and terminal voltage course we were able to perform an idealized calculation of the load angle. As seen in Fig. 4.30, the peak value of the load angle just after the event is 17,6°, which is well below the critical stability limit. Thus, the generator was well within the stable region of operation. As already said, the analysis of the load angle could have been much more reliable if both voltage and currents of all three phases was measured and if we knew whether the voltage regulator really did not intervene to change the $E$ emf phasor during the event as we assumed.

### 4.2.4 Torsional response of a 250 MW nuclear power plant unit to the outage of a nearby unit with LP turbine blade vibration excitation

The last case study will concern the evaluation of torsional vibrations of the turbine-generator rotor of a 250 MW block of a nuclear power plant during an unplanned outage of a nearby 250 MW machine. The uniqueness of this case study lies in demonstrating the fact that the blades of the low-pressure part of the turbine oscillate during significant torsional excitation of the rotor. Or alternatively, that the designed system for measuring and evaluating torsional vibrations of the rotor can also be used to monitor the oscillation of the blades of the low-pressure part of the turbine.

The mentioned unit was the first one in which the system for torsional vibration monitoring was installed. It was still an off-line form of the system, i.e. the measured detection times were stored on a hard disk and the analysis was performed only after the hard disk was taken from the power plant to the university. Even the method of measuring the detection times was more of a pilot, as paper reflective zebra tapes were used with optical sensors directly sensing the tape. No waveguides were used to allow the sensors to be placed further from the moving surface of the rotor. However, even this pilot installation provided high-quality input data for the evaluation of this torsional event.

From the measured data, the instantaneous angular speed was evaluated according to the algorithm described in Chapter 3. Its course around the event is shown in Fig. 4.31. In the course of the angular speed, the manifestation of several phenomena can be observed. What first attracts attention is the transient event started at time 68 s. The manifestation of this event is actually made up of two different effects. The first is the effect of a transient event in the speed of the machine, which is caused by a sudden change in the operating point of the machine during the event, and which practically disappears after only a few seconds. The second is the effect of excited torsional vibrations, which have a longer decay time and can be observed for several tens of seconds after the excitation of the transient event. Furthermore, in the course of the angular speed, we can observe the manifestation of system oscillations, which have a period of several tens of seconds and which are not related to the event. And finally, after the event, the creation of a new frequency in the network can be observed. This is because of the outage of the nearby 250 MW source. The new frequency gets stabilized at the new lower value after the primary control intervention, i.e. when other sources in the network that work in the primary frequency control mode compensate for the active power outage of the failed block. The new frequency in the network is about 0.1 rad/s (0.017 Hz) lower than before the outage, which agrees with the standard 3000 MW / 0.2 Hz gain of the primary regulation.

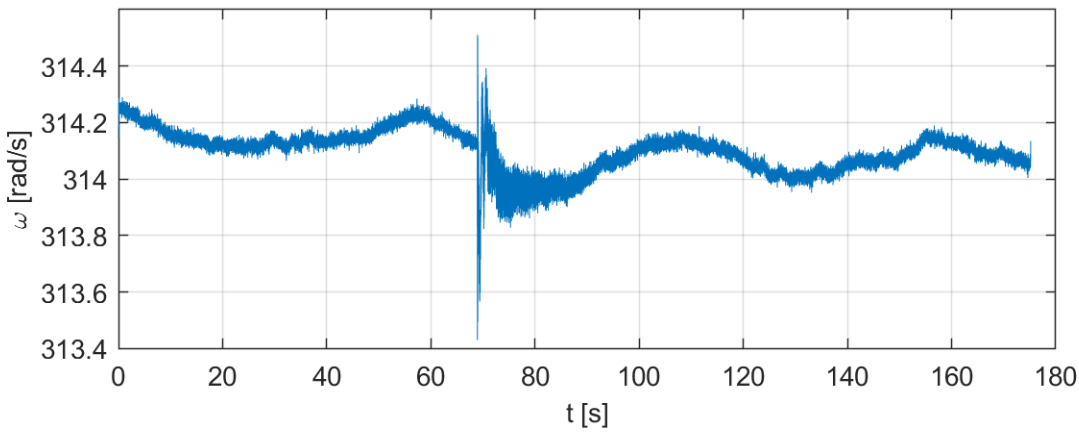


*Fig. 4.31 Evaluated instantaneous angular speed.*

From the point of view of torsional vibrations of the rotor, we are even more interested in the course of torsional oscillations. Let us recall that a step change in the electrical load of the generator acts as a step mechanical excitation of the torsional vibrations of the turbine-generator rotor. During this excitation, all frequencies are excited, however, the rotor's natural frequencies are the main components of the response. The amplitude spectrogram of the short-time Fourier transform of the instantaneous angular speed signal in the vicinity of the event is shown in Fig. 4.32. In the spectrogram, the excitation of the

first and second torsional natural frequencies of the rotor of 17.0 Hz and 28.4 Hz, as well as two higher natural torsional frequencies of 96 and 98.4 Hz, can be seen. These last two frequencies come from the interaction of the rotor and the last rotating blades of the low pressure segment. This is a very valuable proof that the blades of the low pressure segment of the turbine can be oscillated during large events in the network. These components are perceived as the most delicate part regarding the torsional vibration of the turbine-generator. There are cases where blades have been severely damaged or even torn off as a result of network events.

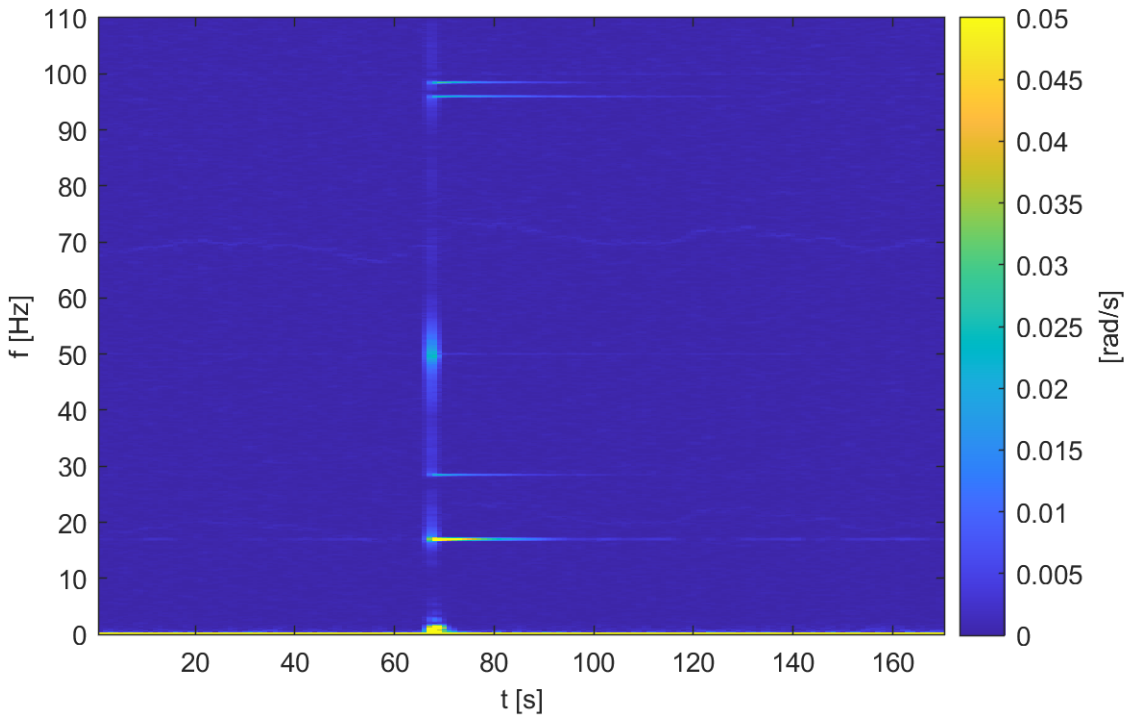


*Fig. 4.32 Instantaneous angular speed Fourier spectrogram.*

In the spectrogram, it can be seen that the first of the natural torsional frequencies is the most excited, which is also in line with the intuitive idea that a step change in the load at one end of the rotor best oscillates the rotor in the sense of the first natural shape, i.e. the oscillation of the opposite ends of the rotor against each other.

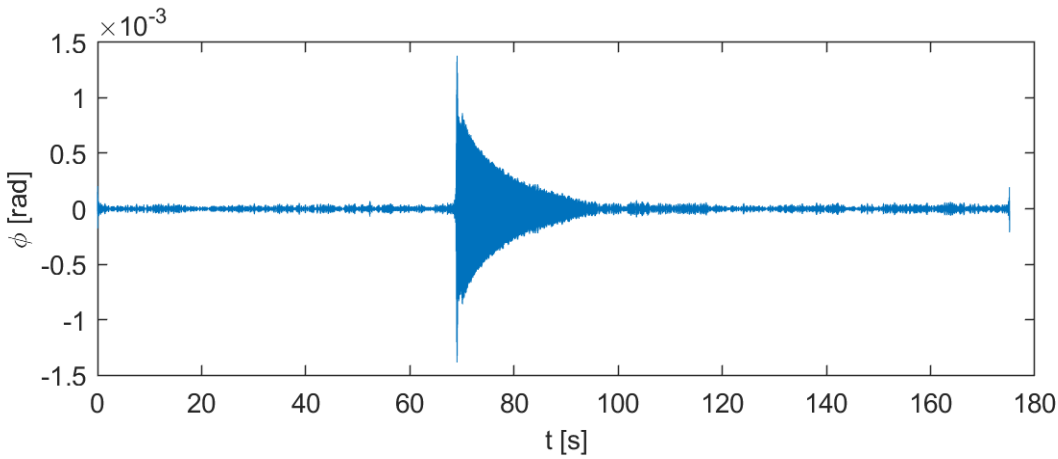


*Fig. 4.33 Forced vibration component tracking on the 94 MW machine from 26.6.2019.*

The detailed course of the oscillation at the first natural torsional frequency is shown in Fig. 4.33. An exemplary oscillatory impulse response can be seen with a jump excitation and an exponential decay lasting several tens of seconds.

# 5 Conclusions

The work was focused on the research and development of methods, software and the necessary components of the measuring chain for the purpose of analysis and subsequent monitoring of the torsional interaction of the turbine-generator with the events in the electricity network. As described, the torsional interaction is enabled by means of the air-gap torque of the generator, as this is a quantity dependent both on the motion state of the rotor as well as on the current electrical state of the generator, i.e. the network. If the torque in the air gap does not remain constant, but, for example, changes in steps or harmonically fluctuates, this is manifested by the excitation of torsional vibrations of the turbine-generator rotor. Under certain conditions, vibration excitation of sufficient amplitude may occur to exceed the material strength limits of the shaft or other rotor components, particularly the turbine blades. Permanent monitoring of torsional vibrations of turbine-generators is not yet a standard in practice. If torsional vibrations are ever evaluated, it is usually as a temporary experimental solution to answer a particular problem of the machine in question. The urgency of torsional vibration monitoring can also be reduced by the fact that torsional vibrations do not have any outwardly observable manifestations, such as the vibration of bearings or outer covers of the turbine.

In Chapter 1, the basic physical principles necessary to understand the issue were presented both from the perspective of the mechanics of torsional oscillations and from the perspective of electrical quantities. Thanks to this, a mathematical-physical model of the most important forms of torsional interaction of the turbine-generator and the power grid could be given in Chapter 2.

Chapters 3 and 4 are key from the point of view of meeting the objectives of the work. In short, Chapter 3 can be said to describe the path from the measured signal to the torsional vibration signal. The complexity of the content of this Chapter is due to the fact that the information on torsional vibration cannot be measured directly, as for example the absolute vibration of bearings, but a special measurement must be used and then a relatively complex post-processing. In the end, this is the only way to obtain sufficiently high-quality and reliable information about the torsional oscillation of the rotor. After a short introduction defining the format of the input data, a method for the precise determination of the encoder geometry is first derived. It is a theoretically derived recursive method, the parameters of which are subsequently calculated based on the properties of practical measured data. Subsequently, a method for evaluating the instantaneous angular velocity is derived. This is a quantity that contains the DC nominal speed of the machine, possibly its fluctuations and oscillating components related to torsional vibrations. By transforming the instantaneous angular velocity signal into the frequency domain, the exact frequencies and amplitudes of the torsional oscillations of the turbine-generator rotor can be determined. In addition, at the end of the third Chapter, some limitations are discussed, either those related to the proposed method or those independent of the method used, arising from the nature of measuring torsional oscillations with an incremental encoder

The last, 4th Chapter is devoted to case studies that demonstrate that the chosen methodology is suitable for practical evaluation and monitoring of the torsional interaction of the turbine-generator rotor and the power grid. The case studies are divided according to the nature of the interaction into those concerning resonance interaction and those concerning one-time transient events. Within the first group, it was possible to demonstrate the existence of oscillating components with a variable frequency originating in the electricity network, which, depending on their frequency, have the ability to torsionally oscillate the rotors of turbine-generators. Within the second group, i.e. case studies related to transient events, a number of examples were shown where a sudden change in conditions in the power grid caused transient excitation of torsional oscillations of the turbine-generator rotor.

The value of this work can be seen on several levels. On the one hand, a more systematic summary of the physical principles applied in the relatively complex phenomenon of the torsional interaction of the turbine-generator and the power grid was given. Furthermore, the methodology of analysis and monitoring of this interaction was proposed and tested on specific practical problems. Last but not least, some important features of the proposed methodology were described in greater depth, which adds to its credibility for practical use and gives the user information about its possibilities and limits.

The topic of the torsional interaction of the turbine-generator and the power grid is far from exhausted and offers a number of open problems even in the future. Starting with the extension of the mechanical

model with the model of the oscillation of the blades of the low pressure turbine stage or the creation of a model of fatigue of the rotor by torsional oscillation, ending with the creation of a kind of digital twin of the physical system, which would only use the measurement of electrical quantities, or the creation of automatic damping of torsional oscillations by appropriate regulation of the excitation current of the generator. At the same time, it can be expected that the importance of this topic and awareness of it will grow with the ongoing transformation of the electricity network, when more and more renewable sources will be connected and traditional sources will be operated outside their optimal design area.
As part of the work on this dissertation, a TVMS torsional vibration measurement system was assembled and programmed in the Labview programming language. This system has already been deployed on 14 turbine-generators with a total output of approximately 3 GW. Some of the installations even have a safety-critical status, when exceeding limit values of torsional vibrations evaluated by the system trigger a trip of the unit.

# 6 Appendices

## 6.1 Appendix 1: Incremental encoders

As was already said, the source of the input data for torsional vibration evaluation are incremental encoders. It is important to explain why standard incremental encoders are not suitable for this task. Although these sensors are widely available on the market, their design usually emphasizes other features such as position control (applications in robotics) or measuring range (applications in electrical drives). In addition, if these sensors had to be used for turbine torsional vibration evaluation they would have to be located at the end of the rotor which is usually an inaccessible location in practice, or they would have to be somehow attached to the surface of the rotor. Such realizations are not suitable for long term monitoring campaigns.

Due to the above-mentioned reasons, a new incremental encoder was designed to meet all the requirements. The design consists of a zebra tape attached to the rotor circumference at a certain location and a sensor fixed to the stator part in such a way that the sensor head points perpendicularly to the rotor surface on the tape. The term zebra tape refers to the alternating pattern which repeats all over the circumference. The pattern is originally formed by alternating black and white stripes but can also be formed by copper rectangles molded into a kapton tape as will be shown in the following text.

The purpose of the sensor is to detect the alternating pattern and convert it into an electrical signal where two signal levels correspond to the two possible zebra tape states (black/white, copper/kapton, ...)

An important requirement regarding the zebra tape is its robustness against the centrifugal force on the surface of the rotating rotor. By the substitution of the area density $\mu$ into the centrifugal force equation we get

$$F_o = \mu\omega^2 r, \qquad (A1.1)$$

where $\omega$ is the rotor angular speed, $r$ is the radius of the rotor and $F_o$ is the centrifugal force at the rotor surface. The centrifugal force must not exceed the strength of the glue attaching the zebra tape to the surface otherwise the tape will peel off.

### 6.1.1 Optical incremental encoders

The first type of the tape was a paper tape of the area density of 0,1196 $kg \cdot m^{-2}$. Unfortunately this tape suffered from a lack of mechanical robustness and from the fact it tend to absorb oil which is always present in the vicinity of rotor bearings. From that reason another type of zebra tape has been manufactured. The new type was a teflon tape of the area density of 0,3225 $kg \cdot m^{-2}$. This tape showed better mechanical robustness, however due to the larger weight it did not withstand long on the shaft. For the teflon tape of the area density of $\mu = 0{,}3225\ kg \cdot m^{-2}$, nominal rotational frequency of 50 Hz and the rotor circumference of 1,4 m the centrifugal force is $7092\ N \cdot m^{-2}$ which corresponds to the weight of approximately $723\ kg \cdot m^{-2}$. The teflon zebra tape is shown on the left side of Fig. A1.1.

For both tapes the same optical sensor has been used. It was the Brüel & Kjær 2981 laser sensor as shown on the right side of Fig. A1.1. The sensor was attached perpendicular to the rotor surface so that the laser beam pointed in the middle of the tape. Here, the axial displacement of the rotor during operation has to be considered. Two main causes of the axial displacement are the thermal dilatation of the rotor body and the unbalanced axial load of the steam on the turbine. The axial displacement amplitude is dependent on the axial distance from the thrust bearing and it varies from zero to the orders of millimeters, possibly centimeters. Hence, the sensor has to be placed so that a correct laser beam location is ensured during operation.

*Fig. A1.1 Teflon reflexive zebra tape and the optical sensor B & K 2981.*

Despite the maximum distance of 70 cm from the reflective surface declared by the manufacturer, in which the sensor can be placed, a distance of around 1 cm has proved to be the most effective. For a distance larger than 3 cm a reliable zebra tape stripe detection could not be ensured.
The output of the optical sensor is a voltage signal whose amplitude depends on the reflectivity of the surface where the output beam reflects back to the sensor detector. By the alternation of more and less reflective surface the output of the sensor gets a form of a rectangular signal. An illustration of this output signal is shown in Fig. A1.2.

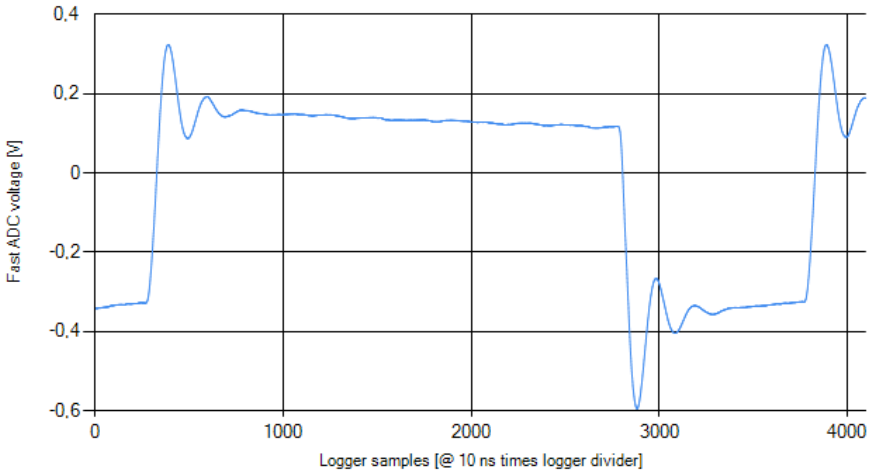


*Fig. A1.2 Voltage output signal of the sensor.*

Overall, the optical measurement can be seen as suitable for laboratory applications where there is no risk of fouling the tape or lens of the sensor, but unsuitable for the power plant environment, where there is relatively high dust and oil aerosol near the rotating parts.

### 6.1.2 Electromagnetic incremental sensors

As mentioned, optical measurement has some properties that make it unsuitable for use in a power plant environment. Especially the risk of foulishing of the tape or the sensor head by oil and dirt. Therefore, it was an attempt to construct an analogous measurement, but one that would be based on the electromagnetic principle. This effort led to the production of a custom-designed kapton tape with molded copper rectangular marks. The tape is manufactured as a 50 cm long and 3 cm wide kapton tape embedding 25 copper rectangular marks. The areal density of the tape is 0,316 kg/m$^2$.

The left hand side of Fig. 6.3 shows the kapton tape. The right hand size of the figure shows the electromagnetic sensor Emerson PR 6423 which is accompanied with an amplifier Emerson CON 041. For the placement of the sensor similar rules as that for the optical sensor are applied.

*Fig. A1.3 Kapton zebra tape and the eddy current sensor Emerson PR 6423.*

The main benefit of the electromagnetic measurement principle is its robustness against fouling. In addition, the kapton tape attached to the rotor surface with two-component epoxy is characterized by high durability and resistance to mechanical damage. All of these are invaluable features for use in industrial environments.
In Fig. A1.4 the output signal of the sensor Emerson is shown for illustration.

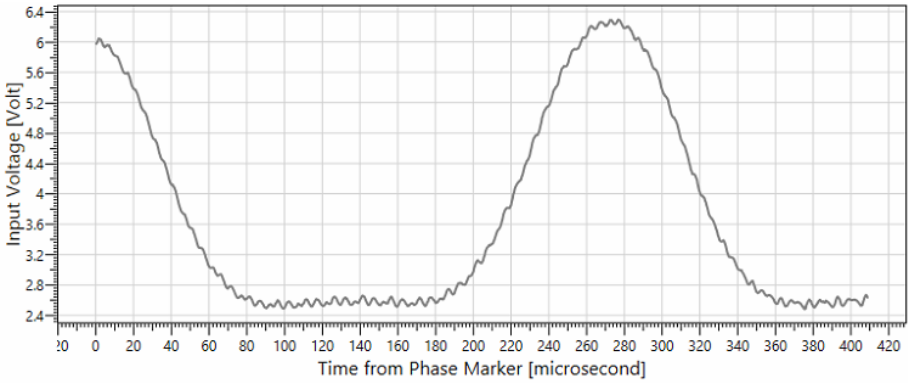


*Fig. A1.4 Voltage output signal of the sensor.*

One fact that must be mentioned is that the distance between the sensor and the rotor surface affects the offset of the output signal (note the sensor Emerson is primarily designed for distance measurement). The triggering level found for a certain sensor setup might not be usable after the sensor moved closer to or further from the rotor surface. For a proper long-term measurement campaign, it is therefore necessary to ensure that the distance between the sensor and the rotor surface remains unchanged. However this is something that can easily be ensured once the worker knows about it. Therefore we can say that the encoder using the electromagnetic principle designed in this way is more suitable for the demanding environment of the power station, especially for its robustness to fouling.

## 6.2 Appendix 2: Disturbances affecting encoder gap width

In this appendix the mechanism of action of disturbances affecting the encoder gap width will be addressed. These disturbances include those that actually change the width of the gap as well as those that do not change the width of the gap, but their final effect is equivalent.
For every mechanism the corresponding mathematical equations will be derived. The sought-after quantity is the change of the cross-sectional angle defining the distance of two adjacent stripes.
By means of the notation used throughout the work, we can define $\Delta\phi$ as

$$\Delta\phi = \Delta(\phi_{i+1} - \phi_i). \qquad (A2.1)$$

In addition, we also set specific values which are close to the practical situation. This will make it possible to compare the individual disturbances according to their significance. The considered gap width will be $\phi_{i+1} - \phi_i = 0{,}02\ m$ and the rotor circumference $1{,}4\ m$.

### 6.2.1 Non-parallelism of the edges of the encoder stripes

A non-parallelism of the edges of the encoder stripes alone will have no effect. However, in combination with a nonzero axial displacement it causes an apparent change of the gap widths. This kind of disturbance can occur in optical as well as electromagnetic measurement principle.
A good understanding of the mechanism gives Fig. A2.1. In the picture there is a short rotor section close to the measurement plane defined by the zebra tape and a sensor. For simplicity, only two encoder stripes are depicted in the zoomed view. It can be seen that the stripes, or their edges, are non-parallel. Due to this non-parallelism, if the rotor shifts axially, the apparent gap width projected in the fixed-position measurement plane changes. The gap width corresponding to the two extreme values of the axial displacement is depicted by the red double arrows.

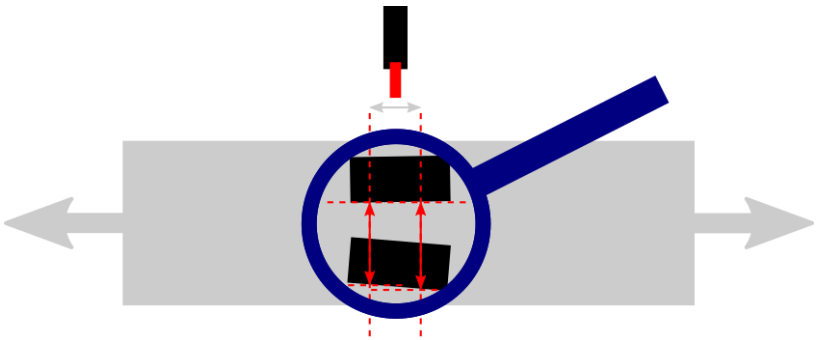

*Fig. A2.1 Non-parallelism of the encoder stripes – the mechanism.*

Next, we make a mathematical analysis of the actual effect. Let $\alpha$ represents the relative angle of the two adjacent encoder stripes as depicted on Fig. A2.2. We now want to calculate the gap width change resulting from the axial displacement $d$.

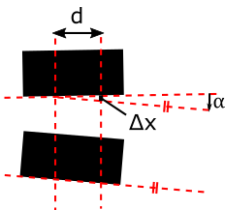


*Fig. A2.2 Non-parallelism of the encoder stripes – mathematical analysis.*

From the definition of the sine function and considering that $\alpha$ is very small we can write the following approximation

$$\Delta x = \sin\alpha \cdot d \approx \alpha \cdot d. \qquad (A2.2)$$

Let us consider the axial displacement $d = 0{,}01\ m$ and the angle $\alpha = 1 \cdot 10^{-3}\ rad$ which corresponds to a rotation of the stripe by 5 % of its width. Then the value of the gap width change is

$$\Delta x = 1 \cdot 10^{-3} \cdot 0{,}01 = 1 \cdot 10^{-5}\ \ [m]. \qquad (A2.3)$$

Finally, we convert the circumferential distance $\Delta x$ to the angular quantity $\Delta\phi$. In this calculation we use the knowledge of the rotor circumference of the size of $1{,}4\ m$. Let $\Delta\phi$ denotes the angular size of the discontinuity, then obviously

$$\Delta\phi = \Delta x \cdot \frac{2\pi}{1{,}4} = 45 \cdot 10^{-6}\ \ [rad]. \qquad (A2.4)$$

### 6.2.2 Zebra tape resolution error

The error analysed in this chapter is associated with the printing resolution of a printer with a finite dot density (dpi). The idea is that if the dot rows created by the printer are not parallel to the direction of the stripes, discontinuities in the encoder stripe edge will inevitably arise. Obviously, this kind of disturbance can occur only in the optical measurement principle. Similarly as in Chpater A2.1, not the discontinuity alone but its combination with an axial displacement is what causes the measured change of the gap width.
Figure A2.3 illustrates the situation where due to a nonzero angle between the edge direction and the direction in which the dotrows are printed a discontinuity arises. If the axial displacement causes fluctuations of the measurement plane around the point of discontinuity, gap width changes will be detected.

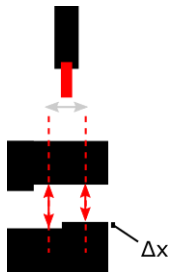


***Fig. A2.3 Discontinuity in the encoder stripe edge caused by finite printer DPI.***

Consider a printer resolution of $600\ dpi$. This means the distance between two adjacent dot rows is

$$\Delta x = \frac{1}{600} \cdot 0{,}0254 = 42 \cdot 10^{-6}\ \ [m]. \qquad (A2.5)$$

which is also the considered size of the discontinuity. The task for now is to convert this distance to angle. In this calculation we use the knowledge of the rotor circumference of the size of $1{,}4\ m$. Let $\Delta\phi$ denotes the angular size of the discontinuity, then obviously

$$\Delta\phi = \Delta x \cdot \frac{2\pi}{1{,}4} = 190 \cdot 10^{-6}\ \ [rad]. \qquad (A2.6)$$

## 6.3 Appendix 3: Detection times generator

In this last part of the chapter on incremental encoders, a relation will be derived according to which the detection times of the encoder stripes located on the rotor, the motion of which is prescribed by equation 6.7, are governed. Right the encoder stripes detection times are then used to evaluate the instantaneous angular speed. The model, which will be derived here, will be used in the next chapter to simulate the measured data for different test cases.

First, annotation used later in the equations will be introduced:

| | |
|---|---|
| $N$ | number of encoder stripes |
| $i$ | index of the $i$-th stripe, $i = 1, \dots, N$ |
| $k$ | index of the actual revolution |

Let the encoder consist of $N$ stripes whose distribution along the rotor circumference define angular positions $\varphi_i$. The angular position presents the angle between the sensor and the $i$-th stripe at the time $t = 0$. In other words it presents how much the rotor rotates so that the $i$-th stripe gets aligned with the sensor axis. If there are $N$ equidistantly distributed encoder stripes, then

$$\varphi_i = \frac{i}{N} 2\pi, \qquad (A3.1)$$

however in case of an encoder with non-equidistant stripes the values of $\varphi_i$ form any ascending sequence on the interval $\langle 0, 2\pi \rangle$

The numbering of the stripes is defined in that way a stripe with a lower index was detected *before* an other stripe with a larger index. The way stripes and the corresponding angles $\varphi_i$ are numbered is illustrated in Fig. A3.1. On the left hand side the situation at the time $t = 0$ and the angular rotation $\varphi(0) = 0$ is depicted. On the right hand side the situation at a general time $t > 0$ where the rotor is at an angular position $\varphi(t)$.

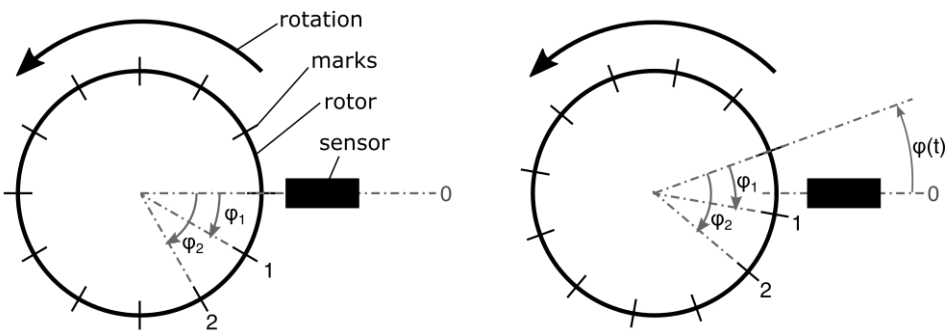


***Fig. A3.1: Introduction of the angular measures used later in the text.***

The detection of the mark by the sensor occurs just at the moment of the passage of the mark below the axis of the sensor. For an $i$-th stripe, this situation occurs every time the sum of the stripe‘s angular position and the sum of the previous revolutions equals the actual rotor angular position $\varphi(t)$. Let $t_{i,k}$ denotes the detection time of the $i$-th stripe in the $k$-th revolution. Then the previous condition can mathematically be written as

$$\varphi(t_{i,k}) = \varphi_i + 2\pi(k-1) \qquad (A3.2)$$

where $t_{i,k}$ denotes the detection time of $i$-th mark in the $k$-th revolution. By the substitution for $\varphi$ from the Eq. A3.1 and by putting all of the terms at one side we get the following implicit form

$$\omega_{rot} t_{i,k} + \sum_{i=1}^{N} \left( -\frac{A_i}{2\pi f_i} \cos(2\pi f_i t_{i,k} + \phi_i) + \frac{A_i}{2\pi f_i} \cos(\phi_i) \right) - \varphi_i - 2k\pi = 0 \qquad (A3.3)$$

Equation A3.3 is a transcendental equation with the unknown variable $t_{i,k}$ which can not be solved analytically. The equation can be solved numerically in the Matlab software $\forall i = 1, \dots, N$ and $\forall k \in \mathbb{N}$, to obtain the detection times $t_{i,k}$ of the $i$-th encoder stripe in the $k$-th revolution.

For the sake of correctness, it is necessary to mention one assumption, which is, however, formal and from a practical point of view in no way limiting, namely the monotonic growth of the quantity $\varphi(t)$. In practice, this assumption is always met because the rotor instantaneous angular speed is always

positive thanks to the relatively large rotor angular speed and relatively small contribution of the angular speed fluctuations caused by torsional vibration.

## 6.4 Appendix 4: Detection time uncertainty approximation by means of normal distribution

The subject of this appendix will be a discussion of how to move from the uncertainty in the determination of the detection time given in the form $t = t \pm \delta$ to the approximation by a normal distribution in the form $t \sim N(t, \sigma^2)$ and how to get the parameter $\sigma$.

$$t = t \pm \delta \quad \rightarrow \quad t \sim N(t, \sigma^2)$$

The procedure will be divided into two sub-tasks:

1. Find the true detection time distribution
2. Find the parameters of the approximate normal distribution

It is not trivial to determine the true detection time distribution . In fact this leads to solving the equation

$$\alpha t + cos(t + t_0) = const., \qquad (A4.1)$$

on the left side is the sum of the useful signal (modelled only by a linearly rising leading edge) and the harmonic noise. On the right is a constant representing the threshold level. The symbol $t$ denotes the variable time, $t_0$ ,represents the initial phase and thus the mutual shift of harmonic noise and useful signal.

Equation A4.1 is a transcendental equation for the variable $t$ for which there is no analytical solution. So we will solve the problem numerically in the Matlab program. First, we plot the dependence of the error in determining the leading edge detection time on the relative shift of the harmonic noise and the useful signal. Since the noise is harmonic, it is sufficient to investigate the relative shift interval $\langle 0, 2\pi \rangle$.

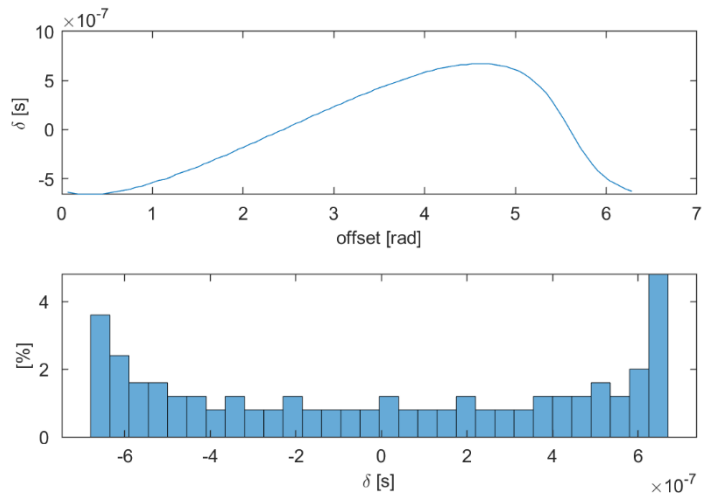


***Fig. A4.1: Introduction of the angular measures used later in the text.***

Although the resulting function shown in the upper plot of Fig. A4.1 does not have a symmetrical shape, the histogram of its values shown in the lower plot shows that the function values are approximately uniformly distributed on the given interval $\langle -\delta, \delta \rangle$, except at the edges of the interval, where an increased number of values is recorded. However for the purpose of distribution approximation it is possible to consider the distribution as uniform.

Thus, we have shown above that the additive harmonic noise leads to an approximately uniformly distributed leading edge detection time error on the interval $\langle -\delta, \delta \rangle$.

In the next we will look for the parameters of the approximate normal distribution, ie the mean and standard deviation. The mean value will probably be half the interval $\langle -\delta, \delta \rangle$, thus 0.The standard deviation $\sigma$ will be obtained using the standard relationship

$$\sigma^2 = \frac{(b-a)^2}{12}, \qquad (A4.2)$$

where $a$ and $b$ are the limits of the interval of the uniform distribution. After the substitution of the true limits $\pm\delta$ and after the square root operation we get

$$\sigma = \sqrt{\frac{\left(\delta - (-\delta)\right)^2}{12}} = \frac{1}{\sqrt{3}}\,\delta, \qquad (A4.3)$$

The resulting distribution of detection times is thus $t \sim N\left(0, \frac{\delta^2}{3}\right)$.

# 7 Bibliography


[1] Bing, L., Xining, Z.: *A new strategy of instantaneous angular speed extraction and its application to multistage gearbox fault diagnosis*, Journal of Sound and Vibration, 396, pp 340-355, 2017.

[2] Braut, S., Zigulic, R., Stimac, G., Skoblar, A.: *Efficient approach for encoder geometry compensation in time interval measurement of torsional vibration*, 10th International Conference on Vibrations in Rotating Machinery, pp 809–818, 2012.

[3] Buskirk, E.: *Torsional Dynamics – Large 2-pole and 4-pole Steam Turbine Powertrains*, GER-4724, 05/2013.

[4] Chen, M., Zheng, N., Zheng, J., Lu, D., Luo, G., Diamond, W.: *Phase demodulation of torsional vibration measurement by zebra-tape method undertime-varying speed*, Mechanical Systems and Signal Processing, 2021.

[5] Diamond, D., H., Heyns, P., S., Oberholster, A., J.: *Online shaft geometry compensation for arbitrary shaft speed profiles using Bayesian regression*, Mechanical systems and Signal Processing, 81, pp 402-418, 2016.

[6] Feynman, R., P.: *Feynmanovy přednášky z Fyziky*, ISBN 0-201-02116-1-P, 2000.

[7] Gee, S., W., Conder, L.: *A Strain Gauge Manual*, Structures Technical Memorandum, 378, 1984.

[8] Giesecke, H., D.: *Steam Turbine-Generator Torsional Response due to Interaction with the Electrical Grid*, 2012 IEEE Power and Energy Society General Meeting, ISBN 978-1-4673-2729-9, 2012.

[9] Hensel, S., Strauß, T., Marinov, M.: *Eddy current sensor based velocity and distance estimation in rail vehicles*, IET Science, Measurement and Technology, Vol. 9, pp 875-881, 2015.

[10] Hirsch, M.: *A Real-Time Eye on Turbines*, EPRI Journal, 6, pp 6-9, 2016.

[11] Holm, J.: *Comparison of methods to measure torsional vibration*, Bakalářská práce, Novia University of Applied Sciences, 2014.

[12] Huster, J., Eckert, L., Pohle, F.: *Calculation and measurement of torsionals in large steam turbines*, ABB Review, pp 31-40, 6/1998.

[13] Janssens, K., Van Vlierberghe, P., Claes, W., Peeters, B., Martens, T., D'Hondt, P.: *Zebra Tape Butt Joint Detection and Correction Algorithm for Rotating Shafts with Torsional Vibrations*, Proceedings of ISMA, pp 2869-2882, 2010.

[14] Kilgore, L., A., Ramey, D., G., Hall, M., C.: *Simplified transmission and generation system analysis procedures for subsynchronous resonance problems*, IEEE Transactions on Power Apparatus and Systems, Vol. PAS-96, no. 6, pp 1840-1846, 1977.

[15] Machowski, J., Bialek, J., W., Bumby, J., R.:*Power system dynamics: stability and control*, ISBN 978-0-470-72558-0, 2008.

[16] Lakshmanan, M.: *The fascinating world of the Landau-Lifshitz-Gilbert equation: an overview*, Philosophical Transactions of the Royal Society, Vol 369, pp 1280-1300, 2011.

[17] Leader, M. E., Kelm, R. D.: *Practical Implementation of Torsional Analysis and Field Measurement*, National Technical Training Symposium and Annual Meeting, pp 131-168, 2004.

[18] Lennerhag, O., Bollen, M. H. J., *Power system impacts of decreasing resonance frequencies*, 2018 18th International Conference on Harmonics and Quality of Power, pp 1-6, 2018.

[19] Lopera, J., M., Prieto, M., J., Linera, F., F., Vecino G., González, J., A.: *A new speed measurement system*, IEEE Industry Applications Magazine, pp 44-51, Nov/Dec, 2005.

[20] Miles, T., J.: *New developments in experimental analysis of torsional vibration for rotating shaft systems*, Doktorská práce, Loughborough University, 1997.

[21] Míšek, T.: *Dynamická analýza olopatkovaných disků axiálních turbosoustrojí*, Disertační práce, Katedra mechaniky FAV UWB, 2011.

[22] Nordmann, R.: *Torsional and stator vibrations in turbines and generators*, Energiforsk, 2016, ISBN 978-91-7673-295-3.

[23] Okabe, A., Otawara, Y., Kaneko, R., Matsushita, O., Namura, K.: *An equivalent reduced shaft modelling method and its application to shaft-blade coupled torsional vibration analysis of a turbine-generator set*, Proceedings of the Institution of Mechanical Engineers, Vol 205, pp 173-181, 1991.

[24] Petit, F., De Bauw, K., Matthys, K., Doucement, S.: *Investigating grid-induced turbo-generator vibrations: a multidisciplinary challenge*, Proceedings of the 9th IFToMM International Conference on Rotor Dynamics, 2011.

[25] Resor, B., R., Trethewey, M., W., Maynard, K., P.: *Compensation for encoder geometry and shaft speed variation in time interval torsional vibration measurement*, Journal of Sound and Vibration, 286, pp 897-920, 2005.

[26] Schaber, U., Mayer, J., F., Stetter, H.: Coupled blade bending and torsional shaft vibration in turbomachinery, International Gas Turbine and Aeroengine Congress and Exposition, 1993.

[27] Siemens PLM Software: *Identifying best practices for measuring and analysing torsional vibration*, Siemens white paper 36423-Y5, 8, 2014.

[28] Tüysüz, A., Flankl, M., Kolar, J., W., Mütze, A.: *IEEE 2nd Annual Southern Power Electronics Conference*, pp 1-6, 2016.

[29] Václavík, J., Chvojan, J. *Torsional vibration monitoring of turbine shafts*. Procedia Structural Integrity, Vol. 5, pp 1349-1354, 2017.

[30] Vejražka, F.: *Signály a soustavy*, Vydavatelství ČVUT, 1992.

[31] Walker, D., N.: *Steam Turbine-Generator Torsional Vibration Interaction with the Electrical Network: Tutorial*, EPRI, 2005.

[32] Walker, D., N.: *Torsional Vibration of Turbo-Machinery*, ISBN 978-0071430371, 2013.

[33] Wang, P., Gao, Y., Tian, G., Wang, H.: *Velocity effect analysis of dynamic magnetization in high speed magnetic flux leakage inspection*, Nondestructive Testing and Evaluation, Vol. 64, pp 7-12, 2014.

[34] Watanabe, M., Iki, H., Sakamoto, K., Mitani, Y., Uriu Y., Kado, Y.: *Analysis of Turbine Generator Shaft Torsional Vibration Caused by Self-Commutated Converters*, Electrical Engineering in Japan, Vol. 193, No. 4, pp 900-907, 2015.

[35] Zeman, V., Hlaváč, Z.: *Kmitání mechanických soustav*, Západočeská univerzita v Plzni, 2004.

[36] Zhao, M., Jia, X., Lin, J., Lei, Y., Lee, J.: *Instantaneous speed jitter detection via encoder signal and its application for the diagnosis of planetary gearbox*, Mechanical Systems and Signal Processing, 98, pp 16-31, 2018.

[37] *Identifying best practices for measuring and analysing torsional vibration*, Siemens PLM Software, 36423-Y5, 8/2014.

# 8 Publications


Liška, J., Jakl, J., Künkel, S.: *Measurement and evaluation of shaft torsional vibrations using shaft instantaneous angular speed*, Journal of Engineering for Gas Turbines and Power, pp 041029 1-5, Vol. 141, 4/2018.

Liška, J., Jakl, J., Strnad. J., Künkel, S.: *Measurement and evaluation of shaft torsional vibrations to reveal the rotating blades excitation sources*, First World Congress on Condition Monitoring, London 12.6.-16.6.2017. ISBN 978-0-903132-64-0.

Künkel, S.: *Měření torzních vibrací rotoru turbogenerátoru***,** Student scientific conference 2017, Pilsen 25.5.2017. ISBN 978-80-261-0706-4.

Liška, J., Künkel, S.: *Localization of loose part impacts on the general 3D surface of the nuclear power plant coolant circuit components*. Progress in Nuclear Energy, Volume 99. August 2017.

Liška, J., Jakl, J., Künkel, S.: *A novel method for on-line 3D localization of loose parts in nuclear power plant cooling system*. The Thriteenth International Conference on Condition Monitoring and Machinery Failure Prevention Technologies, Paris 10.-12.10.2016. ISBN 978-0-903132-63-3.

Liška, J., Jakl, J., Künkel, S.: *Error Considerations for Turbine-Generator Torsional Vibration Monitoring*, Turbo Expo Turbomachinery Technical Conference & Exposition Proceedings, 2020, GT2020-15454.

Liška, J., Jakl, J., Künkel, S.: *Torsional vibration encoder-based monitoring methods and their experimental validation*, The Sixteenth International Conference on Condition Monitoring and Asset Management - CM 2019, Glasgow, UK. 2019

Liška, J., Jakl, J., Künkel, S.: *Torzní vibrace rotorů turbogenerátorů – měření a diagnostika*, Řízení & údržba průmyslového podniku, 59, 4.

Künkel, S.: *Dlouhodobý monitoring torzních vibrací velkých turbogenerátorů*, Student scientific conference, 30.5.2019, UWB, Pilsen.

Liška, J., Jakl, J., Künkel, S.: *Error Considerations for Turbine-Generator Torsional Vibration Monitoring*, Turbo Expo Turbomachinery Technical Conference & Exposition Proceedings, 2020, GT2020-15454

Liška, J., Jakl, J., Künkel, S.: *Torsional vibration encoder-based monitoring methods and their experimental validation*, Condition Monitor, 408, 7-9, 2021.

Liška, J., Jakl, J., Vašíček, V., Kalista, K., Káš, M., Künkel, S.: *Vibration monitoring of rotating machine components*, Condition Monitor, 395, 6-9, 2020.

Liška, J., Jakl, J., Künkel, S.: *Advanced turbine-generator torsional vibration evaluation method using Kalman filtering*, Insight - Non-Destructive Testing and Condition Monitoring, August 2022.

Liška, J., Jakl, J., Künkel, S., Šťastný, L., Mego R.: *Partial discharge detection in modern power grid*, Condition Monitor, Diagnostika 2022, Pilsen.

Liška, J., Jakl, J., Künkel, S.: *Advanced turbine-generator torsional vibration evaluation method using Kalman filtering*, CM 2022 and MFPT 2022, London.

Künkel, S.: *Určení geometrie enkodéru v úloze monitoringu torzních vibrací*, Student scientific conference 2022, FAV, Pilsen.

Liška, J., Jakl, J., Künkel, S.: *Measurement and evaluation of shaft torsional vibrations using shaft instantaneous angular velocity*, ASME Turbo Expo 2018: Turbomachinery Technical Conference and Exposition, 11.6.-15.6.2018, Lillestrom, Oslo. DOI: 10.1115/GT2018-76406.

Künkel, S.: *Diagnostika torzních vibrací rotoru turbogenerátoru*, Student scientific conference, 31.5.2018, UWB, Pilsen.